This is to certify that the
dissertation entitled
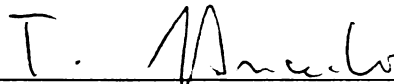
Angular distributions of gamma rays with intermediate-energy
beams and spectroscopy of ^{32}Mg

presented by

Heather Zwahlen

has been accepted towards fulfillment
of the requirements for the

_____Ph.D._____ degree in _____Dept of Physics and Astronomy_____

Major Professor's Signature

12/5/2005

Date

PLACE IN RETURN BOX to remove this checkout from your record.
TO AVOID FINES return on or before date due.
MAY BE RECALLED with earlier due date if requested.

DATE DUE	DATE DUE	DATE DUE

Angular distributions of gamma rays with intermediate-energy beams
and spectroscopy of ^{32}Mg
By

Heather Zwahlen

A DISSERTATION

Submitted to
Michigan State University
in partial fulfillment of the requirements
for the degree of

DOCTOR OF PHILOSOPHY

Department of Physics and Astronomy

2005

ABSTRACT

ANGULAR DISTRIBUTIONS OF GAMMA RAYS WITH INTERMEDIATE-ENERGY BEAMS AND SPECTROSCOPY OF ^{32}Mg

By

Heather Zwahlen

The feasibility of using γ-ray angular distributions and γ-γ angular correlations with intermediate-energy beams to assign multipolarities of γ-ray transitions is explored theoretically and experimentally. The formalism for γ-ray angular distributions and γ-γ angular correlations with intermediate-energy beams is presented. At the National Superconducting Cyclotron Laboratory (NSCL) the γ-ray angular distribution of the first excited state in ^{40}Ar was measured in an intermediate-energy Coulomb excitation experiment. The observed γ-ray angular distribution agrees with the calculated distribution.

The nucleus ^{32}Mg was studied in a two-proton knockout experiment performed at the NSCL. Nine γ rays were observed; five for the first time. Here, excited state energies and partial cross sections to those states are presented. A level scheme is constructed based upon γ-γ coincidence data and γ-ray intensities. The results confirm that the ground state wavefunction of ^{34}Si is dominated by the sd shell configuration. Previous experiments observed a γ ray around 1438 keV. The interpretations of those experiments resulted in possible contradictions in spin and parity assignments for an excited state in ^{32}Mg. In the present experiment two peaks were identified around 1438 keV. The existence of two distinct levels may resolve these contradictions. Calculations of the two-proton knockout reaction, assuming two correlated protons knocked out of the $d_{5/2}$ shell, predict three pure sd states that are not observed in the present experiment. These sd states are each thought to fragment over a few MeV to create six of the observed excited states.

my father

ACKNOWLEDGMENTS

the phones and plane tickets helped make it possible. Jacque, without you I couldn't have done this. Thank you for everything, for your love, for all of you.

Contents

List of Figures

IMAGES IN THIS DISSERTATION ARE PRESENTED IN COLOR.

List of Tables

Chapter 1

Introduction

1.1 The atomic nucleus

The atomic nucleus is a many-body system composed of nucleons bound together by the strong force. Protons (Z) and neutrons (N) are spin 1/2 fermions and are two different states of the nucleon in isospin representation. The mass number, A, is the sum of the number of protons and neutrons in a nucleus. Protons have charge e and neutrons have zero charge. The size of the nucleus increases as the number of protons and neutrons increase. The radius in femtometers (fm) can be approximated by $1.2 \times A^{1/3}$.

The study of nuclear physics aims to understand the force between nucleons, study the structure of atomic nuclei, and understand the interactions between nucleons and other subatomic particles. Studying the properties of atomic nuclei is the focus of nuclear structure research. These properties include energies, spins and parities of excited states, nuclear shapes, and electromagnetic moments and transition rates. Trends in some of these properties become apparent when examined over the entire nuclear chart. Nuclei with a 'magic' number - 2, 8, 20, 28, 50, 82 or 126 - of protons and/or neutrons exhibit distinct properties from those of neighboring nuclei. This will be discussed in the next section.

Interactions between nucleons are primarily governed by the strong force but also are influenced by the weak and electromagnetic interactions. The strong force is poorly understood and different theoretical models are used to approximate the behavior of atomic nuclei. These models aim to reproduce the properties of known nuclei that have been measured experimentally and accurately predict the properties of nuclei that have not yet been studied. Experimental nuclear structure information is used to test and improve these theoretical models. The current nuclear structure models can be divided into two major categories: collective and single-particle.

Collective models focus on how the nucleons act together using collective degrees of freedom. One such model is the vibrational model which describes nuclear excitations as vibrations of the nucleons as a whole. Another collective model is the rotational model which describes nuclear excitations as rotations of statically-deformed nuclei.

Single-particle models focus on the individual nucleons using the individual nucleon's degrees of freedom. The most well-known single-particle model is the nuclear shell model.

1.2 The nuclear shell model

The nuclear shell model is a single-particle model where each nucleon is assumed to move in a potential created from the other $A - 1$ nucleons. If the potential is estimated using a three-dimensional harmonic oscillator, the resulting single-particle energy spectrum has large energy gaps between groupings of energy levels (shells). The first few shell gaps appear at nucleon numbers 2, 8, 20, 40 and 70. Experimentally the magic numbers, or the number of nucleons needed to fill up the last shell before a large energy gap, occur at 2, 8, 20, 28, 50, 82 and 126. The nucleons have an intrinsic spin, s, and orbital angular momentum, l. Coupling l and s, to a total spin j, and adding it to the three-dimensional harmonic oscillator potential results in a potential that accurately reproduces the experimentally observed magic numbers:

2, 8, 20, 28, 50, 82 and 126. This 'spin-orbit' term was first suggested in 1949 [1, 2]. Fig. 1.1 shows a schematic diagram of energy levels calculated in the spherical shell model. In general, nuclei are spherical at closed shells (where the number of protons and/or neutrons are equal to a magic number). This can be understood because if a shell is filled with $2j + 1$ protons or neutrons, then the total projection of the spin along the quantization axis is zero. At closed shells nuclei typically also have large first excited state energies, large proton and neutron separation energies and small reduced transition probabilities, B(E2↑), to the first excited state. Examples of nuclei with large first excited state energies in the N=20 region are, 3.328 MeV for ^{34}Si, 3.291 MeV for ^{36}S and 2.167 MeV for ^{38}Ar. For a given Z, as N increases the two-neutron separation energy (S_{2n}) decreases smoothly until a shell closure is reached. At the crossing of a shell closures there is a sharp drop in S_{2n} because the new neutron shell has less binding energy. Mid-shell nuclei (where the numbers of protons and neutrons are in between the magic numbers) tend to have smaller first excited state energies and larger B(E2↑) values. Larger B(E2↑) values are indicative of a collective behavior - rotational or vibrational excitations. In between closed shells there are many single-particle states available and therefore it is often more energetically favorable for a nucleus to assume a deformed shape.

The spherical shell model potential can be modified to reproduce experimental observables for deformed nuclei. The deformed shell model, or Nilsson model [3], uses the potential of the spherical shell model plus a deformation term. The deformation term typically is due to a quadrupole field. Since in the Nilsson model nuclei are no longer assumed to be spherical, j is no longer a good quantum number, but the projection of j along the quantization axis is a good quantum number. Therefore each single-particle level splits into $(2j+1)/2$ states. The resulting calculated single-particle energies as a function of the deformation of the nucleus, for non-zero deformation parameters, can change significantly. For example, the energy of the $f_{7/2}$ level can drop below the $d_{3/2}$ level essentially eliminating the N=20 shell gap. This occurs in
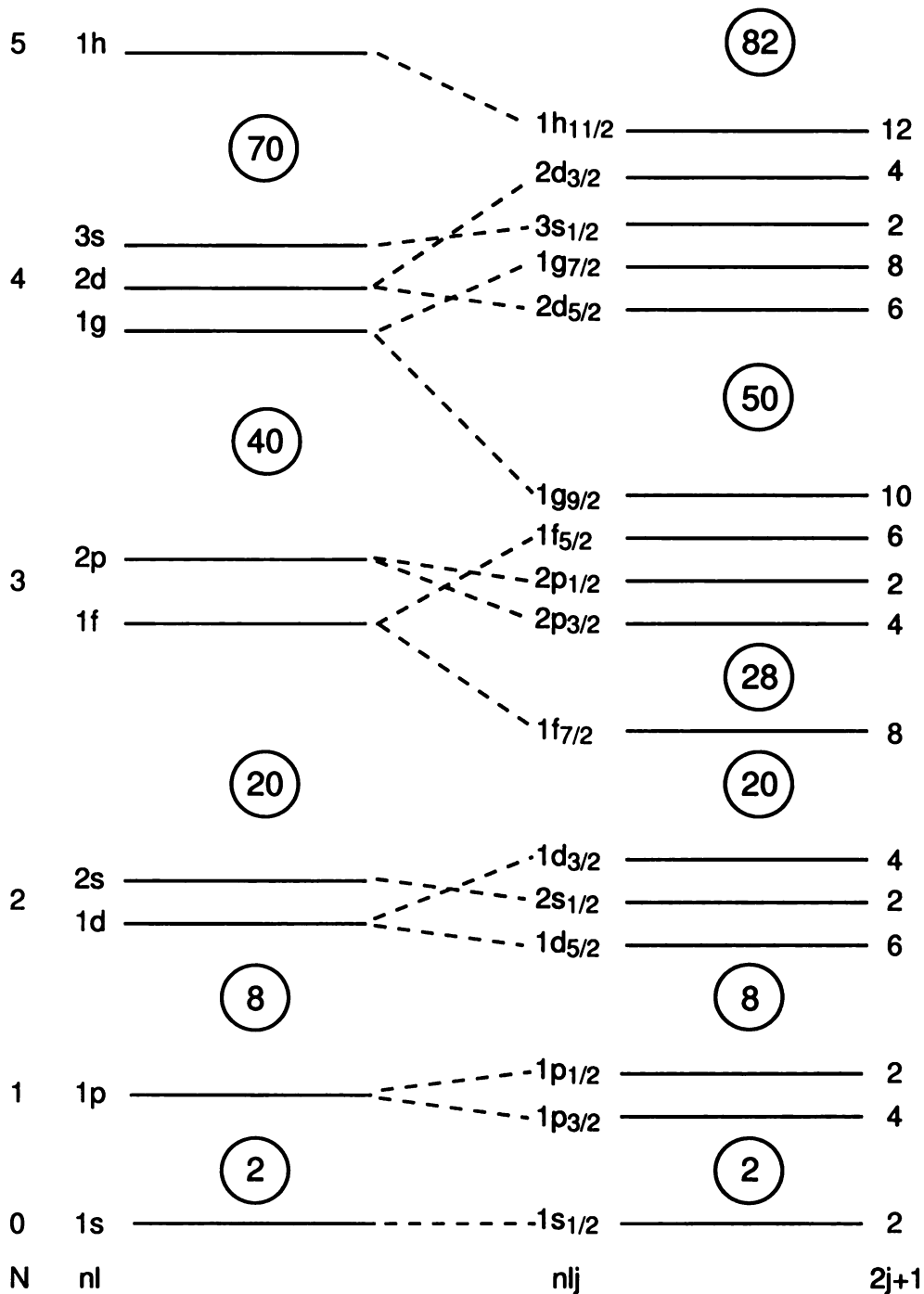
Figure 1.1: Schematic diagram of energy levels calculated in the spherical shell model, shown up to the $1h_{11/2}$ level. On the left is the single-particle spectrum produced by an isotropic, three-dimensional harmonic oscillator potential. On the right is the single-particle spectrum with the spin-orbit interaction included. N is the number of harmonic oscillator quanta in a major shell. The radial quantum number, n, increases each time a particular lj combination occurs in order of ascending energy. The angular momentum quantum number, l, equals 0, 1, 2, 3, 4, 5, 6... corresponding to s, p, d, f, g, h, i, ... The projection of the total spin, j, is equal to $l + s$. The numbers in the right-hand column are the maximum number of nucleons each level can contain. The magic numbers are indicated in each major shell gap.

4

^{32}Mg as discussed in Section 1.4. The Nilsson model in the context of the vanishing N=20 shell gap is further discussed in [4].

In discussions of protons and neutrons occupying levels in the shell model, π and ν will be used in the text to indicate protons and neutrons, respectively. The p shell refers to the $1p_{3/2}$ and $1p_{1/2}$ group of single-particle levels. The sd and fp shells refer to the $1d_{5/2}$, $2s_{1/2}$, and $1d_{3/2}$ and the $1f_{7/2}$, $2p_{3/2}$, $2p_{1/2}$, and $1f_{5/2}$ groups of single-particle levels, respectively. As used here, $0\hbar\omega$ configurations refer to nucleons occupying the sd shell with no nucleons in the fp shell. $N\hbar\omega$ configurations refer to N nucleons in the fp shell.

1.3 γ-ray angular distributions and γ-γ angular correlations

Below the nucleon separation energies, nuclei in excited states can decay by γ-decay, β-decay, α-particle emission, conversion electron emission, and fission. Electromagnetic decay, or the emission of γ rays, is the dominant mode of decay for low-lying excited states in nuclei. Measuring the energies and intensities of γ rays emitted as nuclei deexcite from excited states to their ground states can give information on the excited state structure and shape of nuclei. The excited states have spin I and parity π, denoted by I^π. The deexcitation γ ray from an initial state i to a final state f can have multipolarities l with, $|I_i - I_f| \leq l \leq |I_i + I_f|$ (where $l \geq 1$ because a photon has spin 1), based on angular momentum coupling. The parities of the initial and final states are constrained by the parity selection rule, $\pi_i\pi_f = (-1)^l$ for electric (El) transitions and $\pi_i\pi_f = (-1)^{l+1}$ for magnetic (Ml) transitions. Determining the multipolarity of γ-ray transitions can constrain the possible I_i^π and I_f^π values. If the ground state is known to be a 0^+ state and a γ-ray decay to the ground state is observed, measuring the multipolarity of the γ ray would give the spin of the initial state, I_i.

Measuring γ-ray angular distributions and γ-γ angular correlations from excited nuclei are important tools in nuclear structure studies because of the ability to assign multipolarities and multipole mixing ratios of γ-ray transitions. In-beam techniques are well established for beams with energies near the Coulomb barrier (see for example [5]), but have not been thoroughly investigated for intermediate-energy ($v/c \approx 0.3 - 0.8$) exotic beams. An advantage of measuring γ-γ angular correlations from excited nuclei over measuring γ-ray angular distributions is that there can be an anisotropy in the angular correlation distribution even if there is no initial orientation of the nuclei.

For various excitation methods, the m substate distributions can be calculated or estimated. From the m substate distribution the γ-ray angular distributions and γ-γ angular correlations can be calculated. Fusion evaporation, fragmentation, intermediate-energy Coulomb excitation and nucleon knockout will be discussed in Chapter 2.

The feasibility of using γ-ray angular distributions with fast exotic beams is shown in Chapter 4 for the intermediate-energy Coulomb excitation of ^{40}Ar. Shown in Chapter 5 are γ-ray angular distributions measured in the two-proton knockout reaction ^{9}Be(^{34}Si,^{32}Mg γ)X. A discussion regarding the feasibility of using γ-ray angular distributions to determine multipolarities of γ rays in future nucleon-knockout and fragmentation reactions is in Section 5.4.3.

1.4   The nucleus ^{32}Mg

The first observation of ^{32}Mg was in 1977 [6]. A low first 2^+ excitation energy of 885 keV was determined for ^{32}Mg in the β decay of ^{32}Na in 1979 [7] (see also Table 1.1 and references therein). Mass measurements of ^{32}Mg [8, 9] revealed a larger mass (and S_{2n}) than predicted with N=20 assumed to be a good shell closure. A large B(E2↑) value [4, 10] was measured for ^{32}Mg. A simple sd shell model picture [11] of the nucleus ^{32}Mg could not explain the small first 2^+ energy, large B(E2↑) and

relatively large S_{2n} value. These anomalies have been studied in shell model [11–22] and mean-field [23–31] calculations. In ^{32}Mg, the binding energy of $2\hbar\omega$ configurations, where two neutrons are excited across the N=20 shell gap to the fp shell, is lower than 'normal' $0\hbar\omega$ configurations, where there are no neutrons excited across the N=20 shell gap. This 'inversion' - where the $2\hbar\omega$ configurations are lower in energy than the $0\hbar\omega$ configurations - is thought to be due to the reduction of the N=20 shell gap between the $\nu d_{3/2}$ and $\nu f_{7/2}$ orbitals due to a large excess of neutrons and proton-neutron interactions between the $\pi d_{5/2}$, $\nu d_{3/2}$ and $\nu f_{7/2}$ orbitals [12, 15, 22]. Assuming an axially symmetric shape, the intrinsic quadrupole moment and quadrupole deformation parameter can be calculated from the B(E2↑) value. In shell model calculations [15, 19, 20] the deformation is in this way predicted to be prolate. The Nilsson model calculations in [4], in agreement with the experiment [4], predict prolate deformation for ^{32}Mg.

This inversion effect is most pronounced for nuclei with Z=10-12 and N=19-22. This so-called Island of Inversion [15] was first discovered with the measurement of the masses of ^{31}Na and ^{32}Na [32]. The experimental masses (and S_{2n} values) were greater than expected if N=20 was a good shell closure. This measurement prompted the study of the entire region, including the nucleus ^{32}Mg. The east (most neutron-rich) boundary of the Island of Inversion is not clear [20]. The $2\hbar\omega$, $1\hbar\omega$ and $0\hbar\omega$ configurations are all in close competition for low excitation energies [19, 33]. The ground states of ^{30}Ne, ^{31,32}Na and ^{32}Mg are all dominated by $2\hbar\omega$ configurations [12, 14, 15, 17–20, 22]. At N=19 and N=22, the energy differences between normal and intruder configurations are nearly degenerate [19]. Two recent experiments showed ^{33}Mg to be in the Island of Inversion [34] and ^{30}Mg to be outside the Island of Inversion [35].

According to the Nilsson model, the nucleus must be deformed in order for the $f_{7/2}$ orbital to be in close competition at low excitation energies with the $d_{3/2}$ orbital. However, deformation is not a necessary condition to reproduce the properties seen in ^{32}Mg

Table 1.1: Previously observed ^{32}Mg γ rays. If there are no uncertainties listed, they were not quoted in the respective papers.

Ref.	Year	Reaction	Energy (keV) of observed γ rays assigned to ^{32}Mg decay
[10]	1995	^{208}Pb(^{32}Mg,^{32}Mg γ)	890
[4]	1999	^{197}Au(^{32}Mg,^{32}Mg γ)	885(9), 1438(12)
[37]	2001	^{9}Be(^{36}Si,^{32}Mg γ)X	885, 1430
[38–43]	2000-2002	^{9}Be(^{36}S,^{32}Mg γ)X	885(10), 1430(10), 1950(20), 2870(40)
[44]	2003	^{9}Be(^{34}Si,^{32}Mg γ)X	880(20), 1430(20)
[45]	2002	^{28}Si(^{32}Mg,^{32}Mg γ)X	860(50), 1460(50)
[7]	1979	β decay of ^{32}Na	885.7(2.0), 1233(4), 1440(4), 1970(5)
[46]	1984	β decay of ^{32}Na	885.5(0.7), 1782.4(0.9), 1973.0(1.2), 2151.5(0.7), 3934.8(1.8)^a
[47]	1993	β decay of ^{32}Na	885, 1232, 1436, 1783, 1973, 2152, 2551, 3935
[34]	2001	β-n decay of ^{33}Na	885.3(1), 1437.0(3), 1972.9(5), 2152.4(1), 2551(1)

^{a}Also observed were γ rays at the following energies: 239.5(1.2), 694.4(1.2), 1436.1(1.0), 1232.2(1.2), 2550.7(1.0). The last three have been seen and assigned to ^{32}Mg in later beta decay experiments [7,34,47] listed in the table.

according to a recent calculation. In [31], Hartree-Fock-Bogoliubov(HFB) [36] plus quasiparticle random phase approximation calculations reproduce the large B(E2↑) value and small first 2^+ energy in ^{32}Mg assuming no deformation effects but only neutron-pairing correlations between the $\nu f_{7/2}$, $\nu p_{3/2}$ and $\nu p_{1/2}$ levels. The $2\hbar\omega$ configuration can be generated by deformation effects or neutron-pairing effects. In [31] neutron-pairing effects are shown to be essential. An older HFB calculation [26] and relativistic mean-field calculation [28] both predict ^{32}Mg to be spherical as well.

1.4.1 Previously observed ^{32}Mg γ rays

In ^{32}Mg, the $2^+ \rightarrow 0^+_{g.s.}$ γ-ray transition at 885 keV was first observed in the β decay of ^{32}Na in 1979 [7]. Since then eight other γ rays have been observed in ^{32}Mg as summarized in Table 1.1. The level schemes as observed in β decay [47] and in fragmentation [40] reactions are shown in Fig. 1.2. One γ ray of interest is the γ ray at approximately 1430 keV.
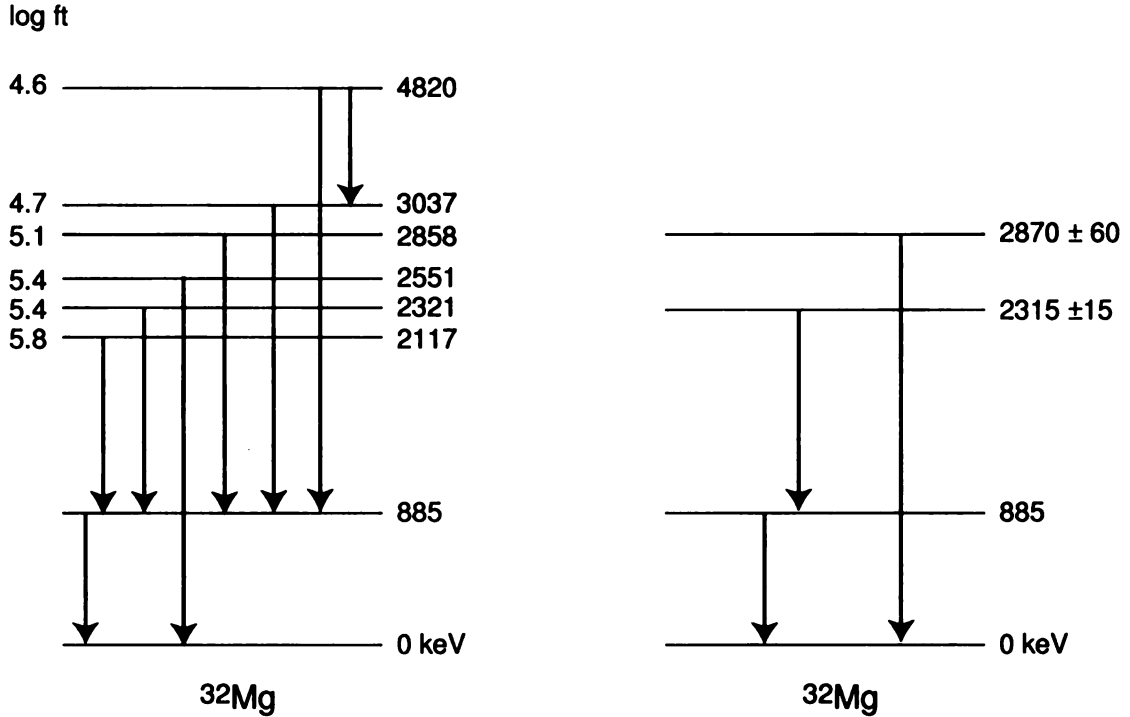
Figure 1.2: Level schemes from β decay [47] (left panel) and the fragmentation reaction $^9Be(^{36}S,^{32}Mg\ \gamma)X$ as reported in [40] (right panel).

The 885 keV γ ray has been observed in coincidence with a γ ray at approximately 1430 keV in Refs. [37,47] and [38] (also reported in [39–43]). The 1430 keV γ ray has been observed in intermediate-energy Coulomb excitation [4,10], fragmentation [37,38], nucleon-knockout [44], beta-decay [7,34,47] and inelastic-scattering [45] measurements. The assignment of the 1430 keV γ ray to a $4^+ \rightarrow 2^+$ transition [38] (also stated in [39–43]), in agreement with [20] and a calculation by F. Nowaki in [39–41,43], is not consistent with the intermediate-energy Coulomb excitation experiments in which the 1430 keV γ ray was seen. In the intermediate energy Coulomb excitation experiment in [10] (and also reported in [48]), a γ ray around 1430 keV is clearly visible in the published γ-ray spectrum, but is not discussed in the text. In intermediate-energy Coulomb excitation a direct E4 excitation from the $0^+_{g.s.}$ to a 4^+ state is unlikely and in [4] the observed γ ray yields were inconsistent with multi-step excitations which are suppressed at intermediate beam energies. In β decay, the 1436 keV γ ray deexcites a level at 2321 keV. The 2321 keV level has a measured

9

log ft value of 5.4 [47]. (The ft-value is proportional to the β-decay half-life.) The log ft value of 5.4 means the transition is allowed. The selection rules for an allowed β decay are that $\Delta J = 0$ or 1, $\Delta T = 0$ or 1 and that there is no parity change. ΔT is the change in isospin from the initial to the final state. Therefore, assuming ^{32}Na has a negative parity ground state, the 2321 keV level must have negative parity. This contradicts the tentative assignment of 4^+ and also contradicts two of the tentative spin assignments from the intermediate-energy Coulomb excitation experiment [4].

One goal of this work is to determine the multipolarity of the 1430 keV γ ray using γ-ray angular distributions. As will be seen in Chapter 5, the 1430 keV γ ray is more complicated than originally expected. However, this may resolve the spin and parity contradictions of the exited state around 2321 keV. A comprehensive description of ^{32}Mg, as the prototypical nucleus in the Island of Inversion, will be presented.

Chapter 2

γ-ray angular distributions and γ-γ angular correlations

2.1 Angular correlation formalism

2.1.1 Notation and terminology

In this work[1], the notation of [51] is used. Fig. 2.1 shows the initial I_i, middle I_m and final I_f spins of a two step γ-ray cascade. The lowest multipolarities of the γ-ray transitions are l and l' for the spin $I_i \rightarrow I_m$ transition and l_{mf} and l'_{mf} for the spin $I_m \rightarrow I_f$ transition. I_{ii} is the spin of the initial state before the nucleus is excited and l_e is the orbital angular momentum of the excitation. The general formalism for spin cascades with more than two γ-ray transitions is addressed elsewhere [5, 52, 53] for low energy beams. Some of the following equations can be found in the literature (see for example [5, 51–54]), but for completeness they are presented here as well.

In this work the use of the terminology γ-γ angular correlations is used when referring to cases when there is no alignment in the initial excited state as well as

---
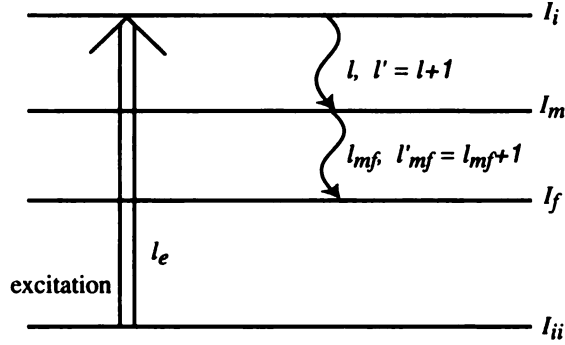
Figure 2.1: Notation used in angular correlation formalism. I_i, I_m and I_f are the initial, middle and final spins of the γ-ray cascade respectively. The lowest possible multipolarities of the γ-ray transition are l and $l' = l + 1$ for the spin $I_i \rightarrow I_m$ transition and l_{mf} and $l'_{mf} = l_{mf} + 1$ for the spin $I_m \rightarrow I_f$ transition. I_{ii} is the spin of the initial state before the nucleus is excited and l_e is the orbital angular momentum of the excitation.

when there is some alignment in the initial excited state. The latter is also referred to as directional correlations from oriented nuclei (DCO). In this work the acronym DCO is not used because the term DCO can be associated with DCO ratios in which ratios of different correlation curves are taken as the physical observable instead of the correlation itself as is examined here.

For the illustrative purposes of this chapter, only pure transitions of the lowest allowed multipolarity are considered. The notation $I_i \rightarrow I_m \rightarrow I_f$ will be used to denote γ-ray cascades from states with spins I_i to I_m to I_f.

2.1.2   Angular correlation function

The γ-γ angular correlation function $w^{\text{c.m.}}(\theta_1^{\text{c.m.}}, \theta_2^{\text{c.m.}}, \Phi)$ specifies the relative probability to observe, in the center-of-mass, a γ-ray transition from spin I_i to I_m at spherical angles θ_1 and ϕ_1 in coincidence with a γ-ray transition from spin I_m to I_f at spherical angles θ_2 and ϕ_2. Φ is defined as $\phi_1 - \phi_2$. θ_1 and θ_2 are measured with respect to the beam axis. The beam axis is the z-axis in the coordinate system used. The center-of-mass frame is the moving frame in which the γ rays are emitted. This is nearly identical to the projectile frame in the fragmentation, nucleon-knockout and

intermediate-energy Coulomb excitation reactions discussed here. For intermediate-energy Coulomb excitation this is a good approximation for light nuclei, but for heavy nuclei the projectile and center-of-mass frames should be distinguished. Thus, in the center-of-mass the angular correlation function has the form

$$
w^{\text{c.m.}}(\theta_1^{\text{c.m.}}, \theta_2^{\text{c.m.}}, \Phi) = \sum_{\substack{\lambda=0 \\ \lambda \text{ even}}}^{2l'} \sum_{\lambda_1=0}^{2I_i} \sum_{\lambda_2=0}^{2I_m} \frac{4\pi(-1)^{\lambda_1}}{\sqrt{2\lambda_2+1}} A_\lambda^{\lambda_2 \lambda_1}
$$
$$
\times A_{\lambda_2} B_{\lambda_1} \sum_{q=-\lambda}^{\lambda} \begin{pmatrix} \lambda_1 & \lambda & \lambda_2 \\ 0 & q & -q \end{pmatrix}
$$
$$
\times Y_\lambda^q(\theta_1^{\text{c.m.}}, \phi_1) Y_{\lambda_2}^{*-q}(\theta_2^{\text{c.m.}}, \phi_2). \tag{2.1}
$$

The $A_\lambda^{\lambda_2 \lambda_1}$ coefficients (defined in Eq. (2.6)) depend on I_i, I_m, l, l' and δ. The A_{λ_2} coefficients (defined in Eq. (2.9)) depend on I_m, I_f, l_{mf}, l'_{mf} and δ_{mf}. The multipole mixing ratios for the γ-ray transitions, δ and δ_{mf}, are defined in Eq. (2.7). The B_{λ_1} coefficients (defined in Eq. (2.11)) depend on I_i, I_{ii} and l_e. The $Y_\lambda^q(\theta_1^{\text{c.m.}}, \phi_1)$ and $Y_{\lambda_2}^{*-q}(\theta_2^{\text{c.m.}}, \phi_2)$ terms in Eq. (2.1) are spherical harmonics. To transform $w^{\text{c.m.}}(\theta_1^{\text{c.m.}}, \theta_2^{\text{c.m.}}, \Phi)$ from the moving frame in which the γ rays are emitted into the laboratory frame in which they are observed, two solid angle corrections are applied and the spherical harmonics are written as a function of the laboratory frame angles, θ_1 and θ_2. The angle Φ is not changed by the Lorentz transformation. Thus, in the laboratory frame $w^{\text{c.m.}}(\theta_1^{\text{c.m.}}, \theta_2^{\text{c.m.}}, \Phi)$ becomes

$$
w(\theta_1, \theta_2, \Phi) = \sum_{\substack{\lambda=0 \\ \lambda \text{ even}}}^{2l'} \sum_{\lambda_1=0}^{2I_i} \sum_{\lambda_2=0}^{2I_m} \frac{4\pi(-1)^{\lambda_1}}{\sqrt{2\lambda_2+1}} A_\lambda^{\lambda_2 \lambda_1}
$$
$$
\times A_{\lambda_2} B_{\lambda_1} \sum_{q=-\lambda}^{\lambda} \begin{pmatrix} \lambda_1 & \lambda & \lambda_2 \\ 0 & q & -q \end{pmatrix} Y_\lambda^q(\theta_1^{\text{c.m.}}, \phi_1)
$$
$$
\times Y_{\lambda_2}^{*-q}(\theta_2^{\text{c.m.}}, \phi_2) \frac{1-\beta^2}{[\beta\cos(\theta_1)-1]^2} \frac{1-\beta^2}{[\beta\cos(\theta_2)-1]^2}, \tag{2.2}
$$

where $\cos(\theta_1^{\text{c.m.}})$ and $\cos(\theta_2^{\text{c.m.}})$ can be transformed to $\cos(\theta_1)$ and $\cos(\theta_2)$ in the laboratory frame using the relation

$$\cos(\theta^{\text{c.m.}}) = \frac{\cos(\theta) - \beta}{1 - \beta \cos(\theta)}. \tag{2.3}$$

β is the velocity of the center-of-mass frame with respect to the laboratory frame relative to the speed of light. For $\beta = 0$, $w(\theta_1, \theta_2, \Phi)$ is equal to $w^{\text{c.m.}}(\theta_1^{\text{c.m.}}, \theta_2^{\text{c.m.}}, \Phi)$. The expressions for the angular correlation functions in Eqs. (2.1) and (2.2) are not normalized. The normalized angular correlation function in the laboratory frame has the form

$$
\begin{aligned}
W(\theta_1, \theta_2, \Phi) = & \sum_{\substack{\lambda=0 \\ \lambda \text{ even}}}^{2l'} \sum_{\lambda_1=0}^{2I_i} \sum_{\lambda_2=0}^{2I_m} \frac{4\pi(-1)^{\lambda_1}}{\sqrt{2\lambda_2+1}} A_\lambda^{\lambda_2\lambda_1} \\
& \times \frac{A_{\lambda_2} B_{\lambda_1}}{(4\pi)^2 B_0} \sum_{q=-\lambda}^{\lambda} \begin{pmatrix} \lambda_1 & \lambda & \lambda_2 \\ 0 & q & -q \end{pmatrix} Y_\lambda^q(\theta_1^{\text{c.m.}}, \phi_1) \\
& \times Y_{\lambda_2}^{*-q}(\theta_2^{\text{c.m.}}, \phi_2) \frac{1-\beta^2}{[\beta \cos(\theta_1) - 1]^2} \frac{1-\beta^2}{[\beta \cos(\theta_2) - 1]^2}
\end{aligned}
\tag{2.4}
$$

and is normalized to

$$\int_0^\pi \int_0^\pi \int_0^{2\pi} \int_0^{2\pi} W(\theta_1, \theta_2, \Phi)$$
$$\times \sin(\theta_1) \sin(\theta_2) \, d\phi_1 \, d\phi_2 \, d\theta_1 \, d\theta_2 = 1. \tag{2.5}$$

Thus, the probability of observing two γ-ray transitions in coincidence over all space is one. In Eq. (2.4), dividing by $(4\pi)^2 B_0$ fulfills the normalization condition in Eq. (2.5). If the population parameter $P(m)$ (introduced in Eq. 2.11 and defined for different reaction mechanisms in Section 2.5) is normalized then B_0 is unity. If $P(m)$ is not normalized, as in intermediate-energy Coulomb excitation discussed in Section 2.5.4, then dividing by B_0 is necessary to normalize the angular correlation function. In Eqs. (2.1), (2.2) and (2.4) the λ values are even because γ ray decay is an electromagnetic

14

process in which parity is conserved. λ_1 and λ_2 can have even or odd values but in order for the angular correlation function to be non-zero the sum of λ_1, λ_2 and λ must be even. If only the directional correlation of two γ rays is observed, as is discussed here, then λ_1 and λ_2 must be even as well as λ. Note that with the normalization used here, the $\lambda = \lambda_1 = \lambda_2 = 0$ term in the correlation function is $1/(4\pi)^2$, not unity, when $\beta = 0$. In Eqs. (2.1), (2.2) and (2.4), $A_\lambda^{\lambda_2\lambda_1}$ are generalized angular distribution coefficients with the form

$$
A_\lambda^{\lambda_2\lambda_1} = \frac{1}{1+\delta^2} \left[F_\lambda^{\lambda_2\lambda_1}(l, l, I_m, I_i) \right.
$$
$$
\left. +2\delta F_\lambda^{\lambda_2\lambda_1}(l, l', I_m, I_i) + \delta^2 F_\lambda^{\lambda_2\lambda_1}(l', l', I_m, I_i) \right].
\tag{2.6}
$$

These angular distribution coefficients consider only two multipolarities, l and $l' = l + 1$, contributing to the γ-ray transition from spin $I_i \rightarrow I_m$ corresponding to the lowest two multipolarities that are allowed by angular momentum coupling. For pure transitions where l is the only multipolarity that contributes to the γ-ray transition $A_\lambda^{\lambda_2\lambda_1} = F_\lambda^{\lambda_2\lambda_1}(l, l, I_m, I_i)$. The multipole mixing ratio, δ is defined as

$$
\delta = \frac{< I_m ||\pi(l+1)|| I_i >}{< I_m ||\pi'(l)|| I_i >},
\tag{2.7}
$$

where π and π' specify the type of radiation, electric or magnetic. δ_{mf} is defined likewise and is used in Eq. (2.9). The generalized F-coefficients in Eq. (2.6) are defined as

$$
F_\lambda^{\lambda_2\lambda_1}(l, l', I_m, I_i) = (-1)^{l'+\lambda_2+\lambda_1+1}(2I_m + 1)^{1/2}
$$
$$
\times(2I_i + 1)^{1/2}(2l + 1)^{1/2}(2l' + 1)^{1/2}(2\lambda + 1)^{1/2}
$$
$$
\times(2\lambda_2 + 1)^{1/2}(2\lambda_1 + 1)^{1/2}
\begin{pmatrix} l & l' & \lambda \\ 1 & -1 & 0 \end{pmatrix}
\begin{Bmatrix} I_m & l & I_i \\ I_m & l' & I_i \\ \lambda_2 & \lambda & \lambda_1 \end{Bmatrix}.
\tag{2.8}
$$

15

In Eqs. (2.1), (2.2) and (2.4), A_{λ_2} are angular distribution coefficients with the same form as Eq. (2.6), but with ordinary F-coefficients in place of the generalized F-coefficients and I_m, I_f, l_{mf}, l'_{mf} and δ_{mf} in place of I_i, I_m, l, l' and δ respectively. Thus, the A_{λ_2} coefficients have the form

$$A_{\lambda_2} = \frac{1}{1+\delta_{mf}^2} \left[F_{\lambda_2}(l_{mf}, l_{mf}, I_f, I_m) \right.$$
$$\left. +2\delta_{mf}F_{\lambda_2}(l_{mf}, l'_{mf}, I_f, I_m) + \delta_{mf}^2 F_{\lambda_2}(l'_{mf}, l'_{mf}, I_f, I_m) \right] \qquad (2.9)$$

with the ordinary F-coefficients defined as

$$F_\lambda(l_{mf}, l'_{mf}, I_f, I_m) = (-1)^{I_f + I_m + 1}(2\lambda + 1)^{1/2}$$
$$\times (2l_{mf} + 1)^{1/2}(2l'_{mf} + 1)^{1/2}(2I_m + 1)^{1/2}$$
$$\times \begin{pmatrix} l_{mf} & l'_{mf} & \lambda \\ 1 & -1 & 0 \end{pmatrix} \begin{Bmatrix} l_{mf} & l'_{mf} & \lambda \\ I_m & I_m & I_f \end{Bmatrix} . \qquad (2.10)$$

This is the limiting case of the generalized F-coefficients when only one γ ray is observed with respect to a fixed direction. The B_λ coefficients in Eqs. (2.1), (2.2) and (2.4), are orientation parameters which have the form

$$B_\lambda = (2\lambda + 1)^{1/2}(2I_i + 1)^{1/2} \sum_{m=-I_i}^{I_i} (-1)^{I_i + m}$$
$$\times \begin{pmatrix} I_i & I_i & \lambda \\ -m & m & 0 \end{pmatrix} P(m). \qquad (2.11)$$

As can be seen in Eq. (2.11), the B_λ coefficients are directly related to the population parameters $P(m)$, which specify the initial m substate distribution of a nucleus in an excited state with spin I_i and are related to the amount of alignment in the excited state. If a nucleus is in an excited state with 100% alignment, the angular momentum of the nucleus is fully oriented either perpendicular to or parallel and anti-parallel to
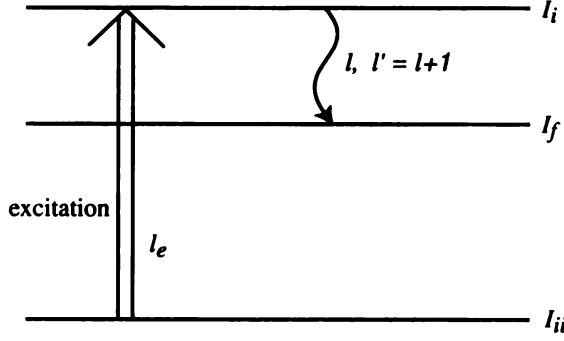
Figure 2.2: Notation used for angular distribution formalism. I_i and I_f are the initial (excited) and final spins of the γ-ray transition, respectively. The lowest possible multipolarities of the γ-ray transition are l and $l' = l + 1$. I_{ii} is the spin of the initial state before the nucleus is excited and l_e is the orbital angular momentum of the excitation.

the beam axis. A percentage of alignment quoted as less than 100% is measured or calculated with respect to the B_2 value for the fully aligned cases.

2.2 Angular distribution function

The γ-ray angular distribution function is a specific case of the γ-γ angular correlation function in which only one γ ray is observed. It is the same as if the γ-ray transition from spins $I_m \rightarrow I_f$ in Fig. 2.1 is not observed. Therefore, Fig. 2.2 shows the comparable notation if just one γ ray is observed from spins $I_i \rightarrow I_f$. Throughout this work the notation $W(\theta_1, \theta_2, \Phi)$ containing θ_1, θ_2 and Φ will indicate a γ-γ angular correlation function and $W(\theta)$ will indicate a γ-ray angular distribution.

The γ-ray angular distribution function $w^{c.m.}(\theta^{c.m.})$ specifies the relative probability to observe, in the center of mass, a γ-ray transition from spin I_i to I_f at an angle $\theta^{c.m.}$ with respect to the beam axis and has the form

$$w^{c.m.}(\theta^{c.m.}) = \sum_{\substack{\lambda=0 \\ \lambda \text{ even}}}^{2l'} A_\lambda B_\lambda P_\lambda(\cos(\theta^{c.m.})). \qquad (2.12)$$

The A_λ coefficients depend on l, l', I_i and I_f. They are a special case of the generalized

angular distribution coefficients (defined in Eq. 2.6) where λ_1 and λ_2 are equal to zero. The A_λ coefficients are defined in Eq. 2.9, but for the $I_m \rightarrow I_f$ transition as needed for the γ-γ angular correlation function. Therefore the A_λ coefficients as needed for the γ-ray angular distribution function can be calculated by replacing, λ_2, δ_{mf}, l_{mf}, l'_{mf} and I_m with λ, δ, l, l' and I_i, respectively. The B_λ coefficients (defined in Eq. 2.11) depend on I_{ii}, I_i and l_e. The $P_\lambda(\cos(\theta^{c.m.}))$ terms in Eq. 2.12 are Legendre polynomials. The γ-γ angular correlation function in Eq. 2.4 contains spherical harmonics. Spherical harmonics can be written in terms of associated Legendre polynomials. The initial excited state has axial symmetry about the quantization axis (in ϕ), so q (in Eq. 2.4) is equal to zero. This reduces the spherical harmonics to the Legendre polynomials seen in Eq. 2.12. To Lorentz boost $w^{c.m.}(\theta^{c.m.})$ into the laboratory frame, a solid angle correction is applied and the Legendre polynomials are written as a function of the laboratory frame angle θ with respect to the beam axis. Thus,

$$w(\theta) = \sum_{\substack{\lambda=0 \\ \lambda \text{ even}}}^{2l'} A_\lambda B_\lambda P_\lambda(\cos(\theta^{c.m.})) \frac{1 - \beta^2}{(\beta \cos(\theta) - 1)^2}, \qquad (2.13)$$

where $\cos(\theta^{c.m.})$ can be transformed to $\cos(\theta)$ in the laboratory frame using the relation found in Eq. 2.3. For $\beta = 0$, $w(\theta)$ is equal to $w^{c.m.}(\theta^{c.m.})$.

The angular distribution functions in Eqs. 2.12 and 2.13 are not necessarily normalized. Dividing by $4\pi A_0 B_0$ normalizes $w(\theta)$ and $w^{c.m.}(\theta^{c.m.})$ to unity, with respect to integrating over all space, because the even Legendre polynomials of order two and greater integrate to zero over the interval $0 \le \theta \le \pi$. As with the normalized γ-γ angular correlation function (Eq. 2.4), if the presented formulas are used and $P(m)$ is normalized, then A_0 and B_0 are unity. The normalized angular distribution function

18

$W(\theta)$ has the form

$$W(\theta) = \frac{w(\theta)}{4\pi A_0 B_0} \;\; = \;\; \frac{1}{4\pi} \left[1 + \sum_{\substack{\lambda=2 \\ \lambda \text{ even}}}^{2l'} \frac{A_\lambda B_\lambda P_\lambda(\cos(\theta^{c.m.}))}{A_0 B_0} \right]$$
$$\times \frac{1 - \beta^2}{(\beta\cos(\theta) - 1)^2}, \qquad (2.14)$$

and is normalized to

$$2\pi \int_0^\pi W(\theta)\sin(\theta)\,d\theta = 1. \qquad (2.15)$$

Normalizing $w^{c.m.}(\theta^{c.m.})$ is similarly performed. The sums in Eqs. 2.12, 2.13 and 2.14 extend to twice the multipolarity of the γ-ray transition, $l' = l + 1$, with the odd λ terms equal to zero.

As introduced in Eq. 2.11, the B_λ coefficients contain the population parameters $P(m)$ which are related to the amount of alignment in an excited state. Both the amount of alignment in an excited state and the velocity of the center-of-mass frame with respect to the laboratory frame can affect the resulting γ-γ angular correlation or γ-ray angular distribution. Fig. 2.3 illustrates the effect of the Lorentz boost on $W(\theta)$ for beam velocities of $\beta = 0.4$ and $\beta = 0.6$ with 100% oblate or prolate alignment, defined in Section 2.3. It will be seen that a Lorentz boost for $\beta = 0.4$ or 0.6 has a smaller effect on $W(\theta)$ than a reduction in the alignment of an excited state. The amount of alignment in an excited state and the Lorentz boost are independent and have different effects on $W(\theta)$ and $W(\theta_1, \theta_2, \Phi)$. A reduction in the amount of alignment in an excited state reduces the anisotropy of $W(\theta)$ (and changes the anisotropy of $W(\theta_1, \theta_2, \Phi)$) and a Lorentz boost forward focuses $W(\theta)$ and $W(\theta_1, \theta_2, \Phi)$.

2.3 Alignment

For an unoriented initial state (one with no alignment in the initial excited state) a γ-ray angular distribution shows no anisotropy, but a γ-γ angular correlation can show
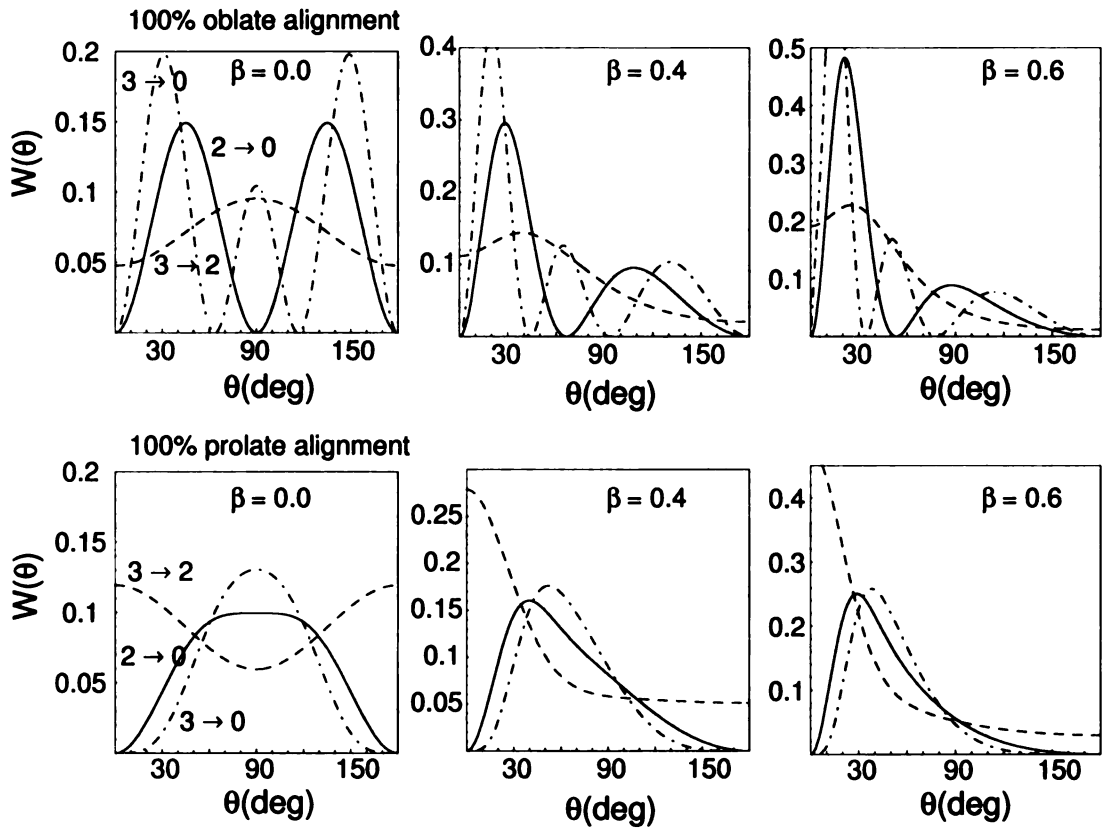
Figure 2.3: Plots of $W(\theta)$ at $\beta = 0.0$, 0.4 and 0.6 for quadrupole (solid curves), dipole (dashed curves) and octupole (dash-dotted curves) transitions with 100% oblate or prolate alignment.

0% alignment
Laboratory frame (β = 0.4)
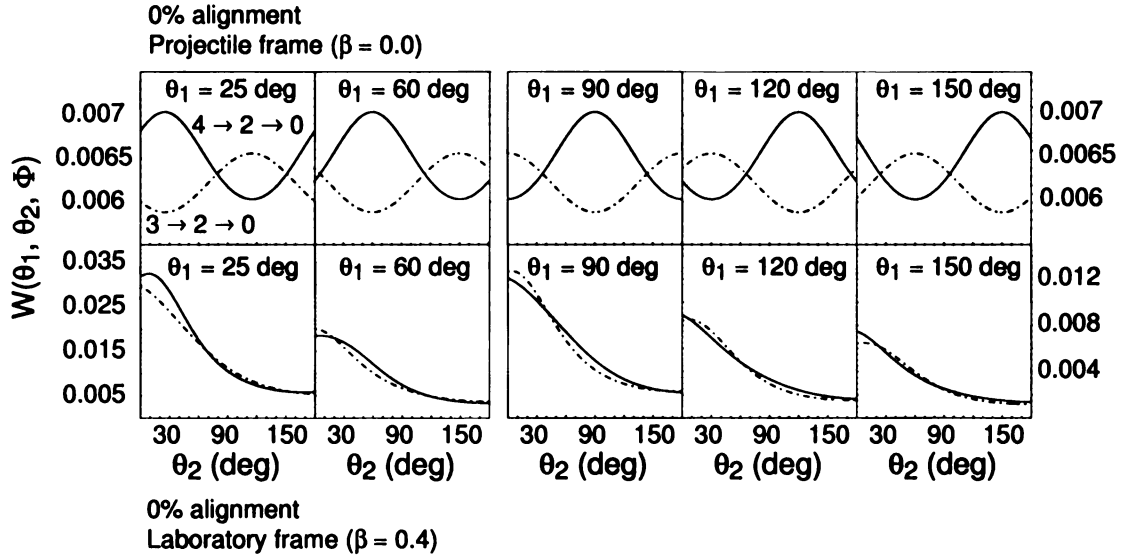
Figure 2.4: Plots of $W(\theta_1, \theta_2, \Phi)$ for $4 \to 2 \to 0$ (solid curves) and $3 \to 2 \to 0$ (dash-dotted curves) correlations at $\beta = 0$ (top row) and $\beta = 0.4$ (bottom row) with no alignment. In each plot Φ and θ_1 are fixed; $\Phi \equiv \phi_1 - \phi_2 = 0°$ and the value of θ_1 is as labeled on each plot. The angular correlation function, $W(\theta_1, \theta_2, \Phi)$, is normalized as in Eq. 2.5.

a large amount of anisotropy. In Fig. 2.4, $W(\theta_1, \theta_2, \Phi)$ is shown for spin transitions $4 \to 2 \to 0$ and $3 \to 2 \to 0$ with no alignment and beam velocities of $\beta = 0$ and $\beta = 0.4$. The $4 \to 2$ and $2 \to 0$ transitions are taken to be pure quadrupole transitions. The $3 \to 2$ transition is taken to be a pure dipole transition and the $2 \to 0$ transition is taken to be a pure quadrupole transition. For all the γ-γ angular correlation plots in this chapter Φ is equal to $0°$. This was chosen because the dependence of Φ on $W(\theta_1, \theta_2, \Phi)$ is such that the maximum anisotropy of $W(\theta_1, \theta_2, \Phi)$ occurs for $\Phi = 0°, 180°, ...$ when $\beta = 0$. The $4 \to 2 \to 0$ and $3 \to 2 \to 0$ correlations can be easily distinguished when $\beta = 0$. For $\beta = 0.4$ the relative difference between the $4 \to 2 \to 0$ and $3 \to 2 \to 0$ correlation functions, seen in Fig. 2.4, is as large as 20% when $\theta_1 = \theta_2$.

The alignment produced in a nucleus in an excited state can be one of two types. If the angular momentum of the nucleus is aligned perpendicular to the beam axis, then the $m = 0$ substates are preferentially populated. This alignment, referred to as oblate, is observed in fusion-evaporation (heavy-ion, xn) reactions. If the angular momentum of the nucleus is aligned parallel and anti-parallel to the beam axis, then

21

the $m = \pm I_i$ substates are preferentially populated. This is referred to as prolate alignment. A prolate-aligned nucleus produces a different γ-ray angular distribution or γ-γ angular correlation for a given γ-ray transition than an oblate-aligned nucleus. Three-dimensional plots of W(θ) are shown in Fig. 2.5. The top row shows a pure quadrupole transition, the middle row a pure dipole transition and the bottom row a pure octupole transition. The first column shows the transitions at rest with 100% oblate alignment. The second column shows the transitions at $\beta = 0.4$ with 100% oblate alignment. The third column shows the transitions at $\beta = 0.4$ with 20% oblate alignment. As can be seen in the third column of Fig. 2.5, a reduction in the percentage of alignment combined with a Lorentz boost for $\beta = 0.4$ washes out much of the anisotropy in the γ-ray angular distribution. A similar reduction in anisotropy occurs in the γ-ray angular distribution for a prolate aligned nucleus. However, distinguishing quadrupole, dipole and octupole transitions is still experimentally possible and will be discussed quantitatively in section 2.5. In Chapters 4 and 5 experimental γ-ray angular distributions will be shown and discussed.

The percentage of alignment for an initial excited state, I_i, given the population parameters $P(m)$, is defined as follows for prolate and oblate alignment. For prolate alignment,

$$A_p = \sum_{n=-I_i}^{I_i} \frac{3n^2 - I_i(I_i + 1)P(n)}{I_i(2I_i - 1)} \times 100. \qquad (2.16)$$

For oblate alignment,

$$A_o^{int} = \sum_{n=-I_i}^{I_i} \frac{3n^2 - I_i(I_i + 1)P(n)}{I_i(I_i + 1)} \times 100 \qquad \text{for } I_i \text{ integer,} \qquad (2.17)$$

$$A_o^{half-int} = \sum_{n=-I_i}^{I_i} \frac{3n^2 - I_i(I_i + 1)P(n)}{I_i(I_i + 1) - 3/4} \times 100 \qquad \text{for } I_i \text{ half-integer.} \qquad (2.18)$$

22
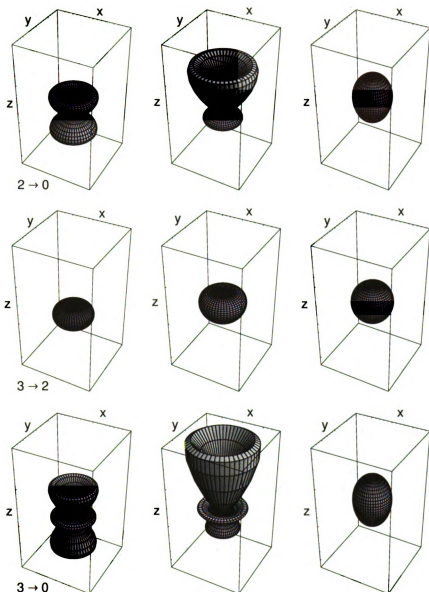
Figure 2.5: Three-dimensional γ-ray angular distributions for three γ-ray transitions from an initial state with oblate alignment. The top row of figures shows pure quadrupole transitions (2→0), the middle row shows pure dipole transitions (3→2) and the bottom row shows pure octupole transitions (3→0). The first column shows all three transitions, quadrupole, dipole and octupole, at $\beta = 0.0$ with 100% oblate alignment. The second column shows the same transitions Lorentz boosted for $\beta = 0.4$. The third column shows the same transitions Lorentz boosted for $\beta = 0.4$ and with the alignment reduced to 20% oblate alignment. In all the plots, the beam axis is the z-axis (up is positive z) with the beam direction towards positive z.

23
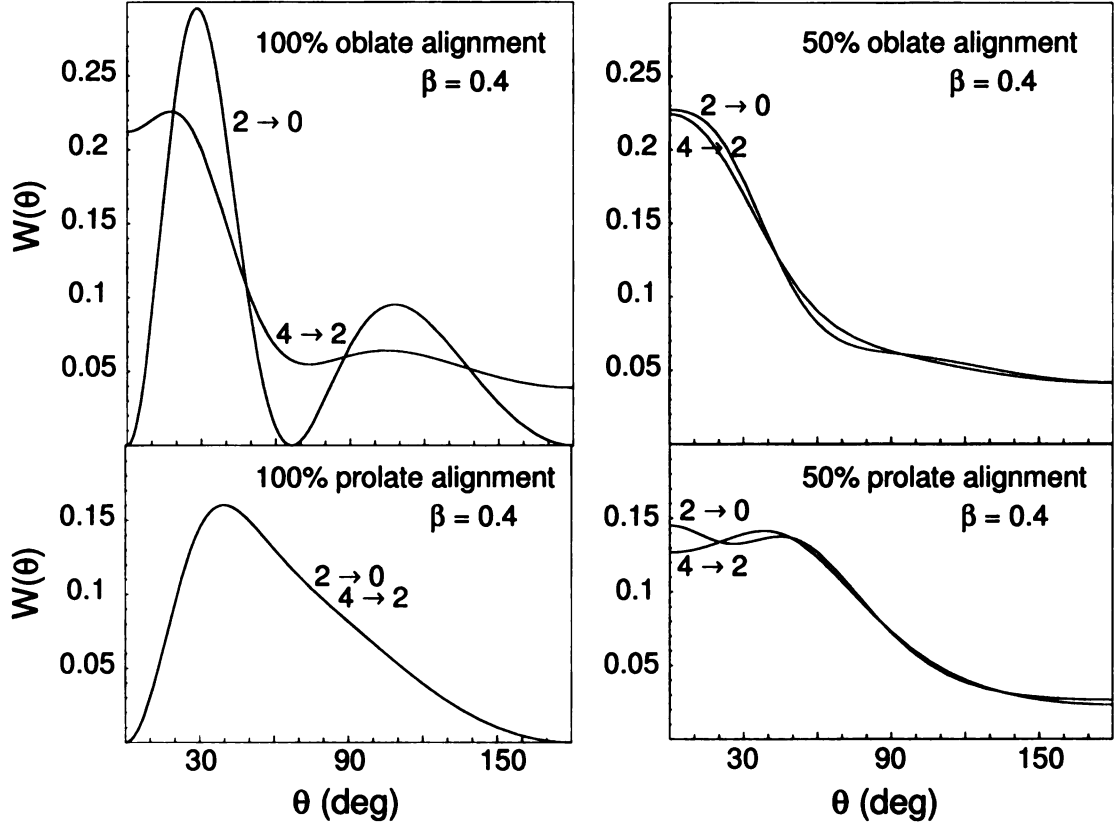
Figure 2.6: Plots of $W(\theta)$ for 100% and 50% oblate or prolate alignment for two different quadrupole transitions at $\beta = 0.4$. The top row shows that 4→2 and 2→0 transitions are significantly different at 100% oblate alignment. However, at 50% alignment they are similar. The bottom row shows that 4→2 and 2→0 transitions are identical with 100% prolate alignment and at 50% alignment they are similar. The dipole transitions, 3→2 and 1→0, and the octupole transitions, 6→3 and 3→0, behave similarly to the two quadrupole transitions shown.

2.4 $W(\theta)$ for transitions of identical multipolarity

Examples of 4→2 and 2→0 quadrupole transitions at 100% and 50% oblate or prolate alignment are shown in Fig. 2.6. For 100% prolate alignment different spin $I_i \rightarrow I_f$ transitions with the same multipolarity are nearly identical at $\beta = 0.4$. Angular distributions for quadrupole 2→0 and 4→2 transitions are equivalent, for dipole 3→2 and 1→0 are equivalent and for octupole 6→3 and 3→0 are equivalent. However, for 100% oblate alignment those same three pairs of transitions are significantly different. The 1→0, 2→0 and 3→0 transitions vanish at the origin and have more features than

the 3→2, 4→2 and 6→3 transitions, respectively. As the amount of oblate alignment decreases, the same-multipolarity different-spin $I_i \rightarrow I_f$ transitions become more alike. As the amount of prolate alignment decreases, same-multipolarity different-spin $I_i \rightarrow I_f$ transitions do not all approach an isotropic Lorentz-boosted distribution the same way, but the differences between those same multipolarity transitions are small enough not to impede distinguishing quadrupole, dipole and octupole transitions.

2.5   Different reaction mechanisms

In an in-beam experiment, partial alignments will be observed. Four reaction mechanisms, namely fusion evaporation, fragmentation, nucleon-knockout and intermediate-energy Coulomb excitation, will be discussed in this chapter. The latter three have become standard in-beam spectroscopy tools with γ-ray detection, using intermediate-energy ($\beta = 0.3$–0.8) exotic beams, but have not been thoroughly explored. Fragmentation reactions were pioneered in 1979 [55], but did not utilize γ-ray detection in the early implementations. Nuclear break-up reactions (including fragmentation and nucleon-knockout reactions) were first used in conjunction with the detection of γ-rays as a spectroscopic tool in three pioneering experiments [37, 56, 57]. The first intermediate-energy Coulomb excitation experiments were performed in 1995 [10, 56].

2.5.1   Fusion evaporation

Non-relativistic fusion evaporation reactions will first be discussed. Yamazaki [58] approximated the population parameter $P(m)$, in Eq. 2.11, for non-relativistic (heavy-ion, xn) reactions using a Gaussian distribution centered at $m = 0$, based upon work done by Diamond *et al.* [59]. Normalized, $P(m)$ then has the form

$$P(m) = \frac{e^{-m^2/2\sigma^2}}{\displaystyle\sum_{n=-I_i}^{I_i} e^{-n^2/2\sigma^2}}.$$

(2.19)

The width of the Gaussian distribution, σ, is related to the amount of oblate alignment in the excited state. For an excited state with less than 100% alignment, $\sigma > 0$ such that $B_2/B_2^{max} \times 100$ is equal to the percentage of alignment, where B_2^{max} is the B_2 coefficient corresponding to the fully aligned case. The percent of alignment, in terms of $P(m)$, is defined in Eqs. 2.16 and 2.17. We have reproduced the tabulated angular distribution coefficients of Yamazaki [58] and der Mateosian and Sunyar [60]. A reduction in the amount of alignment produced in a nucleus in an excited state significantly decreases the anisotropy of the γ-ray angular distribution as seen previously for oblate alignment in Fig. 2.5.

2.5.2 Fragmentation reactions

With the intermediate-energy beams available today, fragmentation reactions have become a spectroscopic tool for creating and studying exotic nuclei. In fragmentation reactions the amount and type of alignment produced is not well studied. Investigations of alignment and polarization produced in intermediate-energy fragmentation reactions [61–64] are not consistent. The alignment produced in [62–64] ranges from less than 1% to 35%. In the experiment where less than 1% alignment was produced [62], the fragment was five protons and ten neutrons removed from the incoming projectile, so little alignment was expected. Each of the 15 nucleons carried off some amount of linear and angular momentum in a random direction, thus leaving the fragment with a significantly lower angular momentum and destroying the alignment. Reactions using intermediate-energy beams were $^9\mathrm{Be}(^{22}\mathrm{Ne},^{18}\mathrm{N})X$ [62], $^9\mathrm{Be}(^{18}\mathrm{O},^{14}\mathrm{B}\ \gamma)X$ [64], $^{12}\mathrm{C}(^{13}\mathrm{C},^{12}\mathrm{B})X$ [62] and $^9\mathrm{Be}(^{46}\mathrm{Ti},^{43m}\mathrm{Sc}\ \gamma)X$ [63]. The first two reactions were performed at 60 MeV/nucleon and were $3p1n$ removal reactions. In those two reactions, 14.4% prolate alignment and less than 5% prolate or oblate alignment, respectively, were observed in the center of the longitudinal momentum distribution. In the wings of the momentum distributions, oblate alignment was observed in both experiments. In $^{12}\mathrm{C}(^{13}\mathrm{C},^{12}\mathrm{B})X$ [62], 4.7% prolate alignment was observed in the center of the momen-

tum distribution. In $^9\text{Be}(^{46}\text{Ti},^{43m}\text{Sc}\ \gamma)X$ [63], performed at 500 MeV/nucleon, 35%
prolate alignment was observed in the center of the momentum distribution and 15%
oblate alignment was observed in the wing of the momentum distribution. Though
the magnitudes of the alignment observed differ significantly, the type of alignment
produced as a function of the longitudinal momentum distribution is consistent. In
[62–64] the alignments produced from the reactions were prolate in the center of the
momentum distributions and oblate in the wings (or tail) of the momentum distribu-
tions. This can be understood in terms of a simple kinematical model [63, 64] where
the projectile fragment acts as a spectator while the nucleons in the overlapping vol-
ume with the target are removed. The outgoing momentum of the fragment is then
directly related to the angular momentum of the fragment, thus giving prolate or
oblate alignment values. Reactions where more nucleons are removed have broader
momentum distributions [65]. Thus the m substate distributions are flatter, resulting
in less alignment. This supports the result in [62] where 15 nucleons were removed and
less than 1% alignment was observed. In contrast to the above experiments, in [61] an
alignment of 30%–70% was observed, though the type of alignment was not reported.
The reaction was $^9\text{Be}(^{48}\text{Ca},^{46}\text{Ar}\ \gamma)X$ at 60.3 MeV/nucleon. In addition to ^{46}Ar, many
of the fragments from the reaction were analyzed. In order to reproduce the approx-
imate ratios of the γ-ray intensities of the quadrupole and dipole transitions in Fig.
2 of [61], we had to assume oblate alignment. The ratios observed in [61] seem to be
incompatible with any percentage of prolate alignment.

Extending the formalism of Yamazaki [58] and Diamond $et\ al.$ [59] for oblate
population distributions, two Gaussian distributions centered at $m = \pm\ I_i$ are used for
approximating prolate alignment in fragmentation reactions [54]. Normalized, $P(m)$
then has the form

$$P(m) = \frac{e^{-(I_i-|m|)^2/2\sigma^2}}{\displaystyle\sum_{n=-I_i}^{I_i} e^{-(I_i-|n|)^2/2\sigma^2}}. \tag{2.20}$$

27

Table 2.1: Relative difference of $W(\theta)$ between a quadrupole, 2→0, and dipole, 3→2, transition (with respect to the dipole transition) for 20% oblate or prolate alignment at $\beta = 0.4$ and 0.6 for a few selected angles, θ, with respect to the beam axis. The angles were selected to sample the range of angles from 0° to 180°.

β	θ	Relative difference (%)	
		Oblate	Prolate
0.4	0°	22.5	9.4
	25°	10.7	13.7
	60°	10.7	16.8
	150°	18.9	12.4
0.6	0°	22.5	9.4
	25°	4.7	10.0
	60°	10.5	16.4
	150°	20.4	11.3

In fragmentation reactions the target is viewed as a means of removing nucleons from the projectile. Thus, we consider the center-of-mass frame to be the projectile frame. In order for γ-ray angular distributions to be a useful experimental tool for measuring γ-ray multipolarities and thus spins of excited states, there must be enough alignment in the excited state to distinguish between different multipolarity transitions. As the amount of alignment decreases, the difference between the angular distribution curves for different multipolarity γ-ray transitions decreases as both curves approach Lorentz-boosted, isotropic distributions. Typical intermediate-energy beam velocities (NSCL, RIKEN, GANIL, GSI) are between $0.3c$ and $0.8c$. At the proposed RIA facility [66], beams will have velocities of approximately $0.6c$. Figs. 2.7 and 2.8 show plots of $W(\theta)$ calculated with 50%, 20% and 10% oblate and prolate alignment, respectively, for quadrupole, dipole and octupole transitions. The plots are shown for incoming beam velocities of $0.4c$ and $0.6c$. Table 2.1 lists the relative difference between the quadrupole and dipole transitions with 20% alignment, as seen in Figs. 2.7 and 2.8, for selected angles. Table 2.1 illustrates that for a fragmentation reaction where only 20% prolate or oblate alignment is produced the difference between a quadrupole and dipole transition is large enough to distinguish between the two and to make the measurement of γ-ray angular distributions experimentally feasible. To
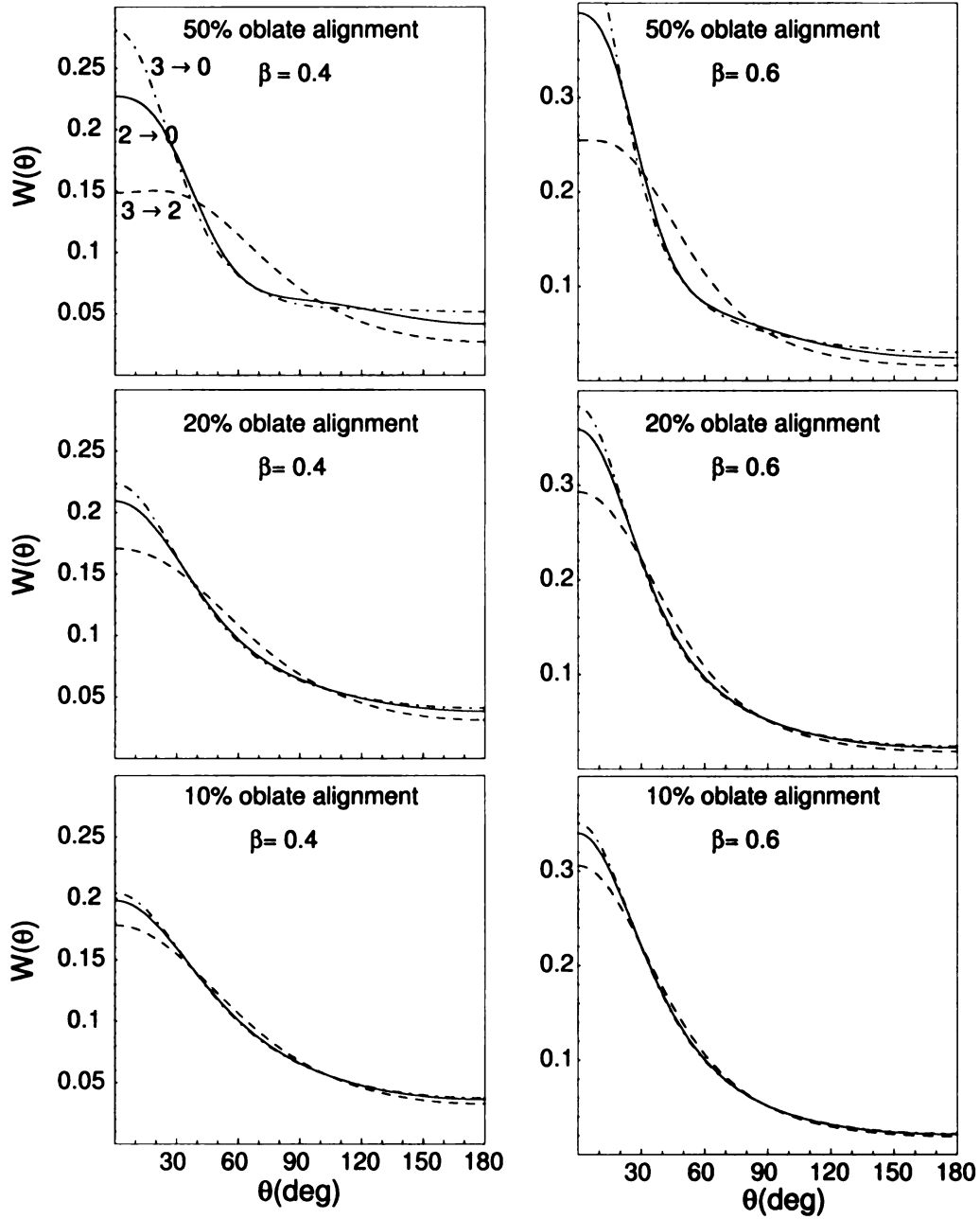
Figure 2.7: Plots of $W(\theta)$ for 50%, 20% and 10% oblate alignment with an incoming beam velocity of $0.4c$ (left column) and $0.6c$ (right column). Quadrupole transitions (solid curves), dipole transitions (dashed curves) and octupole transitions (dashdotted curves) are shown. The order of the transitions, as labeled on the upper left plot, is the same for all of the plots in the figure.

29
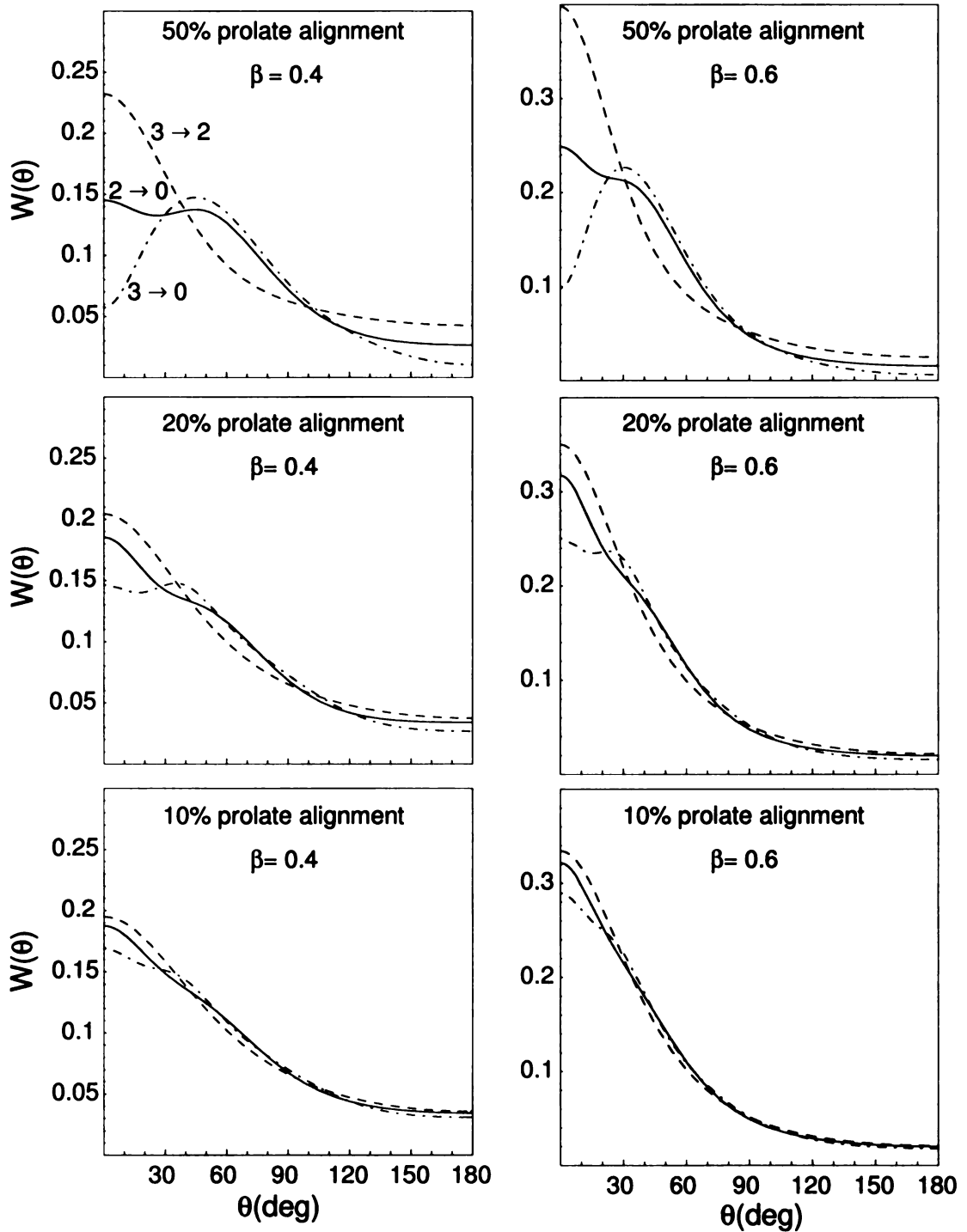
Figure 2.8: Plots of $W(\theta)$ for 50%, 20% and 10% prolate alignment with an incoming beam velocity of $0.4c$ (left column) and $0.6c$ (right column). Quadrupole transitions (solid curves), dipole transitions (dashed curves) and octupole transitions (dash-dotted curves) are shown. The order of the transitions, as labeled on the upper left plot, is the same for all of the plots in the figure.

30

better illustrate the large effect of the percentage of alignment on $W(\theta)$, $W(\theta)$ is shown for quadrupole, dipole and octupole transitions with 100%, 50%, 20%, 10% and 0% oblate and prolate alignment in Figs. 2.9 and 2.10, respectively, at $\beta = 0.4$ and 0.6. The curves with 0% alignment are isotropic, Lorentz-boosted distributions. The curves with the most features correspond to 100% alignment. A reduction in the percentage of alignment has a much larger effect on $W(\theta)$ than a Lorentz boost for $\beta = 0.4$ or 0.6.

For $P(m)$ approximated by a Gaussian distribution(s), transitions with a given multipolarity but different spins $I_i \to I_f$ are similar for approximately 50% oblate or prolate alignment. Thus stretched quadrupole, dipole and octupole transitions can be distinguished from one another. In this chapter, the same amount of alignment in all excited states has been assumed in comparing different multipolarity transitions. Fragmentation reactions may produce different percentages of alignment for different initial spins, I_i, in the same nucleus. However, such differences are likely to be small and would only lead to ambiguities if one state was prolate-aligned and another state was oblate-aligned — a situation that is unprecedented.

To distinguish quadrupole, dipole and octupole transitions proper care must be given to detector placement. At the angles around 40° and 100°, $W(\theta)$ is the same for different multipolarity transitions at $\beta = 0.4$. Avoiding the range of angles around 40° and 100°, the relative difference between a quadrupole (2→0) and dipole (3→2) transition is on the order of 10–20% for fragmentation reactions with 20% prolate or oblate alignment at $\beta = 0.4$. A minimum of approximately 600 counts with negligible background, corresponding to an uncertainty of ±4%, in the γ-ray peak at a given angle is needed to distinguish between a quadrupole and dipole transition that are 10% different at that angle. See Sect. 3.3.1 for the discussion of the detector setup for the experiments performed.

The previous discussions of fragmentation reactions and alignment also apply to γ-γ angular correlations. Figs. 2.11 and 2.12 show γ-γ angular correlations for
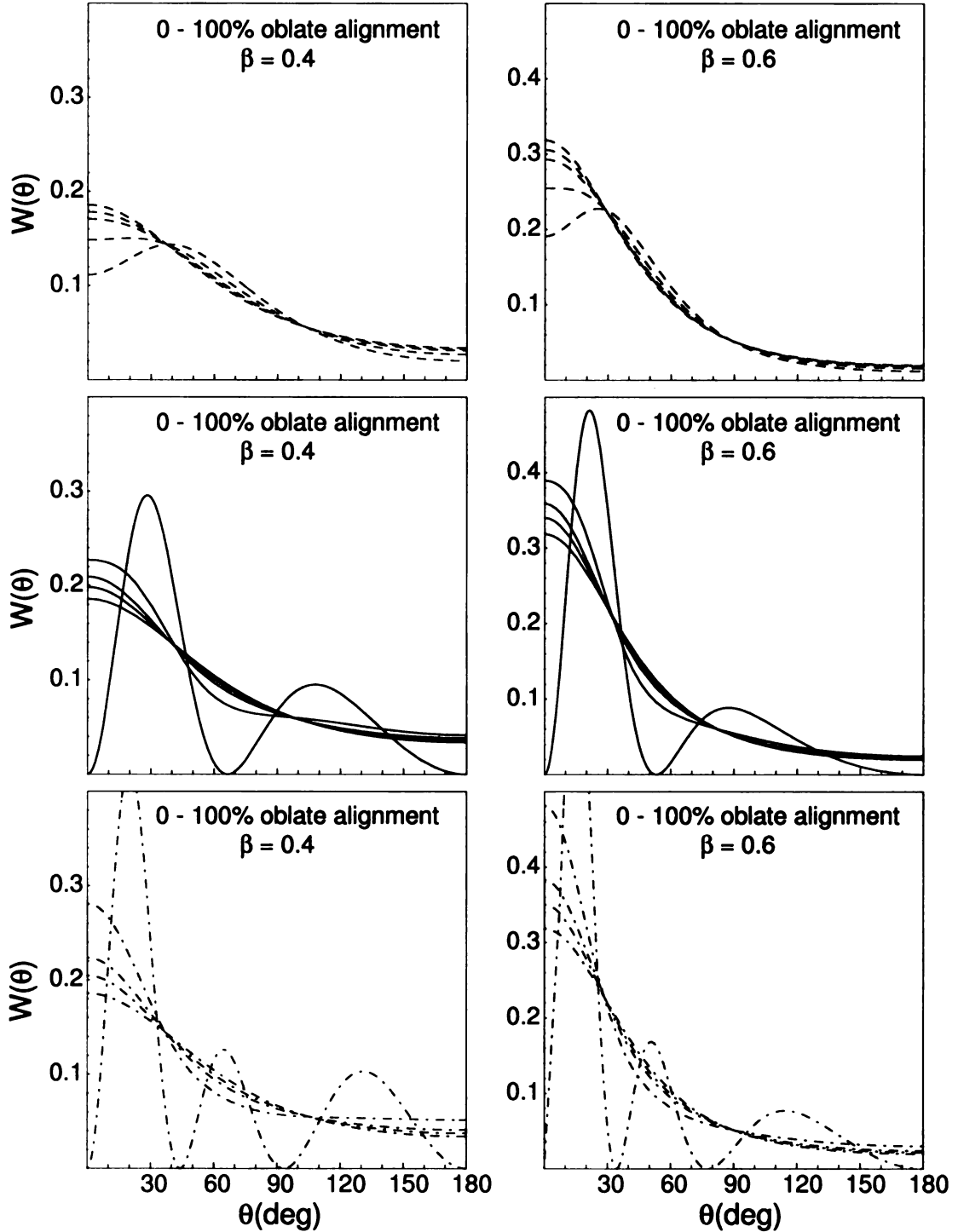
Figure 2.9: Plots of $W(\theta)$ for dipole ((3→2), dashed curves, top row), quadrupole ((2→0), solid curves, middle row) and octupole ((3→0), dash-dotted curves, bottom row) transitions, each with 100%, 50%, 20%, 10% and 0% oblate alignment at $\beta = 0.4$ (left column) and 0.6 (right column). The curves with the most features are those corresponding to 100% alignment. The flatter curves are those corresponding to 0% alignment (an isotropic Lorentz-boosted distribution.)

32
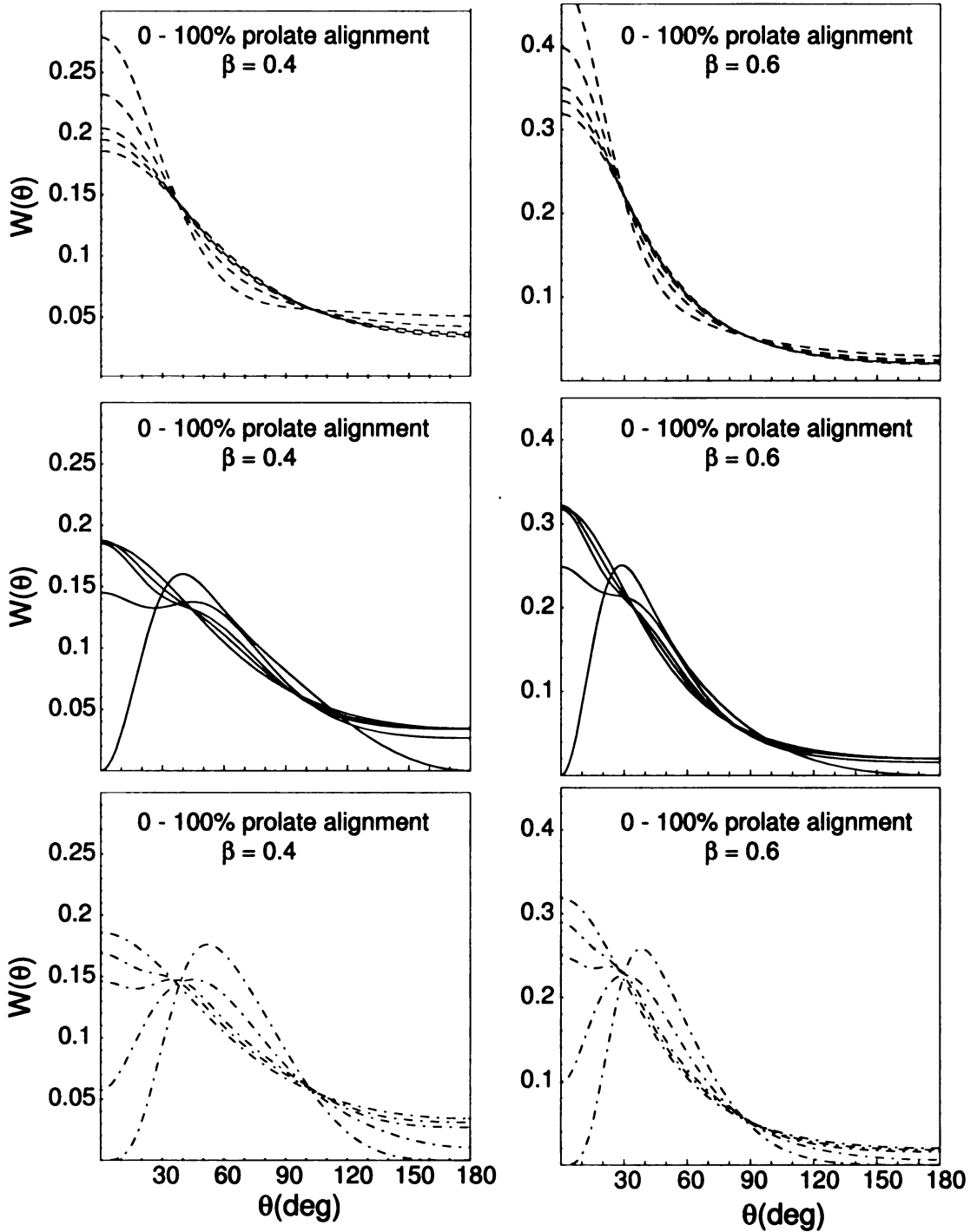
Figure 2.10: Plots of $W(\theta)$ for dipole ((3→2), dashed curves, top row), quadrupole ((2→0), solid curves, middle row) and octupole ((3→0), dash-dotted curves, bottom row) transitions, each with 100%, 50%, 20%, 10% and 0% prolate alignment at $\beta = 0.4$ (left column) and 0.6 (right column). The curves with the most features are those corresponding to 100% alignment. The flatter curves are those corresponding to 0% alignment (an isotropic Lorentz-boosted distribution.)

20% oblate alignment
Laboratory frame (β = 0.4)
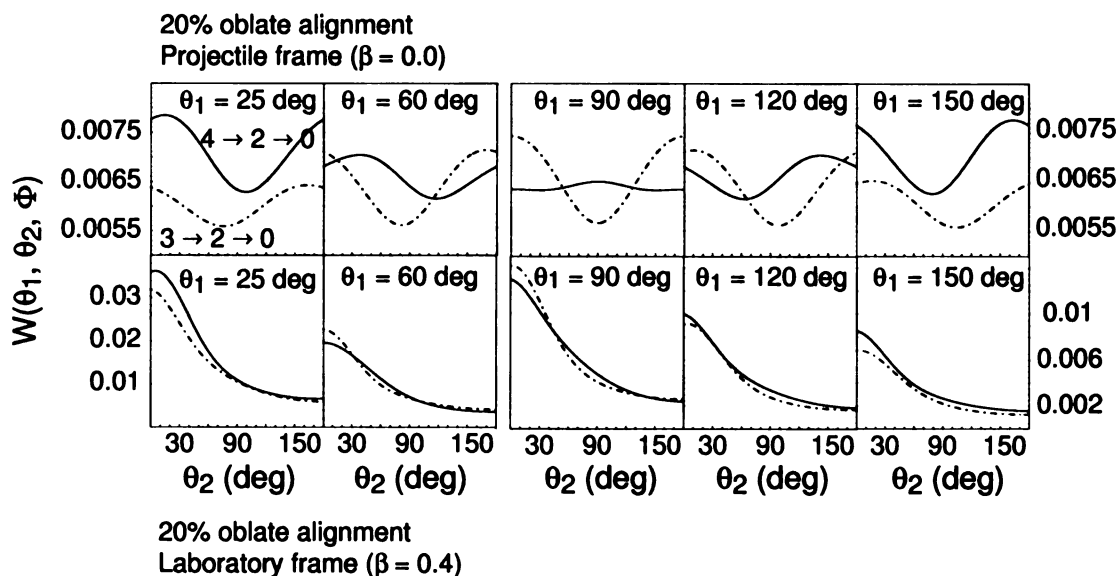
Figure 2.11: Plots of $W(\theta_1, \theta_2, \Phi)$ for $4 \to 2 \to 0$ (solid curves) and $3 \to 2 \to 0$ (dash-dotted curves) correlations at $\beta = 0$ (top row) and $\beta = 0.4$ (bottom row) with 20% oblate alignment. In each plot Φ and θ_1 are fixed; $\Phi \equiv \phi_1 - \phi_2 = 0°$ and the value of θ_1 is as labeled on each plot. The angular correlation function, $W(\theta_1, \theta_2, \Phi)$, is normalized as in Eq. 2.5.

20% prolate alignment
Projectile frame (β = 0.0)

20% prolate alignment
Laboratory frame (β = 0.4)
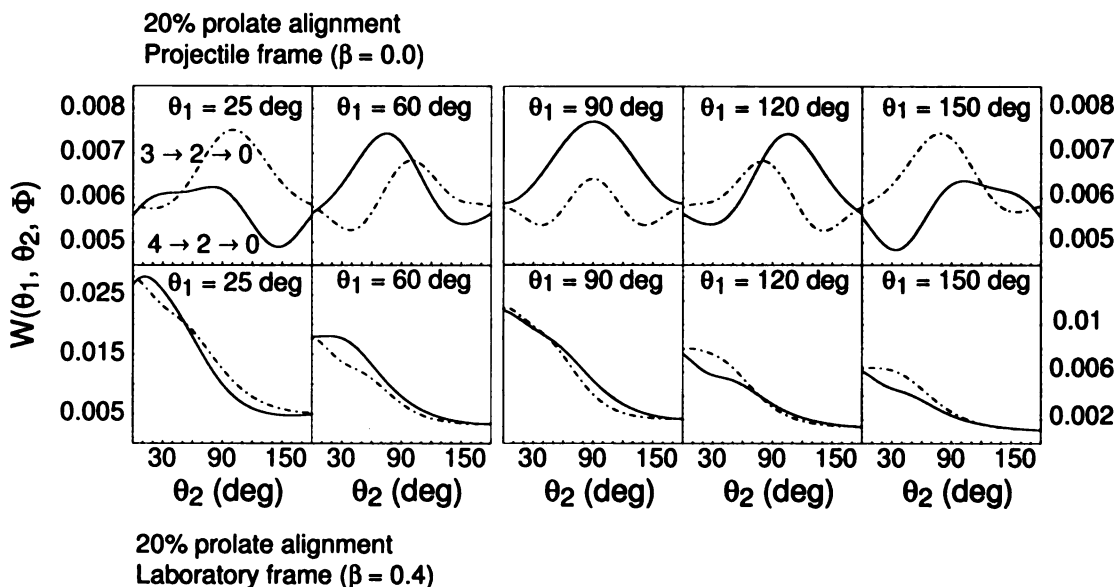
Figure 2.12: Plots of $W(\theta_1, \theta_2, \Phi)$ for $4 \to 2 \to 0$ (solid curves) and $3 \to 2 \to 0$ (dash-dotted curves) correlations at $\beta = 0$ (top row) and $\beta = 0.4$ (bottom row) with 20% prolate alignment. In each plot Φ and θ_1 are fixed; $\Phi \equiv \phi_1 - \phi_2 = 0°$ and the value of θ_1 is as labeled on each plot. The angular correlation function, $W(\theta_1, \theta_2, \Phi)$, is normalized as in Eq. 2.5.

34

$4 \rightarrow 2 \rightarrow 0$ and $3 \rightarrow 2 \rightarrow 0$ transitions at $\beta = 0$ and $\beta = 0.4$ with 20% oblate or 20% prolate alignment, respectively. The larger the reaction induced alignment in an excited state, the greater the anisotropy in the γ-γ angular correlation.

For nuclei with 20% oblate or prolate alignment at $\beta = 0.4$, as seen in Figs. 2.11 and 2.12, the relative difference between the $4 \rightarrow 2 \rightarrow 0$ and $3 \rightarrow 2 \rightarrow 0$ correlation functions is as large as approximately 30%. A minimum of approximately 50 counts with negligible background, corresponding to an uncertainty of $\pm 14\%$, in the γ-ray peak at a given set of angles (θ_1, θ_2 and $\Phi = 0°$) would be needed to distinguish between a $4 \rightarrow 2 \rightarrow 0$ and $3 \rightarrow 2 \rightarrow 0$ correlation where the correlation function, $W(\theta_1, \theta_2, \Phi)$ differs by 30%. To give a specific example, measuring $4 \rightarrow 2 \rightarrow 0$ and $3 \rightarrow 2 \rightarrow 0$ correlations from nuclei with 20% oblate alignment could be accomplished by having detectors at the following angles: 17°, 29°, 88°, 102°, 112°, 139° and 155°. For $(\theta_1, \theta_2, \Phi) = (17°, 29°, 0°)$ the relative difference between the $4 \rightarrow 2 \rightarrow 0$ and $3 \rightarrow 2 \rightarrow 0$ correlation functions is 28%. Likewise, for $(102°, 88°, 0°)$ the relative difference is 20%, for $(139°, 112°, 0°)$ it is 27%, for $(155°, 139°, 0°)$ it is 30% and for $(155°, 155°, 0°)$ it is 29%.

2.5.3   Nucleon-knockout reactions

The category of nucleon-knockout reactions includes the removal of one to a few nucleons. For one-nucleon knockout reactions, it is possible to calculate $P(m)$. The multipolarity, l_e, of the transition from I_{ii} to I_i is deduced from the momentum distribution of the knocked-out particle as well as knowledge of I_{ii}. (In nucleon-knockout reactions I_{ii} is usually the spin of an excited state in another nucleus, not the ground state spin of the nucleus of interest as may be implied in Figs. 2.1 and 2.2.) $P(m)$ can be calculated using an extension of the eikonal model [67] to obtain m substate dependent cross sections. The model utilizes the black-disk limit: the projectile wavefunction is unchanged throughout space except for a cylinder of a given radius where it is set to zero. This is discussed in more detail in [68]. In Fig. 2.13, $W(\theta)$
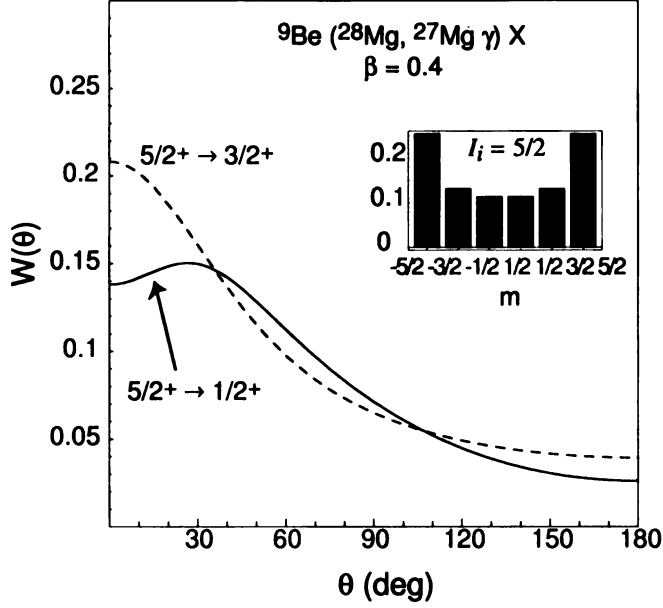
Figure 2.13: $W(\theta)$ for the one-neutron knockout reaction of $^9\mathrm{Be}(^{28}\mathrm{Mg},^{27}\mathrm{Mg}\,\gamma)\mathrm{X}$ at $\beta = 0.4$ for the $5/2^+$ to $1/2^+$ quadrupole transition and $5/2^+$ to $3/2^+$ dipole transition. The inset shows the m substate distribution for the $5/2^+$ excited state which corresponds to 27% prolate alignment.

is shown with the corresponding calculated m substate distribution [69] for the one-neutron removal reaction of $^9\mathrm{Be}(^{28}\mathrm{Mg},^{27}\mathrm{Mg}\,\gamma)\mathrm{X}$ at $\beta = 0.4$. The anisotropy of the γ-ray angular distribution can be significantly increased by selecting momenta from the center region of the momentum distribution where the greatest contribution is from the $m = \pm\ I_i$ substates. In Fig. 2.14, $W(\theta_1, \theta_2, \Phi)$ is shown for the one-neutron knockout reaction of $^9\mathrm{Be}(^{52}\mathrm{Ca},\ ^{51}\mathrm{Ca}\,\gamma)\mathrm{X}$ at $\beta = 0.4$ for the $7/2^+ \rightarrow 5/2^+ \rightarrow 3/2^+$ and $7/2^+ \rightarrow 3/2^+ \rightarrow 3/2^+$ γ-ray transitions in $^{51}\mathrm{Ca}$. The m substate distribution [69] for the $7/2^+$ excited state in $^{51}\mathrm{Ca}$ is shown in Fig. 2.15. The relative difference between the $7/2^+ \rightarrow 5/2^+ \rightarrow 3/2^+$ and $7/2^+ \rightarrow 3/2^+ \rightarrow 3/2^+$ correlation functions is shown in a three-dimensional plot in Fig. 2.16 and is as large as 40%.

The relative difference between quadrupole and dipole transitions for nucleon-knockout reactions is similar to fragmentation reactions when the entire momentum distribution is used. Thus the number of counts needed at a given angle is approximately the same as stated at the end of the previous section. If a cut is made on the

^{9}Be(^{52}Ca,^{51}Ca γ) X
Laboratory frame (β = 0.4)
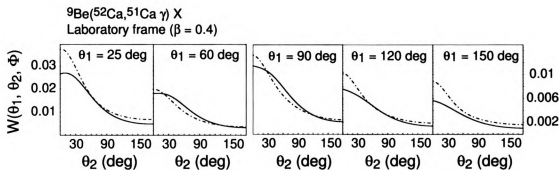
Figure 2.14: Plots of $W(\theta_1, \theta_2, \Phi)$ for the one-neutron knockout reaction of ^{9}Be(^{52}Ca, ^{51}Ca γ)X at $\beta = 0.4$ for the $7/2^+ \rightarrow 5/2^+ \rightarrow 3/2^+$ (dash-dotted curves) and $7/2^+ \rightarrow 3/2^+ \rightarrow 3/2^+$ (solid curves) γ-ray transitions in ^{51}Ca. In each plot Φ and θ_1 are fixed; $\Phi \equiv \phi_1 - \phi_2 = 0°$ and the value of θ_1 is as labeled on each plot. The angular correlation function, $W(\theta_1, \theta_2, \Phi)$, is normalized as in Eq. 2.5.
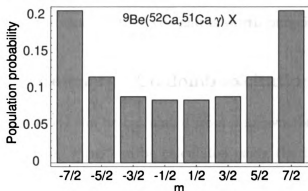
Figure 2.15: The m substate distribution of the $7/2^+$ excited state of ^{51}Ca produced from the one-neutron knockout reaction ^{9}Be(^{52}Ca, ^{51}Ca γ)X at $\beta = 0.4$. The distribution corresponds to 25% prolate alignment.
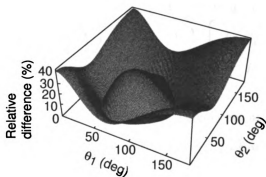
Figure 2.16: Three-dimensional plot of the relative difference between the $7/2^+ \rightarrow 5/2^+ \rightarrow 3/2^+$ and $7/2^+ \rightarrow 3/2^+ \rightarrow 3/2^+$ γ-ray transitions (with respect to the $7/2^+ \rightarrow 5/2^+ \rightarrow 3/2^+$ transition) in ^{51}Ca from the one-neutron knockout reaction of ^{9}Be(^{52}Ca, ^{51}Ca γ)X at $\beta = 0.4$.

center of the momentum distribution, the relative difference between quadrupole and dipole transitions can be increased significantly.

In this work, the beam axis is used as the quantization axis for calculations of γ-ray angular distributions and γ-γ angular correlations. It has been shown [70] for nucleon-knockout reactions that if the recoil direction of the knocked-out nucleon is used as the quantization axis instead of the beam axis, a large amount of anisotropy is produced in the angular distribution. Unlike in fragmentation reactions, in nucleon-knockout reactions the excited state $P(m)$ can be estimated from the momentum distribution of the knocked-out nucleon. Looking at the γ-ray angular distribution with the recoil direction as the quantization axis gives a much larger anisotropy than using the beam axis as the quantization axis and is worth pursuing further.

2.5.4 Intermediate-energy Coulomb excitation

In Coulomb excitation $P(m)$ can be calculated from a known Hamiltonian for given electromagnetic transitions. $P(m)$ can be calculated using the theory of Alder and Winther [71] for intermediate-energy Coulomb excitation. Its form is

$$
P(m) = \sum_{\mu=-l_e}^{l_e} G_\pi(\mu, \beta, l_e) G_\pi^*(\mu, \beta, l_e) g(\mu, \xi)
$$
$$
\times (-1)^{-m-\mu} (-1)^\lambda (2\lambda + 1)
$$
$$
\times \begin{pmatrix} I_i & I_i & \lambda \\ -m & m & 0 \end{pmatrix} \begin{pmatrix} l_e & l_e & \lambda \\ \mu & -\mu & 0 \end{pmatrix} \begin{Bmatrix} I_i & I_i & \lambda \\ l_e & l_e & I_{ii} \end{Bmatrix} \tag{2.21}
$$

where π specifies either electric or magnetic transitions and l_e is the multipolarity of the Coulomb excitation. The $G_\pi(\mu, \beta, l_e)$ and $g(\mu, \xi)$ functions are defined in [71]. The adiabacity parameter, ξ, specifies a straight-line trajectory with a correction that takes into account that the distance of closest approach is increased due to Coulomb deflection. ξ depends on the atomic number and mass of the target and projectile, the impact parameter, the velocity of the incoming projectile, and the

excitation energy of the nucleus. In the plots in Figs. 2.17 through 2.21 the impact parameter of the projectile is integrated from the minimum impact parameter, b_{min}, to infinity. This is experimentally realized by selecting events in which the angle of the scattered projectile is less than θ_{max}. θ_{max} is analytically related to the minimum impact parameter, b_{min}, for a specific reaction at a specific energy. In intermediate-energy Coulomb excitation reactions the target is viewed as a means of exciting the projectile. Thus, we consider the center-of-mass frame to be the projectile frame. This is a good approximation for light nuclei, but for heavy nuclei the center-of-mass and projectile frames should be distinguished. With typical minimum impact parameters in Coulomb excitation (touching spheres plus a few femtometers), and excitation energies of up to a few MeV, a Coulomb-excited nucleus exhibits prolate alignment. For illustrative purposes, it is worth noting that for very large minimum impact parameters (i.e. $b_{min} \approx 100$ fm), the alignment becomes oblate. For typical impact parameters in Coulomb excitation, as the velocity of the incoming beam increases, the amount of prolate alignment increases. The γ-ray angular distribution curves for ^{209}Bi(^{56}Ni,^{56}Ni γ) at 85 MeV/nucleon ($\beta = 0.4$) and 233 MeV/nucleon ($\beta = 0.6$) for quadrupole, dipole and octupole transitions with their corresponding m substate distributions are shown in Fig. 2.17.

The γ-ray angular distribution plots in Figs. 2.17 through 2.21 are calculated with E2 and E3 excitations. A dipole transition is $I_{ii} = 0 \rightarrow I_i = 3 \rightarrow I_f = 2$ (0→3→2), quadrupole is 0→2→0 and octupole is 0→3→0. For a given multipolarity, transitions between different spins, $I_i \rightarrow I_f$, are very similar at $\beta = 0.4$ for intermediate-energy Coulomb excitation reactions.

In intermediate-energy Coulomb excitation, the effect on $W(\theta)$ of varying the minimum impact parameter, b_{min}, is negligible for typical minimum impact parameters (touching spheres plus a few femtometers). As can be seen in the top row of Fig. 2.18, $W(\theta)$ is shown for ^{209}Bi(^{56}Ni,^{56}Ni γ) at 85 MeV/nucleon ($\beta = 0.4$) for three different minimum impact parameters: touching spheres plus 2 fm, touching spheres plus
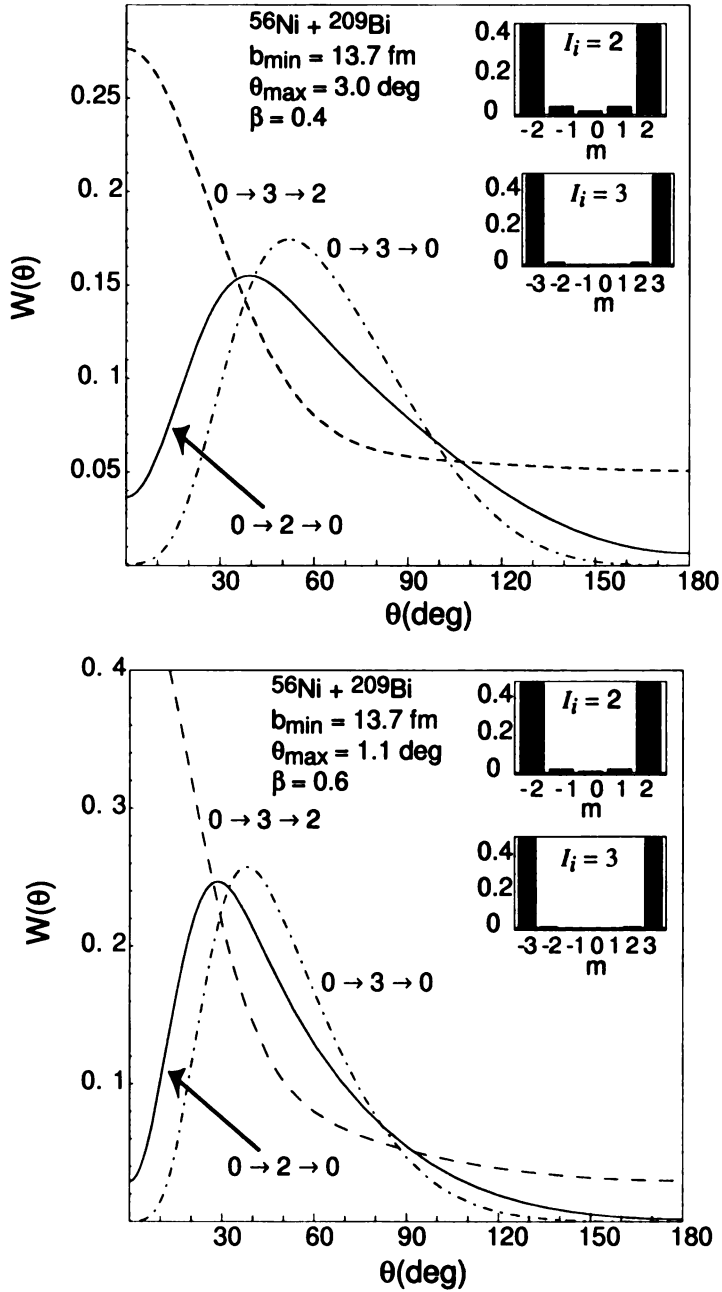
Figure 2.17: $W(\theta)$ for the Coulomb excitation reaction of ^{209}Bi(^{56}Ni,^{56}Niγ) at 85 MeV/nucleon ($\beta = 0.4$) (top plot) and 233 MeV/nucleon ($\beta = 0.6$) (bottom plot) with a minimum impact parameter, b_{min}, of touching spheres plus 2 fm and an excitation energy of 1 MeV. θ_{max} is the maximum scattering angle of the projectile in the laboratory frame corresponding to b_{min}. The insets show m substate distributions for the excited states.
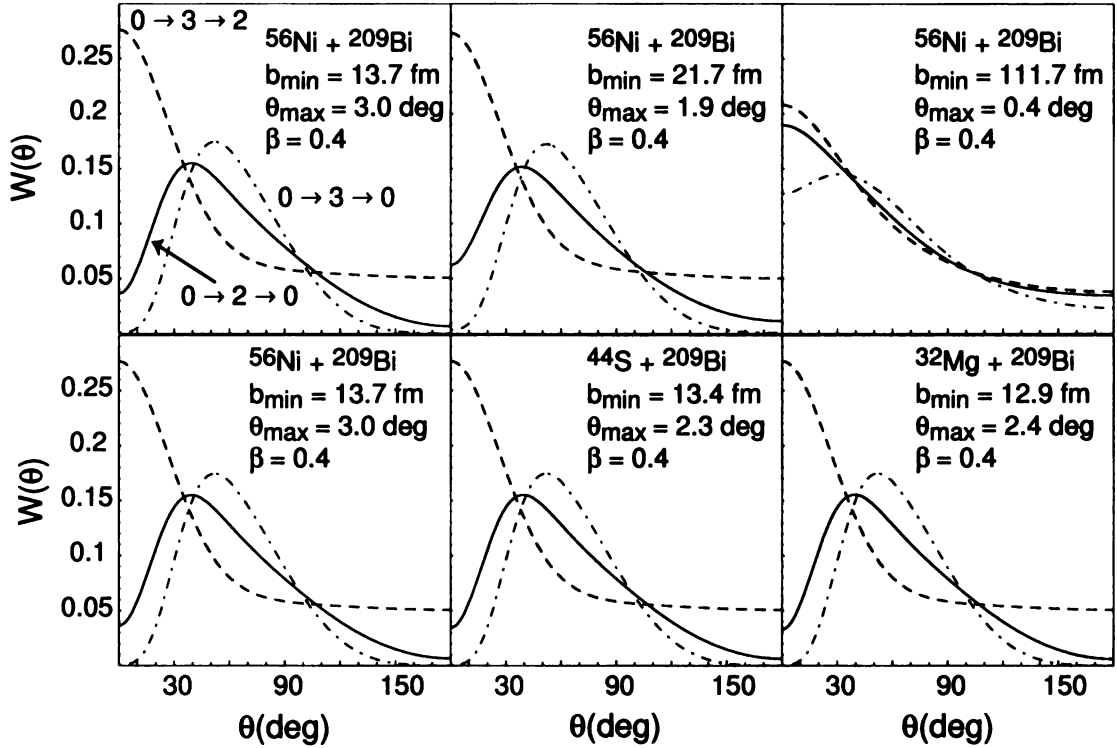
Figure 2.18: $W(\theta)$ for Coulomb excitation reactions at 85 MeV/nucleon ($\beta = 0.4$). The top row shows $W(\theta)$ for three different minimum impact parameters, b_{min}. The bottom row shows $W(\theta)$ for three different reactions. The minimum impact parameter is touching spheres plus 2 fm for all three reactions. θ_{max} is the maximum scattering angle of the projectile in the laboratory frame corresponding to b_{min}. As in previous plots, the quadrupole transitions are depicted by solid curves, dipole transitions are dashed curves and octupole transition are dash-dotted curves. The order of the transitions as labeled on the upper left plot is the same for all of the plots in the figure.

10 fm and touching spheres plus 100 fm. The difference between $W(\theta)$ for the first two cases is minimal. In an experiment, as long as the minimum impact parameter corresponds to only Coulomb excitation reactions, the effect of the size of the minimum impact parameter used is negligible on the percentage of alignment produced. For a minimum impact parameter of touching spheres plus 100 fm, $W(\theta)$ is significantly different for each of the three transitions, however, the Coulomb excitation cross section at such a large minimum impact parameter is essentially zero. In general, as the minimum impact parameter increases, the amount of prolate alignment slowly decreases until the alignment becomes oblate. The second row of Fig 2.18 shows three

41
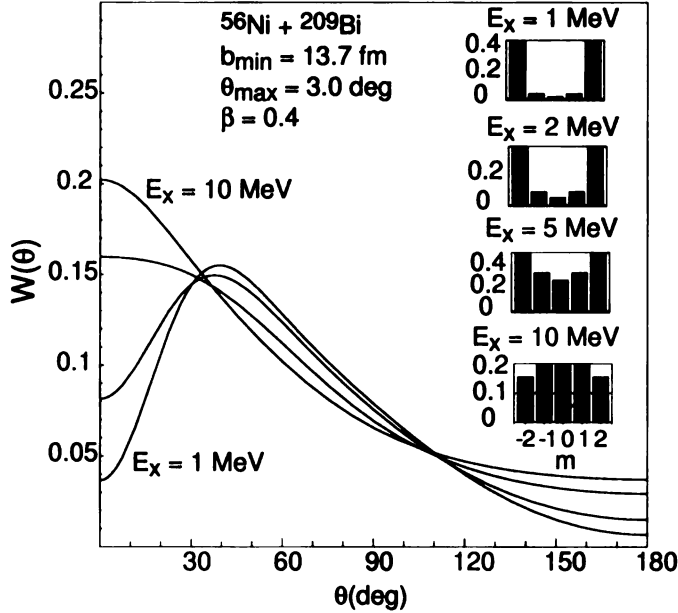
Figure 2.19: $W(\theta)$ for quadrupole Coulomb excitation reactions with 1, 2, 5 and 10 MeV excitation energies at 85 MeV/nucleon ($\beta = 0.4$). The minimum impact parameter is equal to touching spheres plus 2 fm. θ_{max} is the maximum scattering angle of the projectile in the laboratory frame corresponding to b_{min}.

plots of $W(\theta)$ for three different Coulomb excitation reactions. The minimum impact parameters are all touching spheres plus 2 fm. As can be seen, there is no detectable difference between ^{209}Bi(^{32}Mg,^{32}Mg γ), ^{209}Bi(^{44}S,^{44}S γ) and ^{209}Bi(^{56}Ni,^{56}Ni γ). For different light projectiles (from ^{14}N to ^{115}In), with a heavy (^{197}Au or ^{209}Bi) target, the effect on $P(m)$ is negligible. In Coulomb excitation not only do the velocity of the beam, impact parameter and nuclei involved affect $P(m)$, but the excitation energy also affects $P(m)$, which in turn influences $W(\theta)$. As just seen, the minimum impact parameter and nuclei involved have a small effect (within typical impact parameters for Coulomb excitation) on $W(\theta)$, but the excitation energy of the nucleus can have a fairly large effect on $W(\theta)$. In Fig. 2.19, $W(\theta)$ is shown for a quadrupole transition with 1, 2, 5 and 10 MeV excitation energy with the corresponding m substate distributions. $W(\theta)$ is plotted using $\beta = 0.4$ and a minimum impact parameter equal to touching spheres plus 2 fm. Figs. 2.20 and 2.21 are likewise, except they show dipole and octupole transitions respectively. As the excitation energy increases, the

42
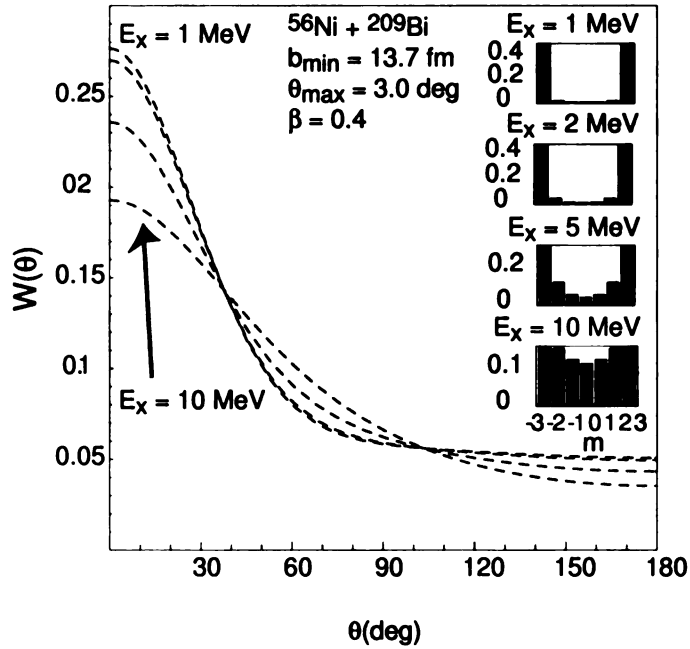
Figure 2.20: $W(\theta)$ for dipole Coulomb excitation reactions with 1, 2, 5 and 10 MeV excitation energies at 85 MeV/nucleon ($\beta = 0.4$). The minimum impact parameter is equal to touching spheres plus 2 fm. θ_{max} is the maximum scattering angle of the projectile in the laboratory frame corresponding to b_{min}.
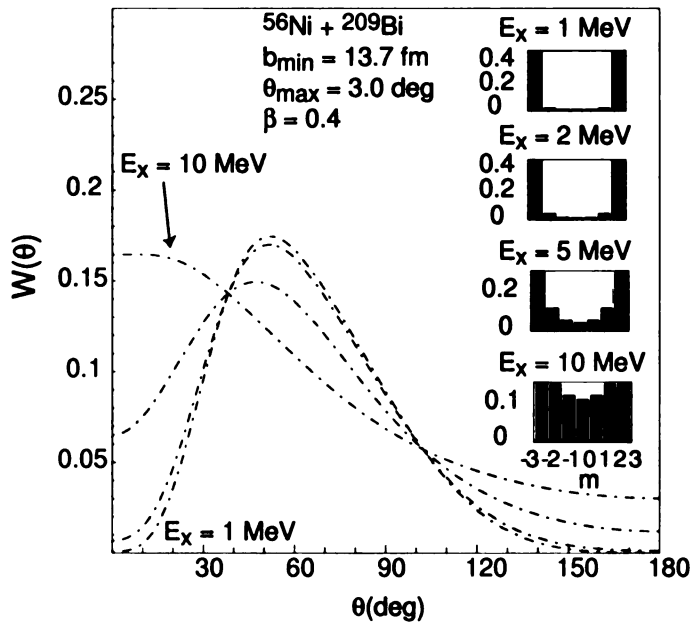
Figure 2.21: $W(\theta)$ for octupole Coulomb excitation reactions with 1, 2, 5 and 10 MeV excitation energies at 85 MeV/nucleon ($\beta = 0.4$). The minimum impact parameter is equal to touching spheres plus 2 fm. θ_{max} is the maximum scattering angle of the projectile in the laboratory frame corresponding to b_{min}.

amount of prolate alignment decreases until the alignment becomes oblate. As can be seen in Fig. 2.19, at energies between 5 and 10 MeV there exists an excitation energy where there is 0% alignment. This is significant experimentally because for certain excitation energies where there is no alignment an isotropic angular distribution will be observed, thus yielding no information about excited state spins. Different multipolarity transitions can be distinguished clearly as long as excitation energies are on the order of a few MeV. Therefore, in intermediate-energy Coulomb excitation, using γ-ray angular distributions to determine multipolarities of γ-ray transitions is feasible.

For intermediate-energy Coulomb excitation performed at $\beta = 0.4$ with an excitation energy of 1 MeV and a minimum impact parameter of touching spheres plus a few femtometers, the relative difference between a quadrupole (0→2→0) and dipole (0→3→2) transition ranges from 88% to 20% if the range of angles around 40° and 100° is avoided. Thus for intermediate-energy Coulomb excitation a minimum of 150 counts with negligible background in the γ-ray peak at a given angle would be needed to distinguish quadrupole and dipole transitions with a relative difference of 20%. If detectors are placed at very forward (less than 16°) or backward (greater than 142°) angles, the relative difference between a quadrupole and dipole transition is greater than 60%. See Chapter 4 for the angular distribution of 1460 keV γ rays from intermediate-energy Coulomb excited ^{40}Ar.

The above discussion of intermediate-energy Coulomb excitation is valid for γ-γ angular correlations as well. Fig. 2.22 shows γ-γ angular correlations for ^{209}Bi(^{56}Ni,^{56}Ni γ) at $\beta = 0.4$ in the center-of-mass and in the laboratory frames for $I_{ii} = 0 \rightarrow I_i = 4 \rightarrow I_m = 2 \rightarrow I_f = 0$ (0 → 4 → 2 → 0) and 0 → 3 → 2 → 0 correlations. The minimum impact parameter is equal to touching spheres plus 2 fm and the excitation energy is 1 MeV.

For intermediate-energy Coulomb excitation performed at $\beta = 0.4$ with an excitation energy of 1 MeV and a minimum impact parameter of touching spheres plus a few

209Bi(56Ni,56Ni γ)
Projectile frame (β = 0.0)

209Bi(56Ni,56Ni γ)
Laboratory frame (β = 0.4)
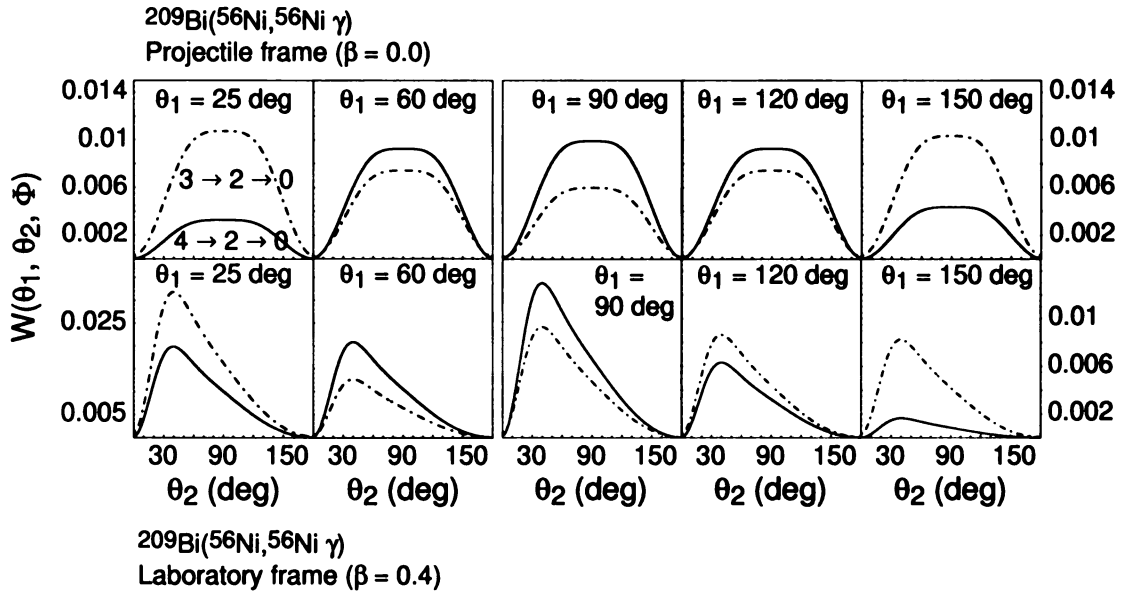
Figure 2.22: Plots of $W(\theta_1, \theta_2, \Phi)$ for the intermediate-energy Coulomb excitation reaction $^{209}\mathrm{Bi}(^{56}\mathrm{Ni},^{56}\mathrm{Ni}\ \gamma)$ with the population parameter calculated using $\beta = 0.4$. The top row shows $W(\theta_1, \theta_2, \Phi)$ in the projectile frame and the bottom row shows $W(\theta_1, \theta_2, \Phi)$ in the laboratory frame. The excitation energy of the nucleus is 1 MeV and the minimum impact parameter is touching spheres plus 2 fm (13.7 fm) which corresponds to a maximum scattering angle of the projectile of 3.0°. The initial spin, I_{ii}, of $^{56}\mathrm{Ni}$ is zero. $0 \rightarrow 4 \rightarrow 2 \rightarrow 0$ correlations are solid curves and $0 \rightarrow 3 \rightarrow 2 \rightarrow 0$ correlations are dash-dotted curves. In each plot Φ and θ_1 are fixed; $\Phi \equiv \phi_1 - \phi_2 = 0°$ and the value of θ_1 is as labeled on each plot. The angular correlation function, $W(\theta_1, \theta_2, \Phi)$, is normalized as in Eq. 2.5.

45

femtometers, as seen in Fig. 2.22, the relative difference between the $0 \to 4 \to 2 \to 0$ and $0 \to 3 \to 2 \to 0$ correlation functions is as large as 99%. Thus, with proper detector placement, distinguishing $0 \to 4 \to 2 \to 0$ and $0 \to 3 \to 2 \to 0$ correlations from one another is possible.

Chapter 3

Experimental setup

3.1 Coupled Cyclotron Facility

To study radioactive nuclei they must be produced, transported to the experimental area, and studied before they decay. The Coupled Cyclotron Facility (CCF) at the National Superconducting Cyclotron Laboratory (NSCL) utilizes projectile fragmentation to produce radioactive nuclei. The CCF consists of two superconducting cyclotrons capable of accelerating stable atomic nuclei ranging from hydrogen to uranium with energies up to 200 MeV/nucleon. At the CCF, a primary beam of a stable isotope is produced in either a room-temperature (RT) or superconducting (SC) electron-cyclotron resonance (ECR) source and then accelerated in the first superconducting cyclotron (K500). Once the K500 has fully accelerated the isotopes, they are injected into the second superconducting cyclotron (K1200) where they are stripped of additional electrons and accelerated further. The beam of stable isotopes is then bombarded onto a production target with a low atomic number (such as ^{9}Be). Many different radioactive isotopes are produced and the desired isotopes are magnetically analyzed and separated using the A1900 fragment separator. Fig. 3.1 shows a schematic of the ion sources, the two cyclotrons and the A1900 fragment separator at the CCF.
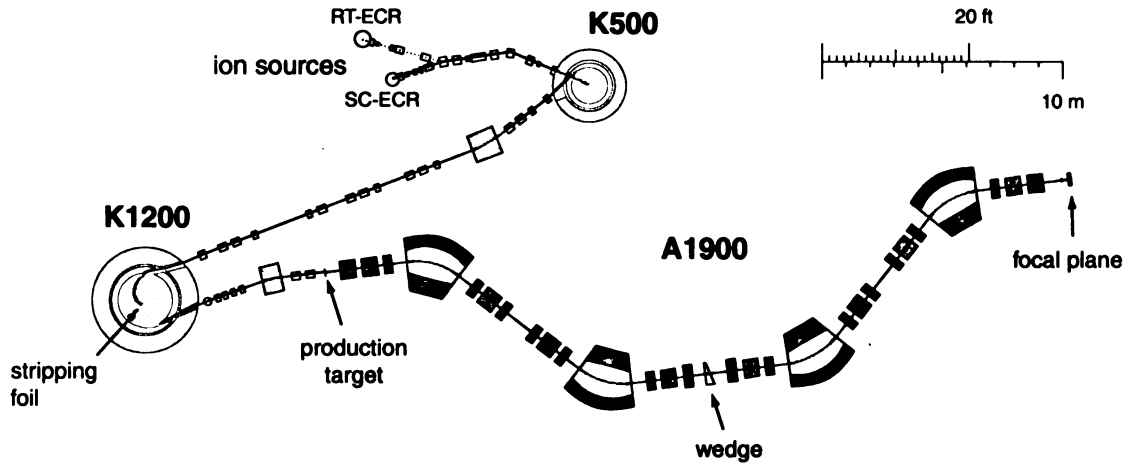
Figure 3.1: Schematic of the CCF including the ion sources, two cyclotrons and A1900 fragment separator.

3.2 A1900 fragment separator

The A1900 fragment separator [72] physically selects the isotope(s) of interest using a series of quadrupole and dipole magnets. The nuclei are selected by their mass-to-charge ratio. The A1900 contains a wedge-shaped degrader, typically made of aluminum or acrylic that can be placed in the path of the beam to purify the beam, and slits to block unwanted isotopes. Slits are located at focal points between each dipole magnet. The resulting 'secondary' beam can contain one or many different isotopes travelling at $0.3c$ to $0.5c$. The momentum spread of the secondary beam can be controlled with momentum slits and can range up to $\pm 2.5\%$. The fragments are identified and their rates are measured using a series of detectors at the focal plane of the A1900. For specific information on the the secondary beam energy, production target, wedge and slits used for the ^{40}Ar intermediate-energy Coulomb excitation experiment and the ^{9}Be(^{34}Si,^{32}Mg γ)X two-proton knockout experiment see Sections 4.2 and 5.2, respectively.

3.3 SEgmented Germanium Array

3.3.1 Configuration

The SEgmented Germanium Array (SeGA) is an array of eighteen thirty-two-fold segmented high-purity germanium detectors [73]. The high degree of segmentation is necessary to event-by-event Doppler correct the γ rays emitted by the excited nuclei travelling at $\beta = 0.3 - 0.5$. To correct for the Doppler boosting of the emitted γ rays, the first interaction point of the γ ray must be known. If the SeGA detectors were not segmented the uncertainty in that position would be the size of the entire germanium crystal, dominating the resolution of the Doppler reconstructed γ-ray peak. See the more detailed discussion of the contributions to the resolution of a Doppler reconstructed γ-ray peak in Section 3.3.5.

The detectors of SeGA were arranged in a unique configuration in the experiments presented here. The detectors were positioned such that the array was optimized for detecting γ-ray angular distributions and γ-γ angular correlations. The eighteen detectors were at the following nine (approximate) angles θ with respect to the beam axis: 24°, 29°, 40°, 60°, 78°, 90°, 126°, 139° and 147°. There were two detectors per angle. The distance from the center of each germanium crystal to the target was 24.5 cm. For all but the two detectors at 24°, the detectors were oriented with the long side of the cylindrical crystal perpendicular to the target. (The detectors at 24° were nearly perpendicular to the target, but physical constraints prevented them from being completely perpendicular.) Fig. 3.2 shows a top-view photograph of the SeGA detectors arranged in the configuration described. See also Figs. 3.4, 3.5, and 3.6 in the discussion of the detector positions in Section 3.3.3 for a front-view, side-view and top-view of the detectors generated by GEANT. For the experiments presented here, SeGA was positioned at the pivot point (target position) of the S800 spectrograph. The secondary beam impinged upon the secondary target at the center of SeGA and the fragments and scattered beam continued into the S800 spectrograph while SeGA

Beam direction towards S800
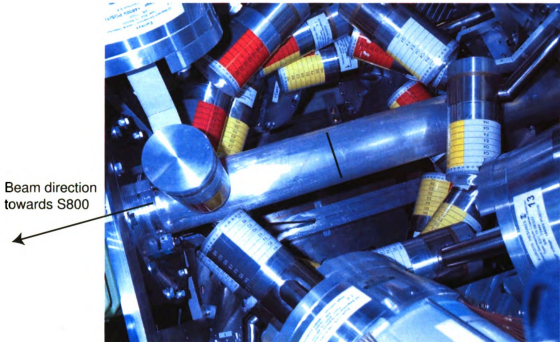
Figure 3.2: Photograph of SeGA at the target position of the S800 spectrograph. The black line drawn on the beampipe in the center of the array indicates the approximate position of the secondary target inside the beampipe.

detected the γ rays emitted from excited nuclei produced in the reactions.

3.3.2 Standard coordinate system

The standard coordinate system used in the experimental setup, the data analysis program SpecTcl, and the detector simulation program GEANT [74] is shown in Fig. 3.3. The angles, θ and ϕ in degrees are defined below.

$$\cos(\theta) = \frac{z}{\sqrt{(x)^2 + (y)^2 + (z)^2}} \tag{3.1}$$

$$\phi = \begin{cases} \arctan(y/x) & \text{if } y > 0 \text{ and } x > 0 \\ \arctan(y/x) + 180 & \text{if } y > 0 \text{ and } x < 0 \\ \arctan(y/x) & \text{if } y < 0 \text{ and } x > 0 \\ \arctan(y/x) + 180 & \text{if } y < 0 \text{ and } x < 0 \end{cases} \tag{3.2}$$
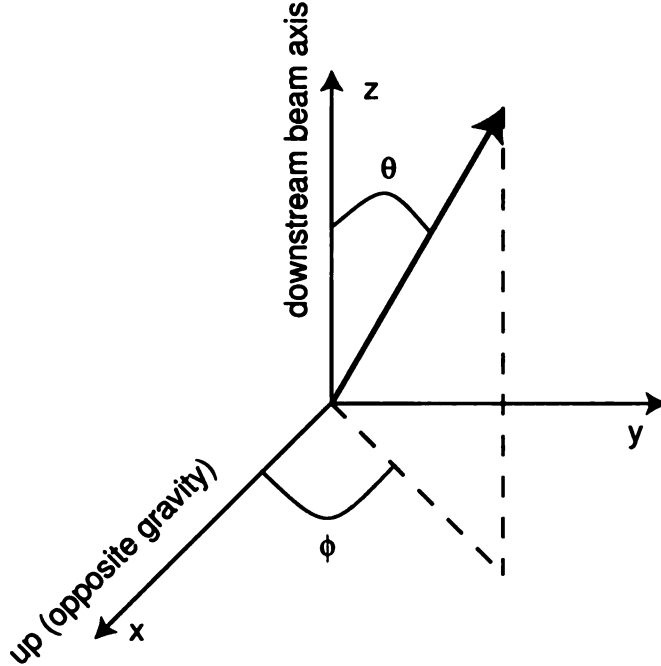
Figure 3.3: Sketch of the standard coordinate system used in the experimental setup, SpecTcl, and GEANT.

3.3.3 Detector positions

In order to Doppler correct the γ-ray energy spectra as will be discussed in Section 3.3.5, the (x,y,z) positions of the center-of-mass of the segments of each SeGA detector with respect to the target position must be known. As discussed in Section 3.3.1, the configuration of the SeGA detectors was new for the experiments presented here. The arrangement was also more complicated than previous configurations. The procedure used to generate the (x,y,z) position of the center-of-mass of each segment of each SeGA detector will be outlined below.

First, the detectors were measured with respect to the frame that held them in the arrangement described in Section 3.3.1. This was done using two theodolites. Each theodolite measured the horizontal and vertical angle of the point focused on. This gave the position of that point with respect to the coordinate system set up by the theodolites. Three to four points on the end cap of the crystal were measured as well as three places on the frame. This was done for each SeGA detector. Using

MicroStation [75], the horizontal and vertical angles from the theodolites, for each point, were transformed into (x,y,z) coordinates with the origin at the center of the array (at the target position).

The (x,y,z) positions of the three to four points on the end cap of each crystal then had to be transformed into center-of-mass coordinates for each segment of each SeGA detector. This was done using a Mathematica [76] script that, for each detector, folded the (x,y,z) positions of the points on the end cap with the known [77] crystal segment positions with respect to the detector can. The Mathematica script was modified from a previous script [78] so that it could function with three (instead of four) end cap position points as input. (When using the theodolites, because of the complicated configuration, four end cap points were not always visible, so only three points could be measured.)

The (x,y,z) positions of the center-of-mass of each segment of each SeGA detector in the current arrangement were then used in SpecTcl and GEANT. (GEANT is discussed in Section 3.3.6.) In previous detector configurations GEANT only used the (x,y,z) center-of-mass coordinate of each segment for Doppler reconstruction. The SeGA detector configuration was put in separately by hand. For the current arrangement, manually inputting to GEANT the detector configuration would have been prohibitively tedious and prone to errors. Therefore a Fortran subroutine was written that took the (x,y,z) positions of the center-of-mass of each segment of each SeGA detector as input and gave as output the detector positions in space in the format required by GEANT. The subroutine is shown in Appendix A. This subroutine can be used for any detector geometry, not just the current configuration. It requires the (x,y,z) positions of the center-of-mass of each segment of each SeGA detector. For each detector configuration this information must be known for SpecTcl, therefore to run GEANT simulations now with a new configuration there is no additional work to be done. It has been tested for the previous, simpler, configuration and the results match those where the geometry was put in manually. Figs. 3.4, 3.5, and 3.6
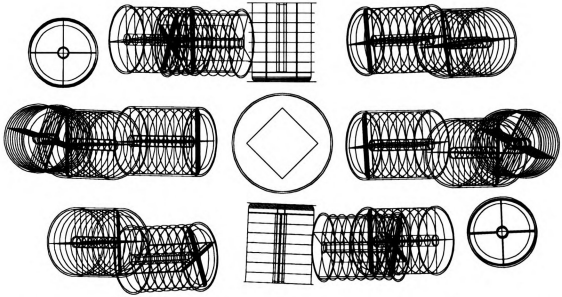
Figure 3.4: Front-view of the SeGA detector geometry. The figure was generated in GEANT.
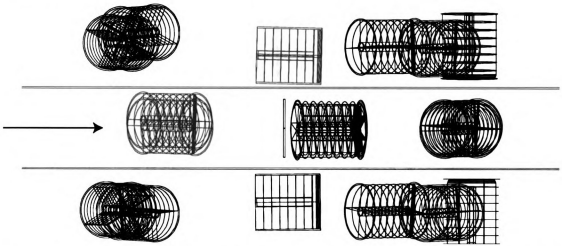
Figure 3.5: Side-view of the SeGA detector geometry. The figure was generated in GEANT. The beam direction is indicated by the arrow.

show the front-view, side-view and top-view, respectively, of the SeGA detectors in GEANT in the configuration as described in Section 3.3.1. The figures were generated in GEANT by displaying the geometry of the SeGA detectors after the subroutine described above was called.

The SeGA detector frame had to be aligned such that the target would be at the target position. SeGA was positioned such that the target position of the frame was at
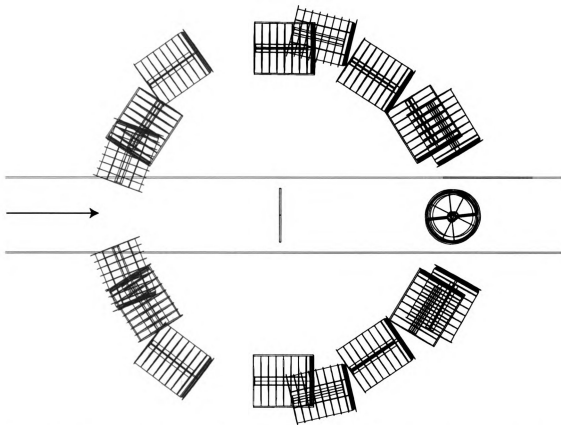
Figure 3.6: Top-view of the SeGA detector geometry. The figure was generated in GEANT. The beam direction is indicated by the arrow.

the pivot point of the S800 spectrograph. The target position is where the secondary beam was focused. To align the frame theodolites were used as well as reference points on the frame and wall (to mark the position of the pivot point). Once the frame was aligned, the target was inserted into the beampipe with a measured stick such that the target was at the target position.

3.3.4 Energy and efficiency calibrations

In order to accurately determine the energies of the γ rays observed in the de-excitation of a nucleus, the SeGA detectors must be energy-calibrated with standard γ-ray sources. In order to determine the number of γ rays emitted in the de-excitation of a nucleus the efficiency of each SeGA detector in the experimental setup must be determined.

The energy and efficiency calibrations were performed using two standard calibration sources, ^{152}Eu (NSCL ID: E2880) and ^{56}Co. They were chosen because they have many strong γ rays between 245 keV and 3272 keV. (The 122 keV γ ray in ^{152}Eu was below the low-energy thresholds of the SeGA detectors.) The sources were placed at the target position of SeGA for two hours each. The correct placement of the sources is essential for the measurement of the efficiency of the detectors because the efficiency is dependent on distance from the source and physical materials between the source and the detectors (i.e. the beampipe).

The energy and efficiency calibrations were done using PAW [79]. For the energy calibration, the γ-ray peaks were fit with a Gaussian peak plus a quadratic background for each detector. The centroids were then fit to the calibrated energies using a quadratic polynomial to get the calibration parameters. Using these calibration parameters, calibrated energy spectra were created for each detector and checked with the source data.

For the efficiency calibration the area of the γ-ray peaks must be accurately determined. The γ-ray peaks have slight low-energy tails that become larger with increasing

energy. In order to measure accurate peak areas it was necessary to parameterize the peak shapes. This was not necessary for the energy calibration because the low-energy tails did not affect the accurate determination of the peak centroids. The total fit function for the efficiency calibration is a Gaussian distribution plus a skewed Gaussian plus a quadratic background. The parameters include a Gaussian width, skew width and skew height. The skew width was fixed to be 1.25 times the Gaussian width. First the Gaussian width was parameterized, letting the skew height and Gaussian width vary. Then using the parameterized Gaussian width, the skew height was parameterized. Once the skew height was determined, the skew shape could then be fixed for each γ-ray peak in each detector. Keeping the skew parameters fixed, another fit was performed letting the Gaussian width vary in order to refine the width parameterization. Once the peak shape was completely parameterized as a function of energy for each detector, final fits were performed fixing the Gaussian width, skew width and skew height, only letting the peak height, peak centroid and three quadratic background parameters vary.

Once all the γ-ray peaks from both the ^{152}Eu and ^{56}Co sources were fit in each detector, separate efficiency curves for both sources were fit with the following function,

$$Eff_{E_\gamma} = \frac{P_1}{(E_\gamma - P_2 + e^{-0.269*E_\gamma})^{P_3}} \qquad (3.3)$$

where E_γ is the energy of the γ ray and P_1, P_2 and P_3 are the fit parameters. This function is only able to accurately fit the experimental source efficiency above approximately 150 keV. The ^{152}Eu source was a calibrated source, but the ^{56}Co source was not a calibrated source. To combine the two efficiency curves, the ^{56}Co source efficiency curve was scaled to the ^{152}Eu source efficiency curve by minimizing the square of the difference between the two curves. The combined efficiency source data was then fit to get the final efficiency calibration parameters. For the analysis presented here, the efficiency calibration was done for each SeGA angle pair. Fig. 3.7
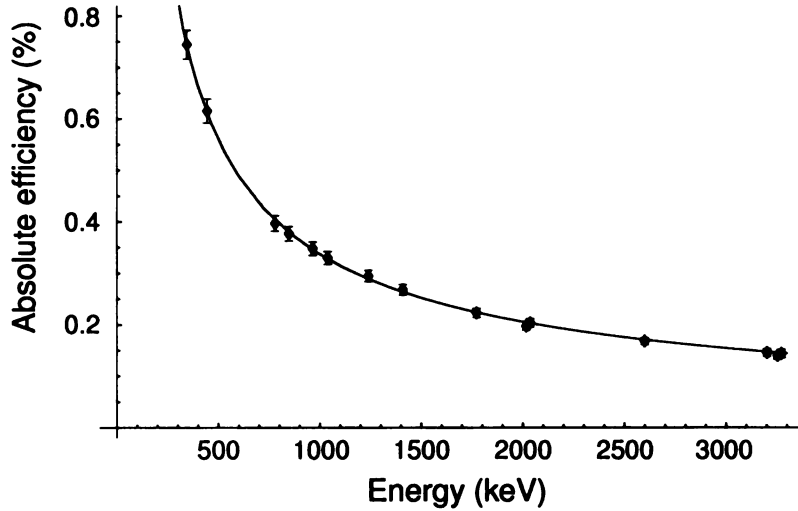
Figure 3.7: Plot of the absolute efficiency in percent versus γ-ray energy in keV for the 60° SeGA angle pair. The values of the parameters in Eq. 3.3 for the 60° angle pair are $P_1 = 39.9$, $P_2 = 36.0$ and $P_3 = 0.69$.

shows an efficiency curve and fit parameters for the 60° SeGA angle pair. The efficiency curve shown is representative of all angle pairs in SeGA in the configuration described in Section 3.3.1. The total photo-peak efficiency for the entire SeGA at 1 MeV is $(3.01 \pm 0.04)\%$.

3.3.5 Doppler reconstruction

For the experiment presented here, the secondary beam energies were approximately 0.4c. When an excited nucleus emits a γ ray traveling at relativistic speeds, the energy of the γ ray as seen by the SeGA detectors is Doppler boosted. The γ-ray energy spectra must be Doppler corrected to reconstruct the energy of the emitted γ ray. The following equation is used,

$$E_\gamma^{pro} = \frac{E_\gamma^{lab}(1 - \beta \cos(\theta_{lab}))}{\sqrt{1 - \beta^2}} \tag{3.4}$$

where E_γ^{pro} is the energy of the γ ray in the projectile frame, E_γ^{lab} is the energy of the γ ray in the laboratory frame, β is the velocity of the projectile frame with respect to the laboratory frame relative to the speed of light at the point of γ-ray emission,

and θ_{lab} is the laboratory angle of the emitted γ ray with respect to the beam axis.

In order to perform the Doppler correction, E_γ^{lab}, β and θ_{lab} must be known. Uncertainties in the β and θ_{lab} parameters produce a resolution in the Doppler corrected γ-ray peaks that is larger than is seen for γ-ray source peaks. The square of the energy resolution, $\frac{\Delta E_\gamma}{E_\gamma}$, is given by,

$$
\left(\frac{\Delta E_\gamma}{E_\gamma}\right)^2 = \left(\frac{\beta \sin(\theta_{lab})}{1 - \beta \cos(\theta_{lab})}\right)^2 (\Delta\theta_{lab})^2
$$
$$
+ \left(\frac{-\beta + \cos(\theta_{lab})}{(1 - \beta^2)(1 - \beta \cos(\theta_{lab}))}\right)^2 (\Delta\beta)^2 + \frac{(\Delta E_\gamma^{intr})^2}{(E_\gamma)^2}. \tag{3.5}
$$

The uncertainty of the beam velocity, $\Delta\beta$, is primarily due to the beam slowing down in the secondary target and the inability to determine the exact velocity at the point of γ-ray emission. The uncertainty in the angle of the emitted γ ray, $\Delta\theta_{lab}$, is dominated by the finite size of the segments of the SeGA detectors. With the detectors in the configuration discussed in Section 3.3.1, if the point of γ ray emission was known exactly and was within approximately 5 mm of the center of the target, then $\Delta\theta_{lab}$ would be approximately 2.34°. However, the position of the γ-ray emission is not known exactly. The z position is most dependent on the half-life of the excited state. If the half-life is less than approximately 50 ps, the additional contribution from the uncertainty in the z position of the γ-ray emission to $\Delta\theta_{lab}$ is small. Fig. 3.8 shows a plot of energy resolution versus half-life, to illustrate the contributions from $\Delta\beta$ and $\Delta\theta_{lab}$ to the energy resolution. The half-life affects $\Delta\beta$ and $\Delta\theta_{lab}$ because it affects where the de-excitation occurs. If the de-excitation occurs as soon as the nucleus is excited that will give a different energy loss than if the de-excitation occurs 20 ps after the nucleus is excited. Fig. 3.9 illustrates the affect of the half-life on the z position of γ-ray emission for a given target thickness.

The intrinsic resolution, $\Delta E_\gamma^{intr}/E_\gamma$, contributes the least to the resolution of the Doppler corrected γ-ray peaks. The intrinsic resolution for an individual SeGA detector is approximately 0.30% (FWHM) at 1408 keV.
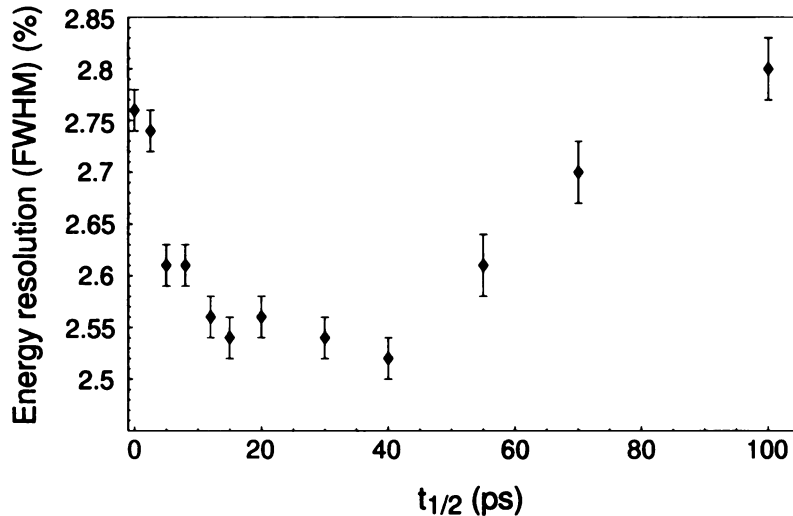
Figure 3.8: Energy resolution of a GEANT simulated 1436 keV γ ray versus half-life $t_{1/2}$ in picoseconds (ps). Each point was generated by a GEANT simulation by setting the half-life and velocity associated with that half-life as used for the Doppler reconstruction. All other GEANT input parameters stayed the same between simulations. The resolution is the energy resolution of the 1436 keV peak in the summed spectrum of all the detectors in SeGA. From 0 ps to approximately 15 ps the energy resolution drops sharply. This is because the energy loss in the target (376 mg/cm^2 ^{9}Be) is greatest at 0 ps and thus the contribution from $\Delta\beta$ is very large. Once the decays happen primarily outside the target (for half-lives greater than approximately 20 ps) the contribution from $\Delta\beta$ is much smaller and stays mostly constant because there is negligible energy loss after the target. Once the half-life is long enough that $\Delta\theta_{lab}$ increases, around approximately 50 ps, the energy resolution starts to increase.
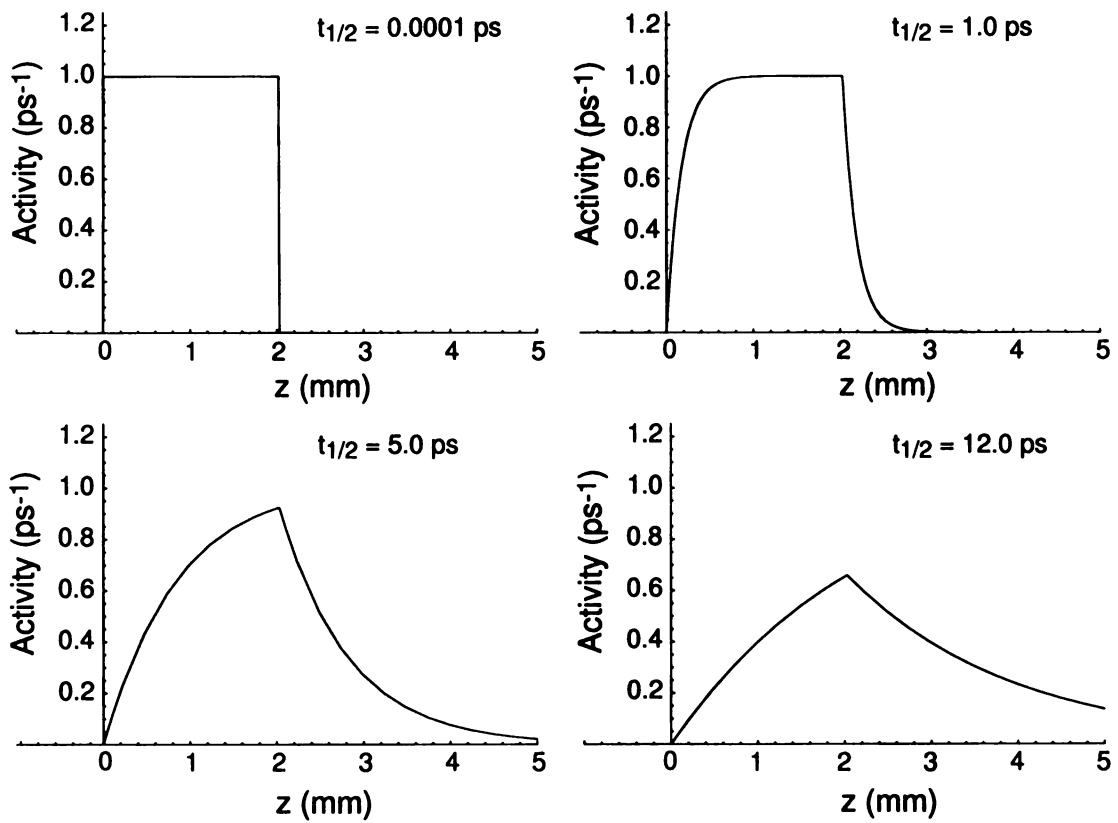
Figure 3.9: Plots of γ-ray activity versus distance for a target thickness of 2 mm. The calculations assume a constant probability for excitation over the thickness of the target, a linear decrease in velocity over thickness of the target and no absorption in the target.

The Doppler correction is performed event-by-event. As stated above, to perform the Doppler correction, E_γ^{lab}, β and θ_{lab} must be known. For each event the segment of the SeGA detector that was hit first by the de-excitation γ ray is selected and the position coordinates of that segment are used in conjunction with a x_o y_o and z_o to get the angle θ_{lab} in Eq. 3.4 using

$$\cos(\theta_{lab}) = \frac{z - z_o}{\sqrt{(x - x_o)^2 + (y - y_o)^2 + (z - z_o)^2}} \qquad (3.6)$$

where (x, y, z) is the coordinate of the first hit segment and (x_o, y_o, z_o) is the coordinate of the emission of the γ ray. Typically, x_o, y_o and z_o are each less than 1 cm. Since (x_o, y_o, z_o) cannot currently be determined event-by-event, the (x_o, y_o, z_o) used is the average (x_o, y_o, z_o) determined from the Doppler correction as described below. Currently the segment that is considered to be hit first by the γ ray is taken to be the segment in which the greatest amount of energy is deposited.

For each nucleus discussed here the energy, E_γ^{pro}, of the largest peak in the γ-ray energy spectrum was known. Therefore, the data was scanned with a mid-target β and $x_o = y_o = z_o = 0$. In the case of the ^{32}Mg γ-ray spectrum, the 885 keV γ-ray peak from the $2^+ \rightarrow 0^+_{g.s.}$ transition was fit with a Gaussian peak in each detector. For ^{40}Ar, the 1460.8 keV $2^+ \rightarrow 0^+_{g.s.}$ γ-ray transition was used. Using Mathematica, the difference between the known peak energy and the Doppler corrected centroids were minimized letting β, x_o, y_o and z_o vary. The data was re-scanned with the new β, x_o, y_o and z_o values and the procedure was repeated until the difference between the known peak energy and the Doppler corrected centroids were within the uncertainty in the energy calibration. For ^{32}Mg, this deviation was ± 4 keV for 16 of the 18 detectors. The other two detectors were ± 6 keV. For ^{40}Ar, this deviation was ± 8 keV for 12 of the 17 detectors. The deviations for other five detectors were -12 keV for three detectors and $+17$ keV for two detectors. (One of the detectors could not be used as discussed in Section 4.3.) The ^{40}Ar Doppler corrected γ-ray spectrum with these

deviations was sufficient since there was only one γ-ray peak in the ^{40}Ar spectrum.

3.3.6 GEANT simulations

The Doppler correction, described in Section 3.3.5, corrects the γ-ray energy spectrum observed in the laboratory frame to the projectile frame such that the photopeak energy centroids are the emitted γ-ray energies. But, the correction from the laboratory frame to the projectile frame does not result in a spectrum that would be observed from a source at rest. Compton scattering, pair production and scattering and interactions with the surrounding equipment all produce features that are spread out in the Doppler corrected spectrum. Also, the efficiency of the SeGA detectors are energy dependent as seen in Section 3.3.4. In order to accurately fit the Doppler-corrected energy spectra, especially if there are multiple γ-ray peaks with similar intensity close (less than approximately 500 keV apart) in energy, a simulation of the responses of the detectors is necessary. GEANT [74] performs a Monte Carlo simulation which event-by-event emits and then subsequently 'detects' a given number of γ rays. Input includes, but is not limited to, the following parameters: γ-ray energy, incoming beam velocity, target thickness, target material, outgoing beam velocity, velocity spread in the incoming beam, and SeGA detector geometry. A sample *xml* input file used by GEANT is shown in Appendix B. For the GEANT simulations used in the fitting of the ^{32}Mg and ^{40}Ar spectra, ten billion events were emitted at each γ-ray energy, with the input parameters taken from experimental observables. To verify that GEANT accurately reproduced the SeGA detector responses, the simulated peak shape for the 885 keV and 1460 keV peaks were compared to the data for the ^{32}Mg and ^{40}Ar datasets, respectively.
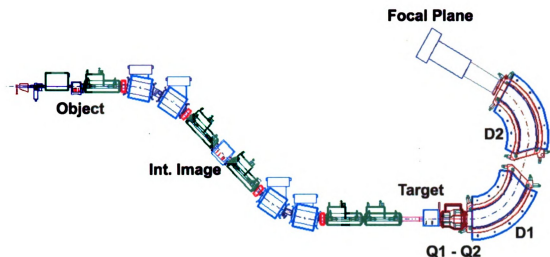
Figure 3.10: Schematic of the S800 spectrograph.

3.4   S800 Spectrograph

The S800 Spectrograph [80–83] is a high-resolution spectrometer containing six de-
tectors at its focal plane capable of giving the energy loss, energy, x and y position,
scattering angle and time-of-flight of the detected nuclei. Those detectors include
two cathode readout drift chambers (CRDCs) three plastic scintillators and an ion
chamber [81]. See Fig. 3.10 for a schematic of the spectrograph. At the object posi-
tion is a plastic scintillator used for timing. Due to physical constraints in the setup
described in Section 3.3.1, the S800 was operated in focused mode rather than dis-
persion matched mode. In focused mode the secondary beam is focused at the target
position, in the center of SeGA, and dispersed in the S800 focal plane. In dispersion
matched mode the secondary beam is dispersed at the target position and focused in
the S800 focal plane.

3.5 Trigger

The choice of what data to record during an experiment is crucial to it's feasibility and success. If uninteresting or not useful information is being recorded in place of physically interesting and necessary information then the experiment will be inefficient and the goal of the experiment may not be obtained. This includes what information of the available information is read for each event and what events are read. Selecting what events to read is possible with a trigger; events are only selected if certain conditions are true. In the setup described in Section 3.3.1 with SeGA at the target position of the S800 spectrograph, each of the following could be a trigger during an in-beam experiment: downscaled S800 particle singles, particle-γ coincidences or downscaled γ singles. Each will be described below.

For all the trigger settings, the data will only be recorded if the data acquisition is not busy. The data acquisition is busy for a finite amount of time while an event is being processed. The time the data acquisition is busy varies according to the time it takes to read out the event for a particular trigger. The rate of what is being recorded (particles or γ rays for example) also affects whether the data acquisition is busy when the next event to be recorded occurs. If the particle rate in the S800 spectrograph is very low (the length of time between events is longer than the recording time), the data acquisition is unlikely to be busy by the time the next event comes.

The S800 particle singles trigger means that data is recorded whenever a particle is detected in the plastic scintillator in the S800 focal plane. In this trigger setting, the γ ray(s) that were detected in SeGA in coincidence with that particle are also recorded. The readout of a S800 particle singles event takes approximately 800 μs. The particle-γ coincidence trigger means that data is recorded whenever a particle *and* a γ ray are detected in coincidence. The readout of a particle-γ coincidence event takes approximately 800 μs. The γ singles trigger means that data is recorded whenever a γ ray is detected in SeGA. The readout of a γ singles event takes approximately

200 μs. The three triggers can be used in combinations; the *or* of any two, or even all three of the triggers can be used as the final trigger for the data acquisition.

The particle-singles and γ-singles trigger each have a downscale value associated with them which can be set from one to 999. A downscale value of x means instead of taking every particle singles (or γ singles) event, take only every x^{th} event. This is useful when combinations of triggers are used and the rate of one trigger is dominating the others or when only one trigger is used but the rate (i.e. of particles) is too large for the data acquisition. Usually if just one trigger is used and the rate is too large for the data acquisition, the beam rate is actually lowered instead of downscaling the trigger. The fraction of time the data acquisition is unable to take data, the deadtime, must be quantified in order to correct the number of observed γ rays and particles to the number that would have been seen if every final event trigger could have been taken. This is necessary in making cross section measurements or any measurement where absolute numbers are desired. The downscale value for a trigger increases the livetime through a reduction in rate, but also introduces a correlation in the data such that the number of events occurring in close succession are reduced. With the *or* of multiple downscaled triggers comprising the final trigger, the understanding of the concept of livetime becomes complicated.

The probability distribution of the duration between two downscaled random (Poisson distributed) events is given by a gamma distribution. For a downscale value of one, the distribution reduces to an exponential distribution with maximum probability at time zero. As the downscale value is increased the peak of the probability distribution moves farther from time zero. This is shown in Chapter 3, Section VII of [84].

Therefore, the act of downscaling one or more triggers comprising the final trigger creates different livetimes for different triggers. The livetime of a downscaled trigger can actually be greater than the busy time of the data acquisition because the downscaler effectively separates the minimum time between two events. This re-

duces the number of events that can fall within the readout time. This applies to the ^{9}Be(^{34}Si,^{32}Mg γ)X experiment where the *or* of three triggers were used. Two of the triggers had downscale values greater than one. See further discussion applicable to that experiment in Section 5.2.1.

Chapter 4

Intermediate-energy Coulomb excitation of ^{40}Ar

4.1 Intermediate-energy Coulomb excitation

Intermediate-energy Coulomb excitation has become an established tool for measuring properties of exotic nuclei [85]. In intermediate-energy Coulomb excitation the target and projectile are excited in the Coulomb field of the other. The γ rays emitted from the excited target and projectile nuclei can be distinguished because the target γ rays are emitted at rest, while the projectile γ rays are emitted at the speed of the projectile. The formalism for γ-ray angular distributions of intermediate-energy Coulomb excitation reactions is presented in Section 2.5.4. Using γ-ray angular distributions to identify and confirm transition multipolarities is common for experiments where the beam energy is lower than the Coulomb barrier. However, this technique has not been explored with intermediate-energy Coulomb excitation reactions. Here the γ-ray angular distribution of the decay of the first excited state of intermediate-energy Coulomb excited ^{40}Ar is presented.

4.2 Experiment setup

For the intermediate-energy Coulomb excitation reaction measurement of ^{40}Ar, the primary beam was ^{40}Ar and a ^{9}Be production target with a thickness of 1151 mg/cm^2 was used to degrade the primary beam from 140 MeV/nucleon to the desired beam energy. SeGA was positioned at the target position of the S800 spectrograph as discussed in Section 3.3.1. At the center of SeGA, the 83.6 MeV/nucleon ^{40}Ar beam impinged upon a 350.8 mg/cm^2 ^{197}Au target. The trigger was set to: downscaled particle singles *or* particle-γ coincidences *or* downscaled γ singles.

4.3 Analysis of the γ-ray spectrum

The particle identification of the ^{40}Ar fragments in the S800 focal plane was unambiguous because the secondary beam was a pure ^{40}Ar beam and the magnetic field of the S800 spectrograph was set to the ^{40}Ar fragments. Other isotopes that may have been produced in the gold target by nucleon knockout and fragmentation reactions could make it to the S800 focal plane but the cross sections of those reactions on a gold target are very small compared to the scattering of ^{40}Ar.

To ensure that the ^{40}Ar γ rays came from Coulomb excitations and not nuclear excitations, the ^{40}Ar fragments with scattering angles corresponding to a minimum impact parameter of touching spheres plus 2 fm were selected. Therefore, the maximum scattering angle was $\theta_{max} = 2.97° = 51.8$ mrad. Shown in Fig. 4.1 is the ^{40}Ar scattering angle distribution. A gate from $0 - 51.8$ mrad in the scattering angle spectrum in Fig. 4.1 was applied to the ^{40}Ar γ-ray spectra. The scattering angle gate only reduced the number of ^{40}Ar particles by 1.3%, but reduced the number of 1461 keV γ rays by 20-35%.

As discussed in Section 3.3.5 the Doppler correction was performed using the known 1460.8 keV $2^+ \rightarrow 0_{g.s}^+$ γ ray. One of the 126° detectors could not be used in this analysis because its gain was shifting within runs. Therefore the 126° spectrum
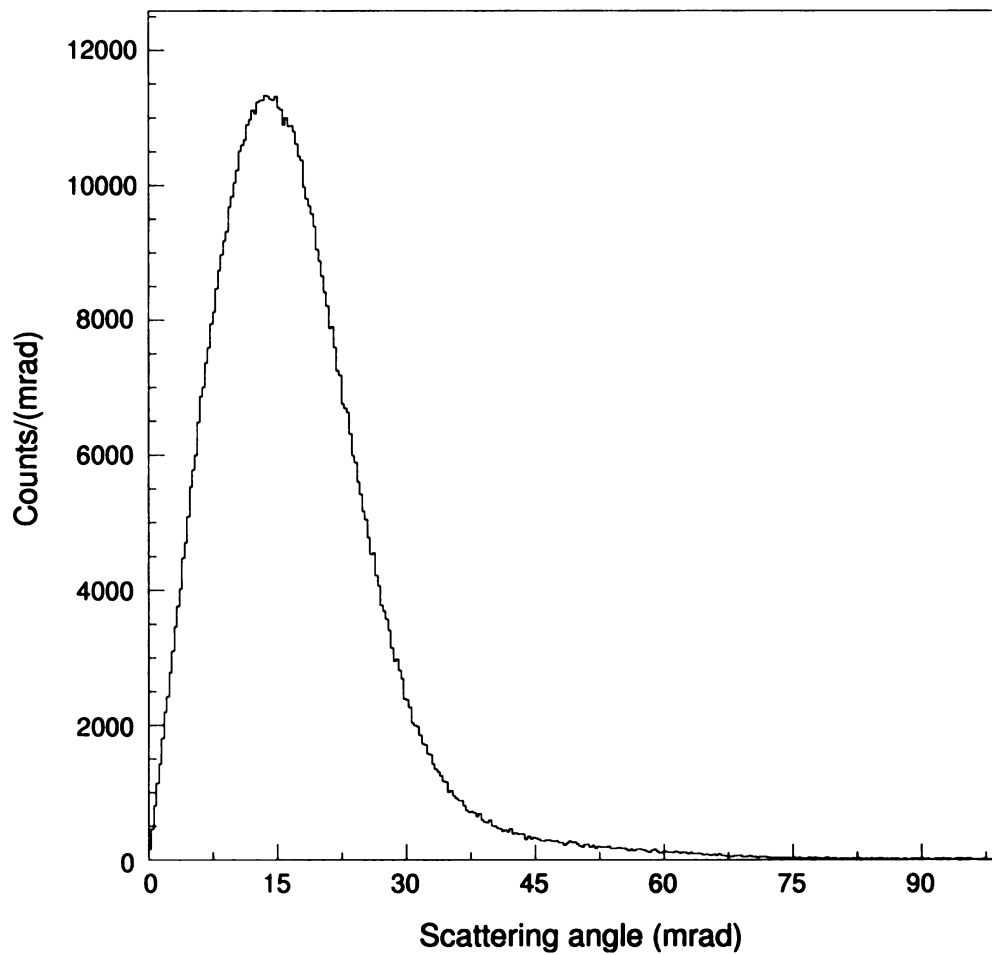
Figure 4.1: Number of scattered ^{40}Ar nuclei versus scattering angle (mrad). The spectrum includes both ^{40}Ar nuclei in coincidence and not in coincidence with a γ ray.

only contained one SeGA detector. The ^{40}Ar γ-ray spectrum for each SeGA angle pair was fit from 800-2000 keV with one GEANT simulated response function and an exponential background. Fig. 4.2 shows the 60° SeGA angle pair γ-ray spectrum. After each SeGA angle pair was fit as described, two corrections had to be made to the fit results to obtain the experimental γ-ray angular distribution. The corrections were the GEANT scale factor and the correction for the effect where the detectors became paralyzed after certain events. Both corrections are described in Section 5.3.4.

4.4 γ-ray angular distribution

In Fig. 4.3 is the γ-ray angular distribution of the intermediate-energy Coulomb excited ^{40}Ar 1460.8 keV $2^+ \rightarrow 0^+_{g.s.}$ γ ray. The experimental points are fitted with a $I_{ii} = 0 \rightarrow I_i = 2 \rightarrow I_f = 0$ ($0 \rightarrow 2 \rightarrow 0$) γ-ray angular distribution (black curve) calculated as outlined in Section 2.5.4. The only parameter that was allowed to vary in the fit was an overall scaling factor. This was due, in part, because the two additional corrections described in Section 5.3.4, coincidence trigger livetime and data loss, were not included because they are not dependent on the SeGA detector angle. The value of the scale factor is 0.0163 ± 0.0015. Fitting the experimental γ-ray angular distribution with a $0 \rightarrow 3 \rightarrow 2$ spin transition or a $0 \rightarrow 3 \rightarrow 0$ spin transition resulted in much larger χ^2_{min} values of 29.3 and 20.2, respectively compared to the $0 \rightarrow 2 \rightarrow 0$ spin transition fit where $\chi^2_{min} = 6.7$. The shape of the $0 \rightarrow 3 \rightarrow 2$ and $0 \rightarrow 3 \rightarrow 0$ calculated γ-ray angular distributions are different than the observed γ-ray angular distribution. This can be clearly seen in Fig. 4.3. Therefore, γ-ray angular distributions can be used as a method for determining the multipolarity of observed γ rays for intermediate-energy Coulomb excitation reactions.
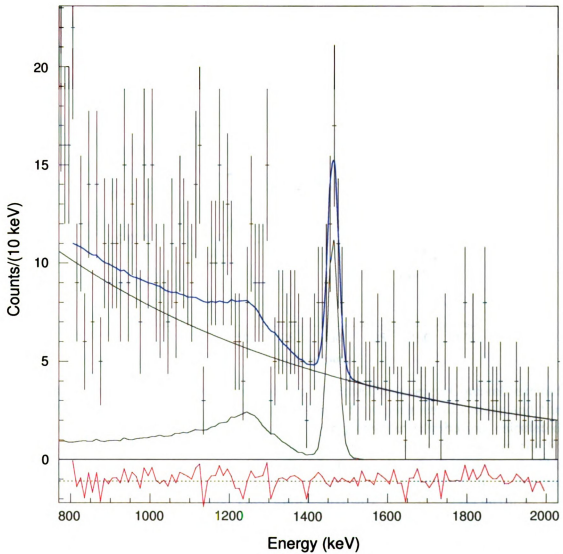
Figure 4.2: ^{40}Ar γ-ray spectrum of the pair of SeGA detectors at 60° fit with a GEANT response function. The spectrum was fit from 800-2000 keV. The spectrum was fit with one GEANT response function and an exponential background. The fit (blue), response function (black) and exponential background (black) are shown on the spectrum. The residual (red) between the fit and the data points is shown below the spectrum.
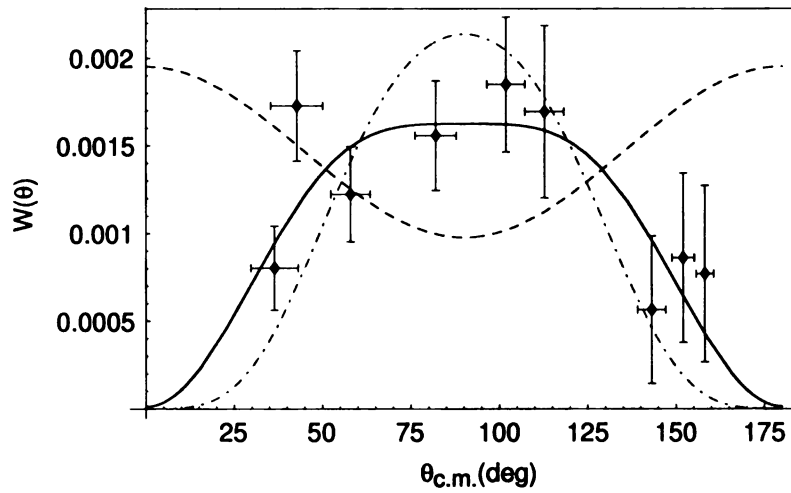
Figure 4.3: γ-ray angular distribution of the intermediate-energy Coulomb excited ^{40}Ar 1460.8 keV $2^+ \rightarrow 0^+_{g.s}$ γ ray. The points are the experimental results and the solid (black) curve is the $0 \rightarrow 2 \rightarrow 0$ calculated γ-ray angular distribution, calculated as outlined in Section 2.5.4. The only parameter that is allowed to vary in the fit of the curve to the data is an overall scaling factor as described in the text. The dash-dotted (red) and dashed (blue) curves are $0 \rightarrow 3 \rightarrow 0$ and $0 \rightarrow 3 \rightarrow 2$ γ-ray angular distributions, respectively. They were scaled with the same scale factor as the $0 \rightarrow 2 \rightarrow 0$ curve.

Chapter 5

Study of ^{32}Mg via two-proton knockout

5.1 Two-proton knockout

One-nucleon knockout reactions have been established as direct reactions and have been used to study the single-particle degree of freedom in exotic nuclei [68]. A recent two-proton knockout experiment [44] gives evidence that two-proton knockout reactions of neutron-rich nuclei also proceed as direct reactions. Calculating two-nucleon knockout cross sections is more complicated than calculating one-nucleon knockout cross sections and is addressed in [86]. In one-nucleon knockout the reaction and structure contributions can be separated, thus simplifying the calculation of the partial cross section to a given state. This is not possible in two-nucleon knockout because the reaction and structure terms are coupled. ^{32}Mg was studied using the two-proton knockout reaction ^{9}Be(^{34}Si,^{32}Mg γ)X. A schematic of the two-proton knockout from ^{34}Si to ^{32}Mg is shown in Fig. 5.1. The sequential two-step process where one proton is knocked out of ^{34}Si to create ^{33}Al and another proton is evaporated to form ^{32}Mg is excluded. Removing one proton from ^{34}Si leaves ^{33}Al in a state with enough energy to emit a neutron, but not enough energy to emit a proton. Therefore, the two-proton
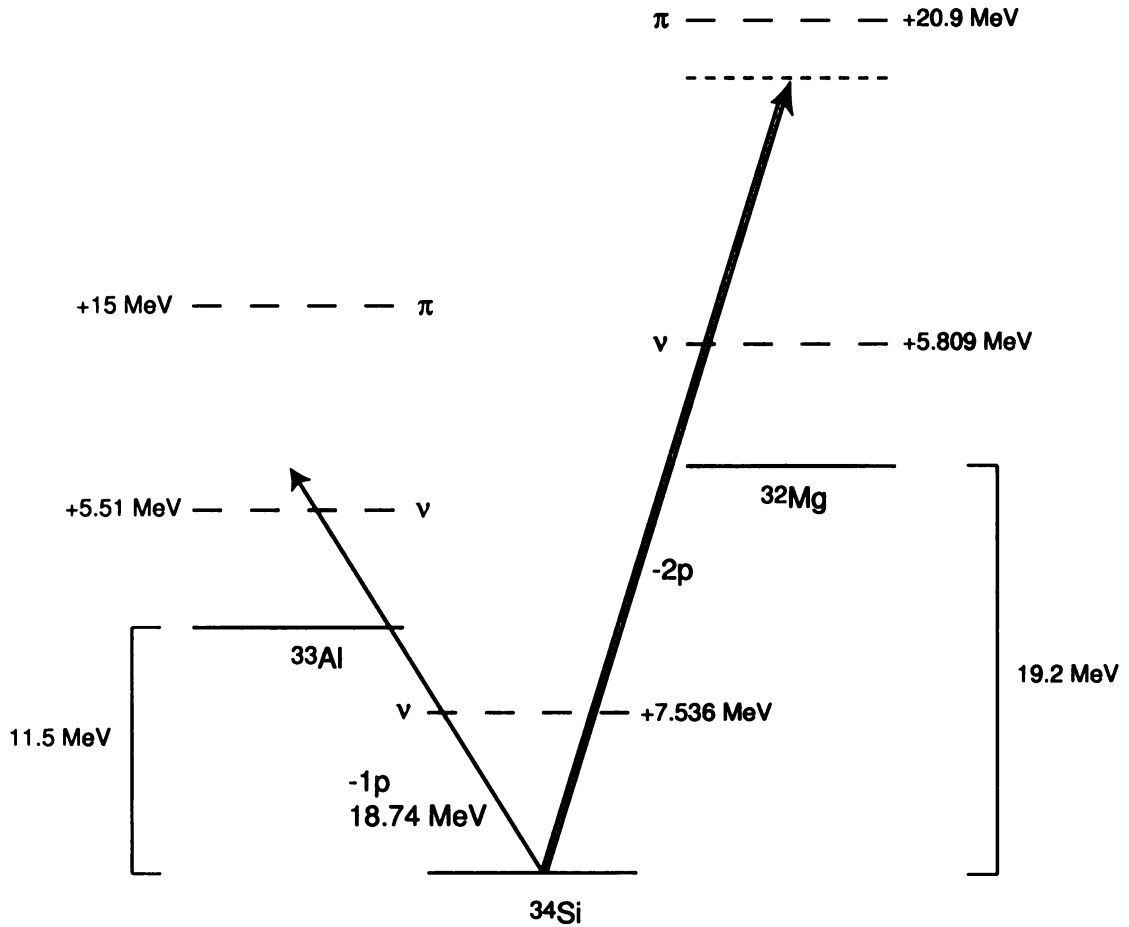
Figure 5.1: ^{34}Si $\rightarrow$ ^{32}Mg two-proton knockout schematic. The reaction, ^{9}Be(^{34}Si,^{32}Mg γ)X proceeds as a direct reaction.

knockout from ^{34}Si to ^{32}Mg proceeds as a direct reaction.

5.2 Experiment setup

The two-proton knockout reaction ^{9}Be(^{34}Si,^{32}Mg γ)X was used to study ^{32}Mg. The 140 MeV/nucleon ^{40}Ar primary beam impinged upon a 705 mg/cm^2 ^{9}Be production target. In the A1900 fragment separator, the secondary beam of ^{34}Si was physically selected, with the aid of a 750 mg/cm^2 acrylic wedge. SeGA was positioned at the target position of the S800 spectrograph as discussed in Section 3.3.1. At the center of SeGA, the 81.05 MeV/nucleon ^{34}Si beam hit a 376 mg/cm^2 ^{9}Be target. The S800

spectrograph was operated in focused mode and the ^{32}Mg fragments were centered in the focal plane.

5.2.1 Trigger

General information about the trigger for the the configuration with SeGA at the target position of the S800 spectrograph is discussed in Section 3.5. For the ^{9}Be(^{34}Si,^{32}Mg γ)X experiment, the trigger was set to: downscaled particle singles *or* particle-γ coincidences *or* downscaled γ singles. The particle-γ coincidence trigger was used because the goal of the experiment was to measure the γ rays emitted from the excited states in ^{32}Mg. Every γ ray that was in coincidence with a particle made a trigger and was read out if the data acquisition was not busy. The downscaled particle singles trigger was used to obtain a subset of the complete particle data without bias toward particles in coincidence with γ rays and without contributing significantly to the data acquisition deadtime. The particle downscale value was set to 10 throughout the experiment. The particle singles data is also used for particle identification, and analyzing momentum distributions and scattering angle distributions of scattered particles. The γ singles trigger was used in order to record γ rays not necessarily in coincidence with a beam particle. A measure of the 1460 keV background γ ray was needed for a correction to the measured γ-ray intensities as described in Section 5.3.4. The γ singles trigger was first downscaled to 100 for 17 runs, then 25 for 54 runs, and then 10 for the last 108 runs. The reason the downscale value was changed throughout the experiment was due to a misunderstanding of the deadtime calculation during the experiment. The goal was to set the downscale value such that there would be enough 1460 keV γ rays per run to make the correction described in section 5.3.4, but to not significantly affect the deadtime. As discussed in Section 3.5 the deadtime must be calculated independently for each trigger. During the experiment it was not calculated this way so the downscale value for the γ singles trigger was set lower (twice) because it appeared that it did not affect the deadtime significantly. However, the livetime of the other

triggers were affected by the subsequent high γ singles rate. To calculate the livetime of any one of the triggers comprising the final trigger (i.e. particle-γ coincidence trigger) only runs with the same downscale values can be used. This ultimately applies to the calculation of the partial cross sections in Section 5.4.4.

To measure the inclusive cross section only particle data is needed. Therefore, in the runs used to measure the inclusive cross section of ^{9}Be(^{34}Si,^{32}Mg)X the trigger was particle singles only. The downscale value was set to one in order to accept all the particle data. See Section 5.4.1 for the description of the calculation of the inclusive cross section.

5.3 Analysis of the ^{32}Mg spectrum

5.3.1 Particle identification

In the S800 spectrograph focal plane there were other isotopes besides the ^{32}Mg fragments of interest. They were primarily generated from reactions from the ^{34}Si secondary beam and the ^{9}Be target. To identify the ^{32}Mg fragments, first the Magnesium isotopes were identified in a time-of-flight versus energy-loss spectrum. The time-of-flight was measured between the object scintillator at the entrance to the S800 analysis line and a plastic scintillator in the S800 focal plane. Fig. 3.10 in Section 3.4 shows a schematic of the S800 spectrograph. The energy loss was measured in the ion chamber located in the S800 focal plane. The magnesium fragments were clearly separated by isotope in a time-of-flight versus angle in the focal plane spectrum which had the first particle identification gate applied. The angle in the focal plane was measured using the two CRDCs in the S800 focal plane. Fig. 5.2 shows the two particle-identification spectra.
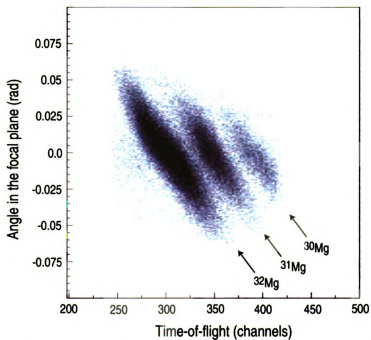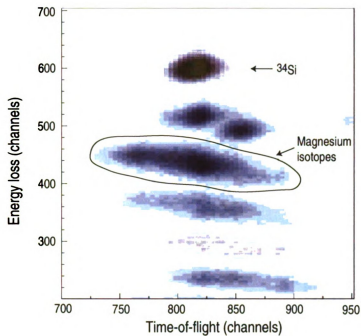
Figure 5.2: ^{32}Mg particle-identification spectra. The spectrum in the lower panel is gated on the gate drawn on the spectrum in the upper panel.
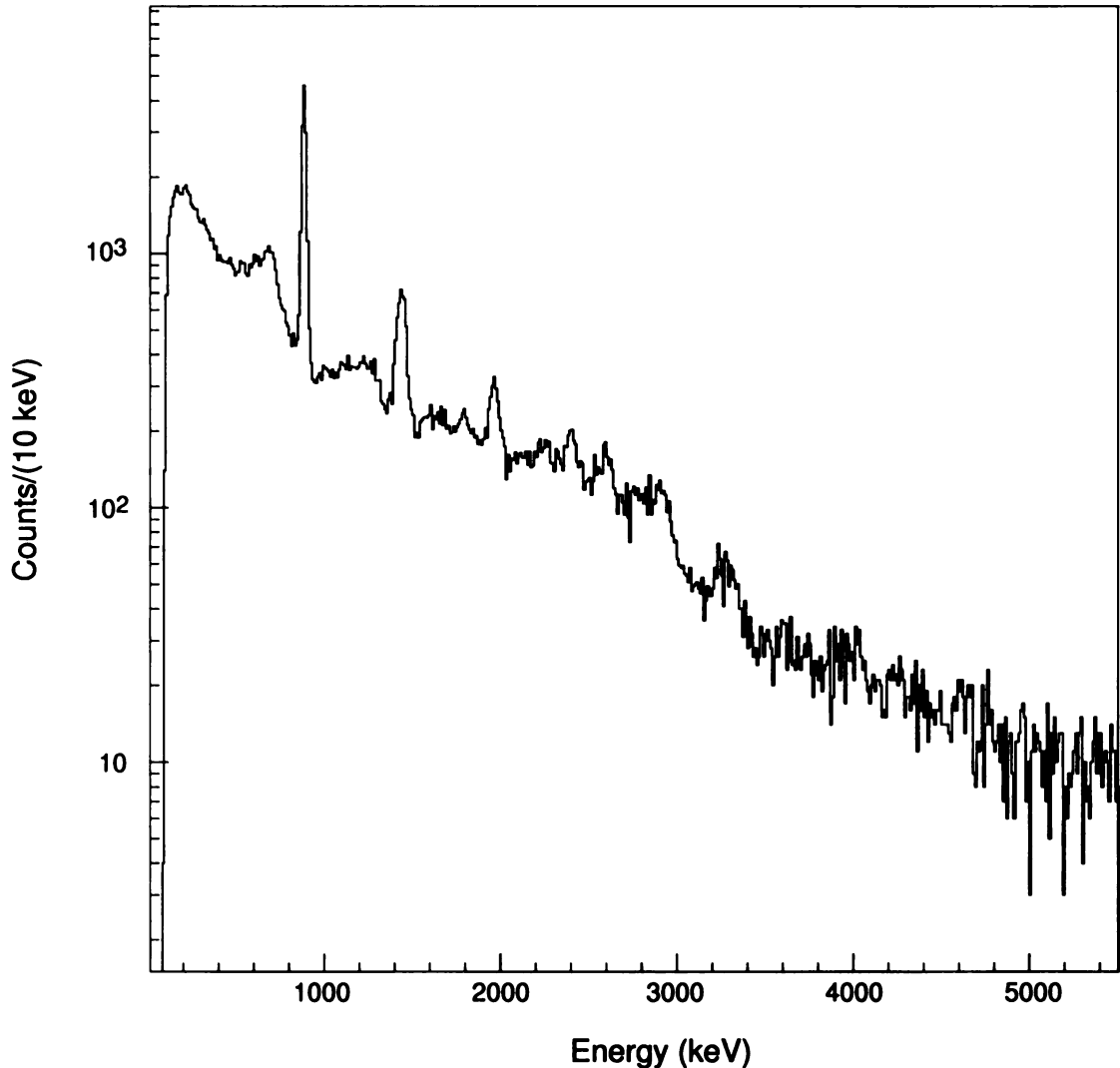
Figure 5.3: ^{32}Mg γ-ray spectrum containing the sum of all 18 detectors from SeGA. Below approximately 250 keV, there is a loss of counts due to the low-energy threshold of the SeGA detectors.

5.3.2 Doppler correction

As discussed in Section 3.3.5 the Doppler correction was performed using the known 885 keV $2^+ \rightarrow 0^+_{g.s.}$ γ ray. Fig. 5.3 shows the Doppler corrected ^{32}Mg γ-ray energy spectrum. Three of the γ-rays have been previously observed, namely the 885 keV, 1964 keV and 1438 keV γ rays. (See Section 1.4.1 for a discussion of the previously observed γ rays in ^{32}Mg.) The accepted half-life for the known (885.3 ± 0.1) keV $2^+ \rightarrow 0^+_{g.s.}$ γ-ray transition in ^{32}Mg is (11.4 ± 2.0) ps [87]. Since the energy spectra
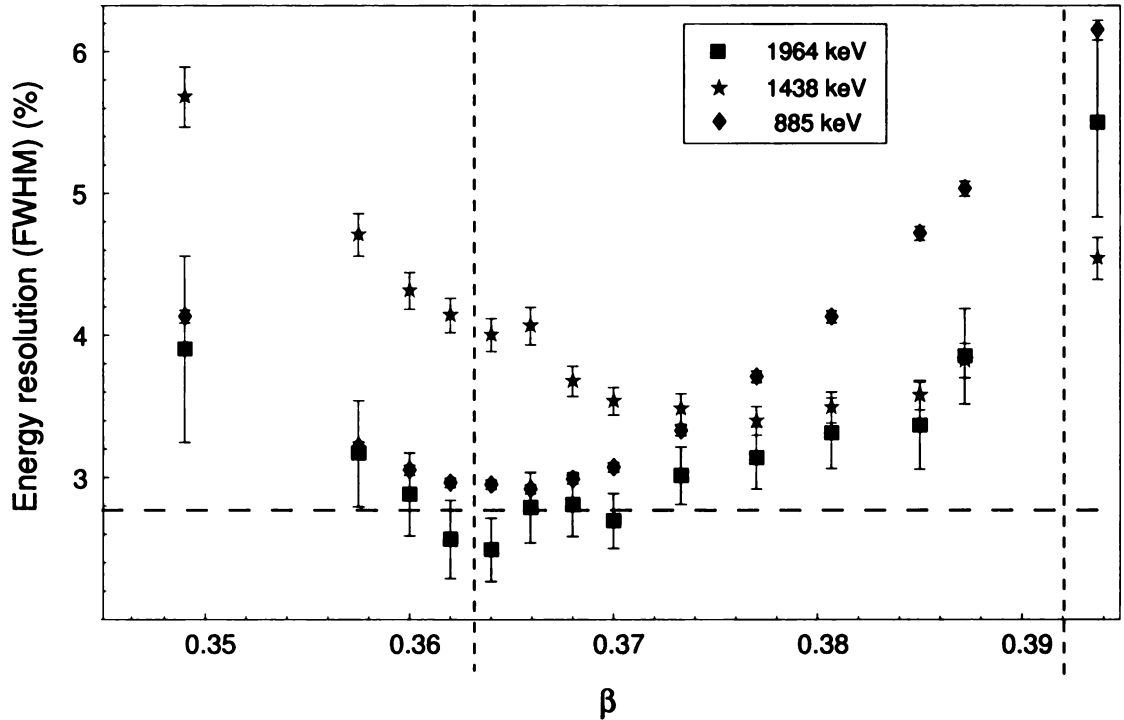
Figure 5.4: Energy resolution versus β for three prominent γ rays in the ^{32}Mg γ-ray spectrum. The energy resolution of the 1438 keV peak is the energy resolution assuming it is one peak. The horizontal dashed line illustrates the GEANT energy resolution of the 885 keV γ-ray peak (with a half-life of 11.4 ps) and also the GEANT energy resolution of the 1438 keV γ-ray peak (with a half-life of 0 ps). The vertical dashed lines indicate the position of the target. The larger β values correspond to the upstream beam direction.

were Doppler corrected using the 885 keV peak, those γ rays which do not have a half-life of approximately 11.4 ps will have a larger energy resolution and be offset in energy. The energy centroid is only affected by a few keV and will be addressed in Section 5.3.4. The γ-ray peak resolutions as a function of β can give information about the half-life of the observed γ-ray transitions. As discussed in Section 3.3.5, the Doppler correction has four parameters which must be optimized: β, x_o, y_o and z_o. Fig. 5.4 shows energy resolution versus β and Fig. 5.5 shows energy resolution versus z_o for three prominent γ rays in the ^{32}Mg spectrum. As can be seen in Fig. 5.5, the z_o position does not affect the energy resolution within ± 0.2 cm. From Fig. 5.4, it is obvious that the β value that gives the smallest energy resolution for the 885 keV γ-ray peak is lower than the β value that gives the smallest energy resolution for the
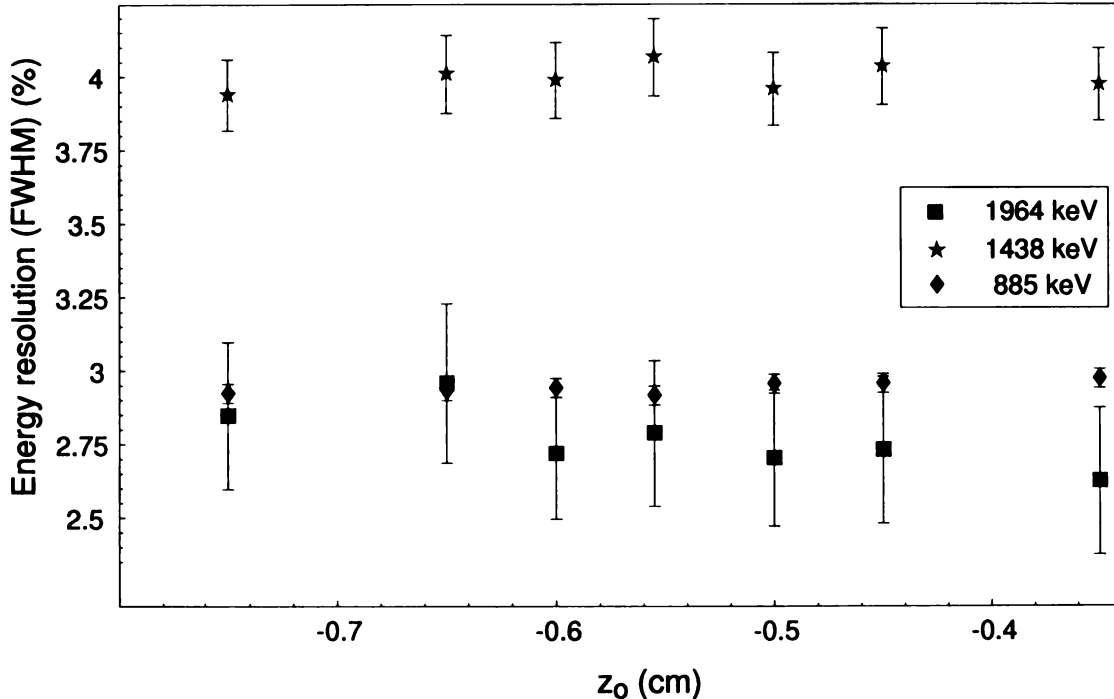
Figure 5.5: Energy resolution versus z_o for three prominent γ rays in the ^{32}Mg γ-ray spectrum. The energy resolution of the 1438 keV peak is the energy resolution assuming it is one peak.

1438 keV γ-ray peak.

The β value which produces the minimum energy resolution for the 1438 keV peak (assuming it is one peak) is $\beta = 0.3770 \pm 0.0047$. That value of β is consistent with a γ-ray transition with a half-life of $(0 - 3.5)$ ps. A half-life of 0 ps, versus 3.5 ps, gives the greatest energy resolution (because of the largest contribution to $\Delta\beta$). Using GEANT, the energy resolution of the entire SeGA of a single 1438 keV γ ray with a 0.0 ps half-life is $2.76 \pm 0.02\%$ (FWHM). As can be seen in Fig. 5.4, the minimum experimental energy resolution is $3.41 \pm 0.10\%$ (FWHM) for the sum of the entire SeGA. This gives strong evidence that the peak around 1438 keV is a doublet. To confirm that the 1438 keV peak was not one peak, it was fit with a 0.0 ps half-life simulated response. The response was too narrow for the data. The minimum experimental energy resolution of the entire SeGA of the 885 keV γ-ray peak is $(2.913 \pm 0.030)\%$ (FWHM) and the GEANT energy resolution is $(2.782 \pm 0.004)\%$

80
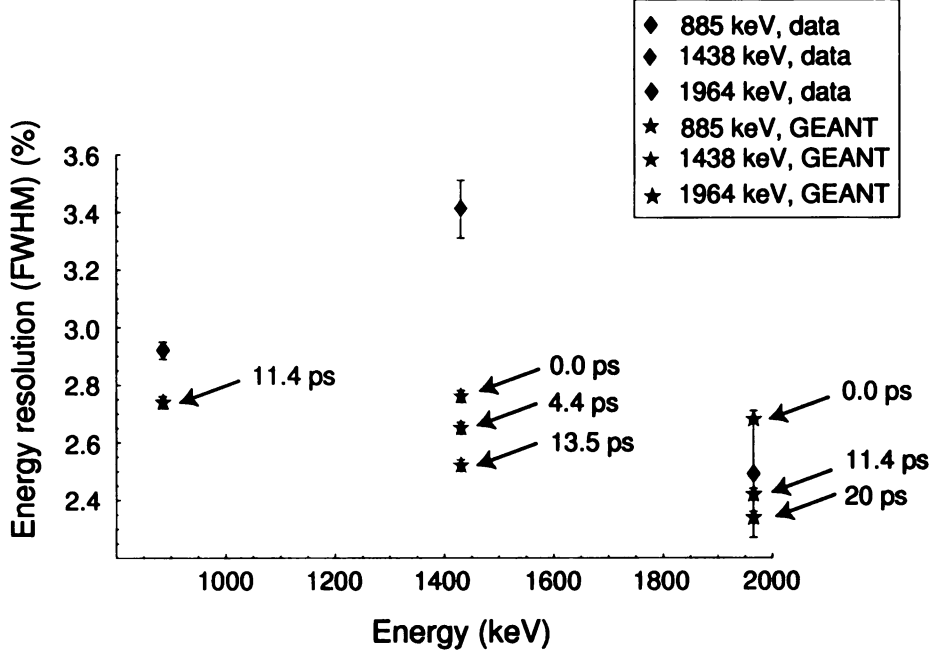
Figure 5.6: Energy resolution versus energy for three prominent γ rays in the ^{32}Mg γ-ray spectrum. The experimental data is shown by diamonds. The GEANT simulated resolutions are shown for a few different half lives for the 1438 keV and 1964 keV peaks as labeled on the figure.

(FWHM). The small difference between the GEANT simulated energy resolution and the experimental energy resolution for the 885 keV peak cannot account for the large difference observed for the 1438 keV peak between simulation and experiment. This is illustrated in Fig. 5.6. Shown are the experimental and simulated, by GEANT, energy resolutions of the entire SeGA for the 885 keV, 1438 keV and 1964 keV γ rays. The GEANT simulations are for a few different half lives for the 1438 keV and 1964 keV peaks. Therefore, it is clear that the peak at 1438 keV is a doublet.

The energy resolution of the sum of the two peaks around 1438 keV corresponds to an effective half-life of $(0 - 3.5)$ ps (as discussed above). The half-lives of the individual peaks are not known. The unknown doublet parameters are then related as,

$$(0 - 3.5) \text{ ps} \geq \frac{(I_a/I_b)T_{1/2}^a + T_{1/2}^b}{(I_a/I_b) + 1}, \tag{5.1}$$

where a and b denote the two peaks comprising the doublet, $T_{1/2}^a$ and $T_{1/2}^b$ are the

half lives in ps and I_a and I_b are the peak intensities. Another unknown parameter is the energy spacing dE between the peaks.

5.3.3 Doublet parameter study

To gain insight on the individual peaks of the 1438 keV doublet a parameter study was performed. The experimental 1438 keV peak in the summed spectrum of all nine SeGA detector angle pairs was fit with two GEANT simulated peaks, a and b, each with a given half life ($T^a_{1/2}$ and $T^b_{1/2}$), intensity (I_a and $I_b = 1 - I_a$) and energy spacing between the two peaks (dE). The parameters looped over all combinations allowed by Eq. 5.1 of $T^a_{1/2} = 0, 1, 2, 3, 4, 5, 6, 7, 8$ ps, $T^b_{1/2} = 0, 1, 2, 3, 4, 5, 6, 7, 8$ ps, $I_a = 0.03, 0.06, 0.09, ..., 0.87, 0.9$ and $dE = 0, 5, 10, ..., 55, 60$ keV. An initial set of fits was performed with coarser half-life increments up to 30 ps which showed the minimum χ^2 occurred when $T^a_{1/2}$ and $T^b_{1/2}$ were both less than 8 ps. The intensities were chosen such that each peak could range to approximately 30 times the other in magnitude. A maximum energy spacing, dE, of 60 keV was chosen because a peak shape characteristic of two peaks would have been apparent in the experimental summed energy spectrum if the energy spacing was greater than approximately 60 keV; this was not observed. For each combination of parameters allowed by Eq. 5.1, the fit was performed and the χ^2 value was recorded. For a given parameter, the 1σ uncertainty was determined by fixing the other three parameters and looking at what values of the parameter gave χ^2 values up to $\chi^2_{min} + 1$. The resulting uncertainties in the dE and I_a parameters were on the order of the step size. The uncertainties in $T^a_{1/2}$ and $T^b_{1/2}$ are on the order of the step size, but the generated GEANT response functions are not sensitive to half-life increments smaller than 1 ps. Therefore a final set of fits was performed where $T^a_{1/2}$ and $T^b_{1/2}$ looped over the same values listed above, but I_a and dE varied with $I_a = 0.75, 0.76, ..., 0.80, 0.81$ and $dE = 25, 26, ..., 34, 35$ keV. The values of the parameters which give a global minimum, with their 1σ error bars, are $T^a_{1/2} = 3^{+1}_{-0}$ ps, $T^b_{1/2} = 1^{+3}_{-1}$ ps, $I_a = 0.77^{+0.04}_{-0.02}$, and $dE = 29^{+2}_{-1}$ keV. Peak a is the
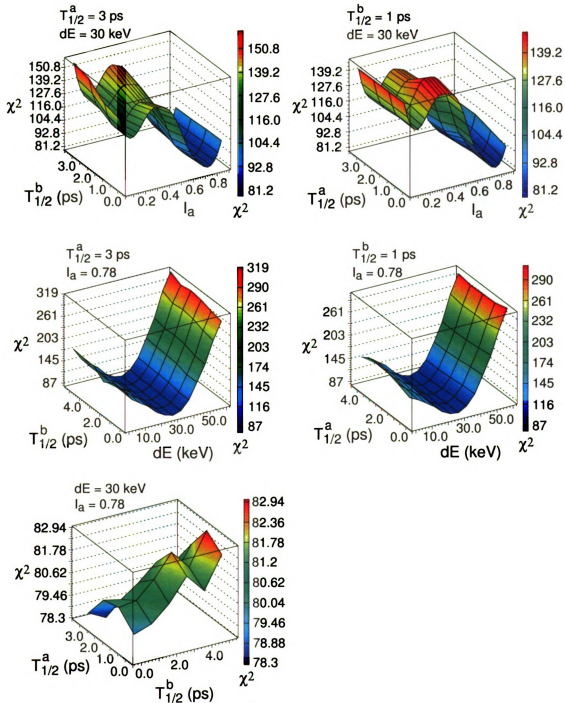
Figure 5.7: Three-dimensional plots illustrating the goodness-of-fit χ^2 values versus different parameters, for the experimental γ-ray spectrum fit with GEANT simulated response functions in which the four parameters looped over $T^a_{1/2} = 0, 1, 2, 3, 4, 5, 6, 7, 8$ ps, $T^b_{1/2} = 0, 1, 2, 3, 4, 5, 6, 7, 8$ ps, $I_a = 0.03, 0.06, 0.09, ..., 0.87, 0.9$ and $dE = 0, 5, 10, ..., 55, 60$ keV. Each plot shows the region around the global minimum as a function of two of the four parameters. The two fixed parameters are given in the upper left of each plot.
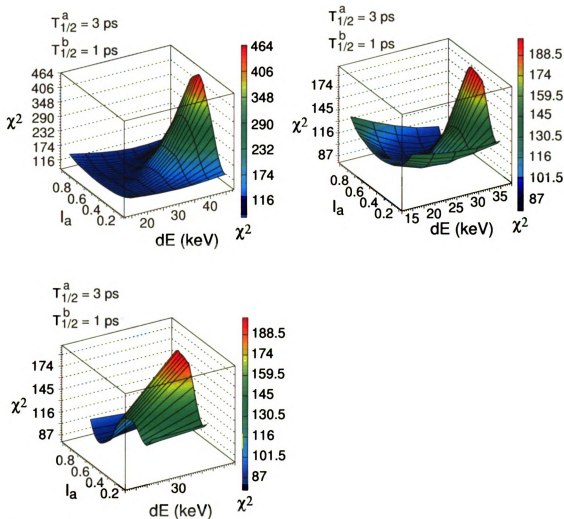
Figure 5.8: Three-dimensional plots illustrating the goodness-of-fit χ^2 values versus different parameters, for the experimental γ-ray spectrum with GEANT simulated response functions in which the four parameters looped over $T^a_{1/2} = 0, 1, 2, 3, 4, 5, 6, 7, 8$ ps, $T^b_{1/2} = 0, 1, 2, 3, 4, 5, 6, 7, 8$ ps, $I_a = 0.03, 0.06, 0.09, ..., 0.87, 0.9$ and $dE = 0, 5, 10, ..., 55, 60$ keV. For each plot the x and y axes are dE and I_a, respectively. Each successive plot is over a smaller energy range than the previous plot (going left to right, top to bottom).
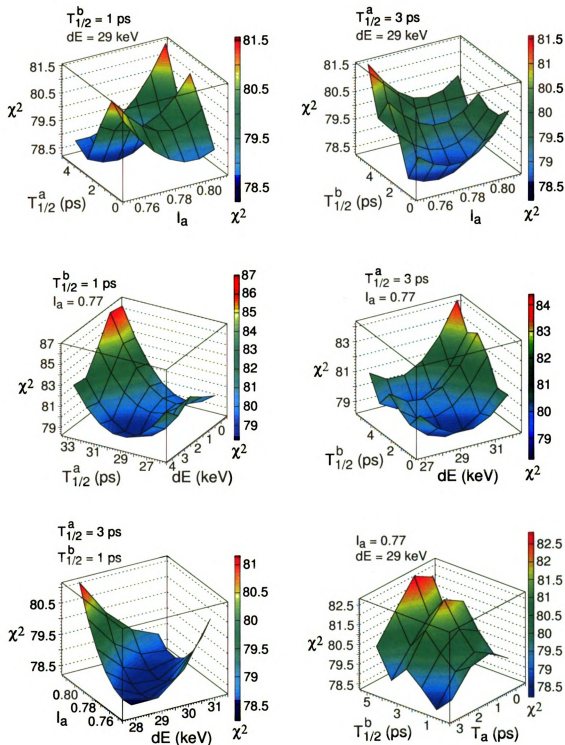
Figure 5.9: Three-dimensional plots illustrating the goodness-of-fit χ^2 values versus different parameters, for the experimental γ-ray spectrum with GEANT simulated response functions in which the four parameters looped over $T_{1/2}^a = 0, 1, 2, 3, 4, 5, 6, 7, 8$ ps, $T_{1/2}^b = 0, 1, 2, 3, 4, 5, 6, 7, 8$ ps, $I_a = 0.75, 0.76, ..., 0.80, 0.81$ and $dE = 25, 26, ..., 34, 35$. Each plot shows the region around the global minimum as a function of two of the four parameters. The two fixed parameters are given in the upper left of each plot.

higher energy peak and peak b is the lower energy peak. Figs. 5.7, 5.8 and 5.9 show three-dimensional plots illustrating the goodness-of-fit χ^2 values versus different parameters, for the experimental γ-ray spectrum fit with GEANT simulated response functions. In all of the figures the z axis and color indicate χ^2. The figures show selected slices or sections of the parameter space that illustrate the location of the global minimum.

5.3.4   Fitting the ^{32}Mg γ-ray energy spectrum

For each pair of SeGA detectors at a given angle θ, with respect to the beam axis, the ^{32}Mg γ-ray spectrum was fit from 650 to 3800 keV with simulated response functions from GEANT plus an exponential background. To generate simulated response functions for the two peaks around 1438 keV, the half-lives and energy separation results from the parameter study were used. (See Section 5.3.3 for the results of the parameter study.) When fitting the spectra all peak magnitudes were allowed to vary freely. The intensity ratio between the two peaks around 1438 keV could not be fixed for the SeGA angle pair spectra because the parameter study used the summed spectrum of all the SeGA detectors. If the two γ rays around 1438 keV have angular distributions, then fixing the intensity ratio for each SeGA angle pair would be incorrect. When fitting the spectra, offsets (in energy) for each GEANT response function were allowed to vary to account for unknown energies and half-lives of most of the γ-ray peaks. The calculation of the energy centroids of the γ-ray peaks is discussed at the end of this section. Fig. 5.10 shows the 40° SeGA angle pair γ-ray spectrum fitted with nine simulated response functions plus an exponential background. The other eight SeGA angle pairs were fit likewise. The summed spectrum, of all nine SeGA angle pairs, was fit likewise except the intensity ratio between the two peaks around 1438 keV was fixed from the parameter study results. The fit to the summed spectrum was used to obtain the energies of the γ-ray peaks and the partial cross sections of the two states which decay by the two γ rays around 1438 keV. The fits to the SeGA angle pair
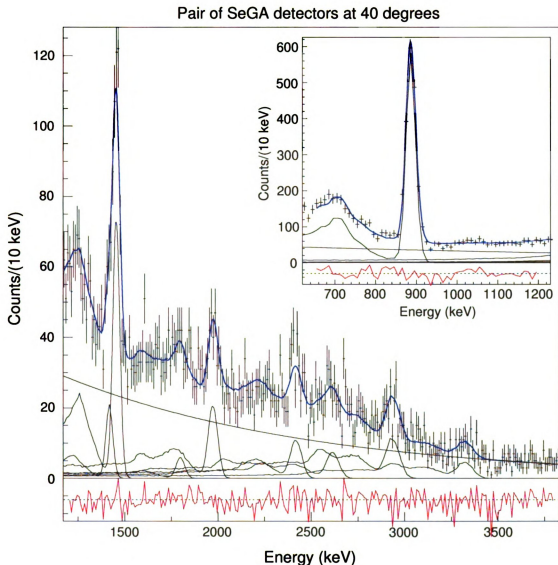
Figure 5.10: ^{32}Mg γ-ray spectrum of the pair of SeGA detectors at 40° fit with GEANT response functions. The spectrum was fit from 650-3800 keV. The spectrum was fit with nine GEANT response functions and an exponential background. The inset shows the fit from 650-1200 keV. In the figure, the fit (blue), individual response functions (black) and exponential background (black) are shown on the spectrum. The residual (red) between the fit and the data points is shown below the spectrum.

spectra were used to obtain γ-ray angular distributions and partial cross sections for the other observed γ rays and excited states, respectively.

After the ^{32}Mg γ-ray energy spectra were fit with GEANT response functions, four corrections had to be applied to obtain the γ-ray intensities and partial cross sections shown in Tables 5.5 and 5.6. Two of the corrections must be applied to each detector angle pair. One is a GEANT scale factor. The detector efficiency as simulated by GEANT does not exactly match the experimental source efficiency for each detector angle pair. The GEANT scale factor corrects for this discrepancy. The scale factor is dependent on the angle of the detector to the beam axis (θ) and the detected γ-ray energy. The scale factors for the different angle pairs for the 885 keV γ ray ranged from 0.89 to 1.05. The other correction that must be applied to each detector angle pair is a correction for an effect where the detectors became 'paralyzed'. This happened after certain events and caused the particular SeGA detector affected to be unable to detect another γ ray for a finite amount of time. It is thought to be caused by scattered particles hitting the SeGA detector crystal and saturating the preamplifier. Cursory inspection of the preamplifier signal for one of the SeGA detectors at 24° indicates the preamplifier is saturated for approximately 1 ms. The detectors at forward angles were affected much more than detectors at backward angles. This effect was quantified by measuring the peak area of the background γ ray at 1460 keV in and out-of-beam for each detector. The area of the 1460 keV γ-ray peak per unit time should stay constant in and out-of-beam. Measuring the discrepancy gives a measure of the amount the detectors are paralyzed. Fig. 5.11 shows the ratio of 1460 keV γ rays in and out-of-beam as a function of detector angle. The points are normalized such that the 147° detectors have a value of one. This introduces a systematic error of 5.6% that is not shown on the error bars in the figure.

For the two peaks around 1438 keV the fit to the summed spectrum was used to obtain the partial cross sections for those peaks (as stated above). The GEANT scale factor used for these two peaks was not the GEANT scale factors for the individual
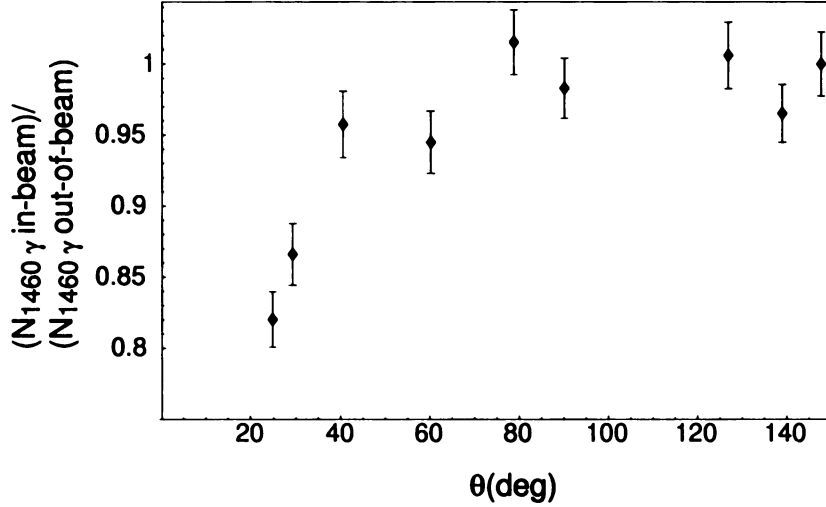
Figure 5.11: Plot of the number of in-beam 1460 keV γ rays divided by the number of out-of-beam 1460 keV γ rays as a function of detector angle.

angle pairs, but a scale factor calculated by comparing the measured efficiency of the sum of the entire SeGA to the efficiency of the entire SeGA as simulated in GEANT. For the problem of the detectors becoming paralyzed, an 'effective' correction for the entire array was calculated using the five largest γ rays (excluding the two peaks around 1438 keV) in the γ-ray spectrum. For those five γ rays, using the fit from the summed spectrum (of all nine SeGA angle pairs) and the fits of the SeGA angle pair spectra an effective detector 'paralyzation' value could be calculated.

The other two corrections to the to the γ-ray intensities, which are detector angle independent, are a livetime correction and a correction due to data loss. The particle-γ coincidence trigger was not 100% efficient. For the runs used to obtain the γ-ray intensities the coincidence trigger livetime was 0.7755 ± 0.0006. During the ^{32}Mg experiment some coincidence trigger data was lost due to a readout programming error. The amount of data lost was independent of detector angle. The amount of data lost for the runs used to get the γ-ray intensities was $(11.5 \pm 0.1)\%$. In Table 5.1 is a summary of the four corrections to the γ-ray intensities and their magnitudes.

The γ-ray peak energies were calculated from the results of the fit to the summed spectrum of all nine SeGA angle pairs. The energy centroids for the γ-ray peaks were

Table 5.1: Summary of corrections to ^{32}Mg γ-ray intensities. See text for description of corrections.

Correction	Value
GEANT scale factor	0.89 - 1.05 (detector angle and γ-ray energy dependent)
correction for paralyzed detectors	0.82 - 1.0 (detector angle dependent)
coincidence trigger livetime	0.7755 ± 0.0006
data loss	0.115 ± 0.001

calculated for each γ ray by taking the centroid of the GEANT simulated γ-ray peak and subtracting the fitted offset for that peak. The fitted offsets for all the γ rays were ≤ 6.1 keV. From the parameter study the spacing between the two doublet peaks, dE, was determined (see Section 5.3.3 for the results of the parameter study) and this was implemented in the fitting of the doublet. Therefore in the calculation of the energy centroid of the 1414 keV γ ray, dE was also subtracted. The total uncertainty on the energy centroids of the γ rays reported in Table 5.5 include the uncertainty in the centroid of the GEANT simulated γ-ray peak (≤ 0.14 keV for all γ rays), uncertainty in the fitted offset (≤ 5.6 keV for all γ rays), and an uncertainty due to not knowing the half-lives of the γ rays (explained below). For the 1414 keV γ ray there is an additional uncertainty of 2 keV due to the 29 keV spacing between the two peaks comprising the doublet. All of the uncertainties are added in quadrature.

As mentioned in the beginning of Section 5.3.2, since the Doppler correction of the ^{32}Mg γ-ray energy spectrum was performed using the 885 keV γ ray, those γ-ray transitions with different half-lives than the 885 keV γ ray will be Doppler corrected to energies a few keV above or below the emitted γ ray energy. The uncertainties on the centroids reported in Table 5.5 have a systematic uncertainty folded in to account for the fact that the half-lives of the γ rays in the ^{32}Mg energy spectrum are not known. The magnitude of the uncertainty was estimated using GEANT simulations in the following way. In GEANT, simulations of γ rays were performed using mismatched β and half-life values and the deviation in the energy centroids of the simulated γ rays versus the inputted γ ray energies were recorded. For example, a simulated

2000 keV γ ray with a half-life of 40 ps was Doppler reconstructed with a β value corresponding to a 0 ps half-life. The centroid of the resulting simulated peak was recorded. Likewise a simulated 2000 keV γ ray with a half-life of 0 ps was Doppler reconstructed with a β value corresponding to a 40 ps half-life. This was done for multiple half-life and β combinations for two different energy γ rays. The maximum deviation of the simulated energy centroid from the energy of the γ ray that was inputted into GEANT scaled linearly with energy. Therefore for the 1964 keV γ ray the magnitude of the uncertainty of the energy centroid due to not knowing the half-life is ± 8.69 keV. (The resolution of the 1964 keV γ-ray peak in the γ-ray spectrum of all SeGA angle pairs is approximately 2.5% which corresponds to a FWHM of 50 keV.) Scaling with energy, the uncertainty of the 2912 keV γ ray is ± 12.89 keV. The uncertainties are scaled likewise for the other γ rays.

5.4 Results and Discussion

5.4.1 Inclusive Cross Section

The inclusive cross section, σ_{incl}, for the two-proton knockout of ^{34}Si to ^{32}Mg was calculated by taking the ratio of the number of livetime and efficiency corrected ^{32}Mg fragments detected in the S800 focal plane to the number of incident ^{34}Si nuclei, normalized to the number of livetime and efficiency corrected incident ^{34}Si beam particles and multiplied by the target number density,

$$\sigma_{incl} = \frac{N^f(^{32}\text{Mg})/(N^f(^{34}\text{Si total}) * LT^f_{\text{S800 trig}} * Eff^f_{crdcs}(^{32}\text{Mg}) * Eff^f_{obj}(^{34}\text{Si}))}{N(^{34}\text{Si})/(N(^{34}\text{Si total}) * LT_{\text{S800 trig}} * Eff_{crdcs}(^{34}\text{Si}) * Eff_{obj}(^{34}\text{Si}))} * \sigma_{tar},$$

(5.2)

where

$$\sigma_{tar} = \frac{A_t * 10^{27}}{t * N_A}.$$

(5.3)

In the calculation of the target number density, σ_{tar} in barns, A_t is the atomic mass of the ^{9}Be target in g/mol, t is the thickness of the target in g/cm^2 and N_A is Avogadro's number (mol^{-1}). In the numerator of Eq. 5.2, the number of ^{32}Mg fragments, $N^f(^{32}$Mg), was determined by the number of counts in the particle identification gate. (Section 5.3.1 contains a discussion of the ^{32}Mg particle identification.) The total number of ^{34}Si nuclei, $N^f(^{34}$Si total), was determined using the object scintillator at the entrance to the S800 analysis beam line. The livetime of the trigger, the efficiency of the CRDCs and the efficiency of the object scintillator—$LT^f_{S800\text{ trig}}$, Eff^f_{crdcs} and Eff^f_{obj} respectively—were included. In the denominator, the number of ^{34}Si fragments, N(^{34}Si), was determined by a set of data where the S800 spectrograph magnetic fields were set to the rigidity of the incident ^{34}Si beam. The total number of ^{34}Si nuclei was determined using the object scintillator. The numerator and denominator were calculated using different sets of data because the spectrograph was set to different magnetic field settings. (The setting where the ^{32}Mg fragments are centered in the focal plane denoted by the superscript f on the terms in Eq. 5.2 and the setting where the ^{34}Si fragments are centered in the focal plane, respectively.) Therefore, the trigger livetime and two efficiency terms in the numerator do not cancel out with those in the denominator in Eq. 5.2. The magnitudes of these terms are not negligible. In Table 5.2 are the particle numbers, livetimes, and efficiencies used in the calculation of the ^{9}Be(^{34}Si,^{32}Mg)X inclusive cross section in Eq. 5.2. For the ^{32}Mg fragment setting, the rate on the object scintillator was 33557 particles/second and the rate in the S800 focal plane was 32 particles/second. For the ^{34}Si setting, the rate on the object scintillator was 291 particles/second and the rate in the S800 focal plane was 154 particles/second.

The inclusive cross section calculated from Eq. 5.2 must be corrected for loss of acceptance in the S800 spectrograph focal plane. There are two effects. Firstly, at the edges of the focal plane the momentum distribution gets slightly distorted. Secondly, the entire ^{32}Mg momentum distribution did not fit into the acceptance of the focal

Table 5.2: Particle numbers, livetimes, and efficiencies used for the $^9\text{Be}(^{34}\text{Si},^{32}\text{Mg})\text{X}$ inclusive cross section calculation in Eq. 5.2.

Variable	Value
$N^f(^{32}\text{Mg})$	2333 ± 48
$N^f(^{34}\text{Si total})$	252967878 ± 15905
$LT^f_{\text{S800 trig}}$	0.985 ± 0.003
$Eff^f_{crdcs}(^{32}\text{Mg})$	0.975 ± 0.022
$Eff^f_{obj}(^{34}\text{Si})$	0.956 ± 0.019
$N(^{34}\text{Si})$	92039 ± 303
$N(^{34}\text{Si total})$	203008 ± 451
$LT_{\text{S800 trig}}$	0.875 ± 0.004
$Eff_{crdcs}(^{34}\text{Si})$	1.0 ± 0.0^a
$Eff_{obj}(^{34}\text{Si})$	1.000 ± 0.005

^{a}The CRDCs were not used in the identification of the ^{34}Si fragments therefore the CRDC efficiency correction is identically one.

plane. These corrections were estimated based upon a previous measurement of the same reaction [44,88]. The total acceptance correction was 11.5%.

Therefore, the inclusive cross section for the $^9\text{Be}(^{34}\text{Si},^{32}\text{Mg})\text{X}$ reaction is (0.86 ± 0.08) mb. This is in agreement with the inclusive cross section of (0.76 ± 0.10) mb determined in a previous measurement [44].

In addition to the ^{32}Mg fragments, ^{31}Mg fragments were also detected in the S800 focal plane as seen in Fig. 5.2. The observed inclusive cross section of the reaction $^9\text{Be}(^{34}\text{Si},^{31}\text{Mg})\text{X}$ is (0.403 ± 0.026) mb. This measurement represents a lower limit on the true inclusive cross section for two experimental reasons. Firstly, in the S800 focal plane ^{31}Mg was severely cut off in acceptance because the ^{32}Mg fragments were centered in the focal plane. Secondly, the momentum distribution of the ^{31}Mg fragments is expected to be wider than the distribution of the ^{32}Mg fragments since the reaction process leading to ^{31}Mg has a non-direct component. The location of the center of the ^{31}Mg momentum distribution cannot be determined in the data. But, because the momentum distribution of the ^{31}Mg fragments is expected to be wider than the momentum distribution of the ^{32}Mg fragments, it can be concluded that more than half of the ^{31}Mg momentum distribution does not fit in the acceptance of the S800
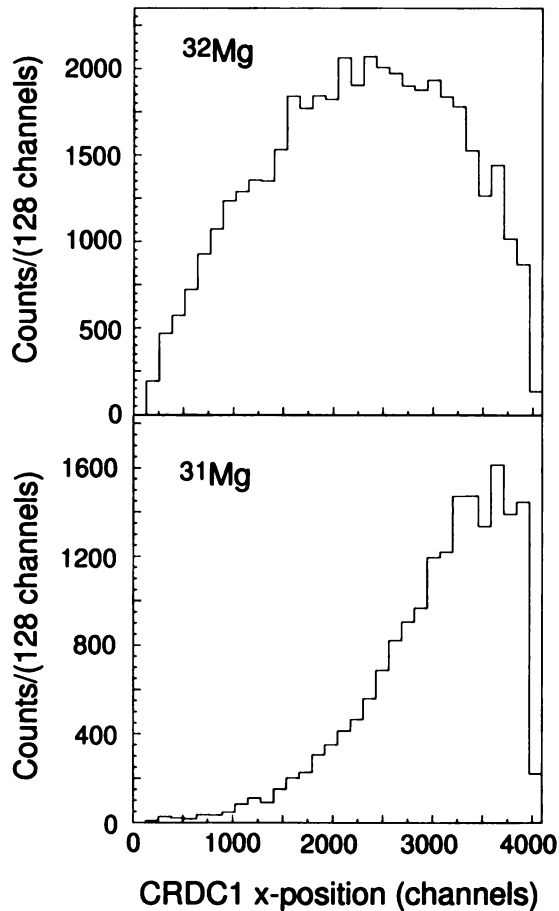
Figure 5.12: Fragment yield versus the x-position distributions of ^{32}Mg and ^{31}Mg fragments in the S800 focal plane. Both spectra are gated on the *and* of the Magnesium isotopes gate drawn on the top panel of Fig. 5.2 and the corresponding isotope from the bottom panel of Fig. 5.2.

focal plane. Therefore, the 0.403 mb lower limit of the inclusive cross section for the production of ^{31}Mg is significantly less than what the true inclusive cross section for the reaction ^{9}Be(^{34}Si,^{31}Mg)X would be if ^{31}Mg was not being cut in the S800 focal plane. Fig. 5.12 shows the x-position distributions of the ^{32}Mg and ^{31}Mg fragments in the S800 focal plane. The reduction of counts in the highest and lowest channels in the x-position distributions in Fig. 5.12 is due to a loss of acceptance at the edges of the CRDC.

Discussion

Using the theory of two-nucleon stripping reactions as presented in [86], with shell-model wavefunctions calculated by B. A. Brown [89] and nuclear radii from B. A. Brown's (Skyrme SKX) Hartree-Fock calculations [90], J. Tostevin [91] calculates an inclusive cross section for the ^{9}Be(^{34}Si,^{32}Mg)X reaction of 2.76 mb. The shell-model calculation predicts 0^+, 2^+ and 4^+ sd states at 2.41 MeV, 4.09 MeV, and 5.31 MeV with partial cross sections of 0.42 mb, 0.98 mb, and 1.36 mb, respectively. The sum of the partial cross sections to the 0^+, 2^+ and 4^+ states is 2.76 mb. This method of calculating the inclusive cross section by the stripping of two correlated nucleons has matched experimental inclusive cross sections reasonably well. Examples include two-proton and two-neutron knockout from ^{12}C at three different energies [92, 93], two-proton knockout from ^{28}Mg to ^{26}Ne [44, 86], two-proton knockout from ^{46}Ar to ^{44}S [94] and two-proton knockout from ^{44}S to ^{42}Si [94].

The 0^+, 2^+, and 4^+ sd states at 2.41 MeV, 4.09 MeV and 5.31 MeV are not observed in the experiment. The excited sd states are each thought to fragment over a few MeV to create the observed excited states. The ground state of ^{34}Si is dominated by the $0\hbar\omega$ configuration [95]. The deformed excited states in ^{32}Mg are not expected to be directly populated because there is very little overlap between the spherical and deformed state wavefunctions.

In the calculation of the two-nucleon knockout reaction cross sections, diffraction should also be included in addition to the stripping components. This is just beginning to be explored for two-nucleon knockout [91, 96]. In the calculation of the two-nucleon knockout inclusive cross sections, diffraction contributions seem to be approximately the same size as the stripping contributions. In one-nucleon knockout, in comparing the calculated inclusive cross section, including stripping and diffraction parts, to the experimental inclusive cross section for a given reaction, a reduction factor of approximately 0.5-0.7 [68, 97] is observed for normally to loosely-bound nuclei. These observed reduction factors give a measure of the correlations that are

absent in, or only approximately described by, the nuclear shell-model. These correlations arise from the repulsive core and tensor part of the nucleon-nucleon interaction (short-range) and also couplings to low-lying excitations and higher-lying giant resonances (long-range) [98,99]. In [96] it was suggested that the reduction factor needed for two-nucleon knockout reactions are approximately equal to the reduction factor for one-nucleon knockout squared. A reduction factor of approximately 0.5 for two-nucleon knockout is then reasonable. Including diffraction components is currently under investigation [91] and will not be pursued further here.

For the two-proton knockout of ^{34}Si to ^{32}Mg the calculated inclusive cross section of 2.76 mb is much larger than the measured inclusive cross section of (0.86±0.08) mb. A possible explanation for this difference is that some of the predicted strength to the 2^+ and 4^+ sd states is fragmented over a few MeV such that a significant fraction of the 2^+ and 4^+ strength could be above the ^{32}Mg neutron separation energy (S_n) of 5.809 MeV. For excitations above S_n a neutron would be emitted, leading to ^{31}Mg.

The observed inclusive cross section of (0.403±0.026) mb for the ^{9}Be(^{34}Si,^{31}Mg)X reaction has contributions from two processes. One is the two-step process where ^{32}Mg is produced then one neutron is emitted and the the other process is where ^{31}Mg is made directly in fragmentation from ^{34}Si. It is not possible to know how much of the observed inclusive cross section for the production of ^{31}Mg is due to which process. The observation of ^{31}Mg with an inclusive cross section of at least 0.403 mb is a plausible explanation why the observed inclusive cross section of ^{9}Be(^{34}Si,^{32}Mg)X is less than the expected cross section. The strength from the 2^+ and 4^+ sd states exciting levels above the neutron separation energy in ^{32}Mg leads to the emission of a neutron and observation of ^{31}Mg. If half of each of the partial cross sections that lead to the 4^+ and 2^+ sd states go into ^{31}Mg, then the expected inclusive cross section of ^{9}Be(^{34}Si,^{32}Mg)X would be (2.76 − 1/2(1.36) − 1/2(0.98) = 1.59) mb. The observed inclusive cross section is (0.86 ± 0.08) mb. More than half of the unobserved cross section can thus be explained. However, a better understanding of the structure of

^{32}Mg is needed to accurately predict the observed inclusive cross section and observed excited states.

5.4.2 Proposed level scheme

Fig. 5.13 shows the ^{32}Mg level scheme observed from the two-proton knockout reaction ^{9}Be(^{34}Si,^{32}Mg γ)X. The placement of the γ rays and energy levels was based upon γ-γ coincidence analysis and the observed γ-ray intensities. γ-γ coincidence data can give valuable information on the excited state level scheme of a nucleus. ^{32}Mg γ-γ coincidence data were obtained by requiring two prompt γ rays in two different SeGA detectors and a ^{32}Mg particle in coincidence. When analyzing the γ-γ coincidence spectra, two criteria were used to assert that two γ rays were in coincidence. Given two γ rays A and B, the first criterion compares the calculated with the observed number of γ rays of A in the γ-γ coincidence spectrum gated on B. The second criterion is the reverse; it compares the calculated with the observed number of γ rays of B in the γ-γ coincidence spectrum gated on A. If each of the two comparisons agree within 1σ, then it is asserted that two γ rays are in coincidence. The fits to the SeGA angle pair spectra were used to obtain the γ-ray intensities, I_{γ}, (as outlined in Sections 5.3.4 and 5.4.4) and are presented in Table 5.5. The last column in the table summarizes what γ rays were seen in coincidence with the listed γ ray. Placement of each γ ray is discussed below.

Fig. 5.14 shows the ^{32}Mg γ-ray energy spectrum in coincidence with the 885 keV $2_1^+ \rightarrow 0_{g.s.}^+$ γ-ray transition. While background was subtracted, the spectrum contains a large density of γ rays (compared, for example, to a spectrum gated on a higher-lying transition as shown in Fig.5.15) since all of the observed excited states deexcite through the 2^+ state at 885 keV. In the 885 keV γ-γ coincidence spectrum seven γ rays can be seen; the 1800 keV, 1964 keV, 2405 keV, 2599 keV, 2912 keV, and 3258 keV γ rays, and the doublet around 1438 keV. The 885 keV γ ray was the only γ ray observed in the γ-γ coincidence spectra of the 1800 keV, 1964 keV, 2599 keV
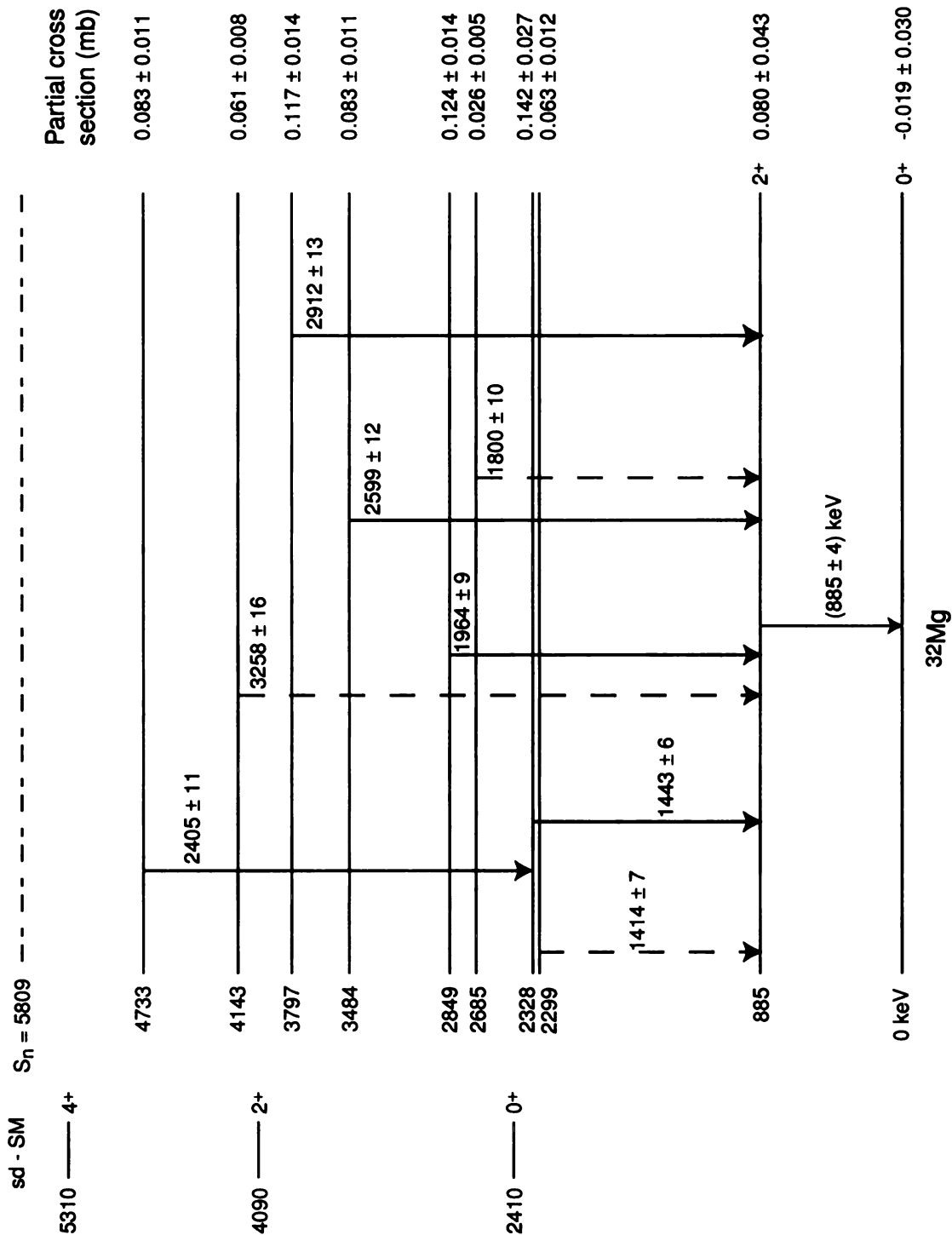
Figure 5.13: ^{32}Mg level scheme observed from the two-proton knockout reaction ^{9}Be(^{34}Si,^{32}Mg γ)X. The γ-ray energies and uncertainties in keV are labeled to the right of each γ ray. The excited state energies in keV are labeled to the left of each level. The partial cross sections in mb (discussed in Section 5.4.4) for each level are labeled to the right of each level. The sd states in keV, calculated in the shell-model (SM), are shown to the left of the level scheme.

98
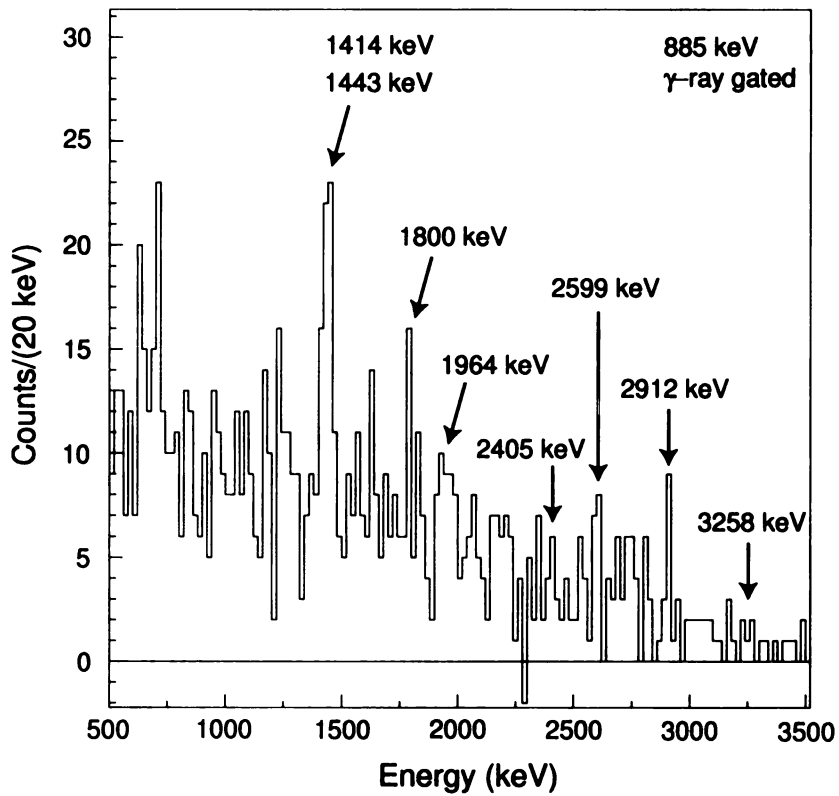
Figure 5.14: ^{32}Mg γ-ray energy spectrum in coincidence with the 885 keV γ ray. The background-subtracted spectrum contains a large density of γ rays; those placed in the level scheme are labeled.
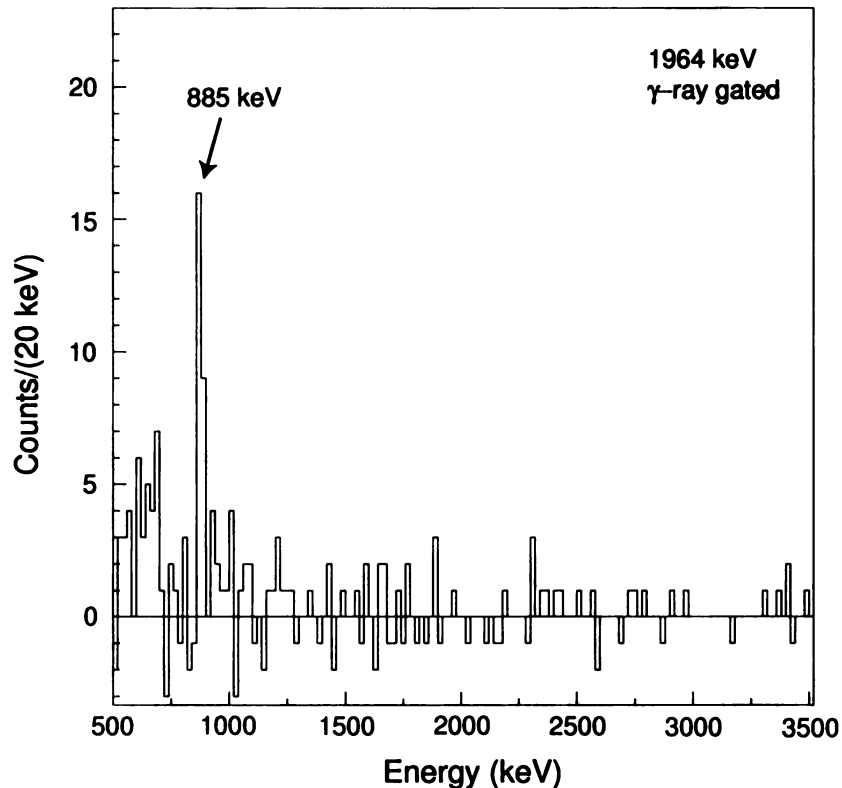
Figure 5.15: Background-subtracted ^{32}Mg γ-ray energy spectrum in coincidence with the 1964 keV γ ray. The 885 keV γ ray, in coincidence with the 1964 keV γ ray, is labeled.

and 3258 keV γ rays. This can be seen for the 1964 keV γ ray in Fig. 5.15 which shows the 1964 keV γ ray gated, background subtracted, γ-γ coincidence spectrum. The 1800 keV and 3258 keV γ rays are dashed on the level scheme because one of the two above discussed comparisons between the 1800 keV and 885 keV γ rays, and the 3258 keV and 885 keV γ rays, respectively, did not agree within 1σ.

The 1414 keV and 1443 keV γ rays comprise the doublet discussed in Sections 5.3.2 and 5.3.3. The 1443 keV γ ray is in coincidence with the 885 keV and 2405 keV γ rays as shown in the level scheme. The placement of the 1414 keV γ ray is uncertain. The more intense 1443 keV γ ray can be solely responsible for the observed γ-γ coincidence agreements with the 885 keV γ ray. However, it can not be excluded that the 1414 keV γ ray is in coincidence with the 885 keV γ ray. If the 1414 keV γ ray is the γ ray seen in the intermediate-energy Coulomb excitation experiments (as

proposed in Section 5.4.4), then there is no additional (besides the present experiment) experimental evidence for the 1414 keV γ ray to be in coincidence with the 885 keV γ ray. Therefore, the 1414 keV transition is dashed in the level scheme.

The 2405 keV γ ray is in coincidence with the 1443 keV and 885 keV γ rays and deexcites a state at 4733 keV. Fig. 5.16 shows the 2405 keV γ ray gated γ-γ coincidence spectrum containing the 885 keV and 1443 keV γ rays. The 2405 keV γ ray was determined to be in coincidence with the 1443 keV γ ray and not the 1414 keV γ ray for two reasons. Firstly, the intensity of the 2405 keV γ ray is greater than the intensity of the 1414 keV γ ray and less than the intensity of the 1443 keV γ ray. Secondly, the energy of the γ ray in the 2405 keV γ-γ coincidence spectrum agrees with 1443 keV.

The 2912 keV γ ray is in coincidence with the 885 keV γ ray and deexcites a state at 3797 keV. There is some weak evidence that the 2912 keV γ ray may be in coincidence with the 1414 keV γ ray and thus feed the 2299 keV level. Only one of the γ-γ coincidence comparisons (described above) between the 2912 keV and 1414 keV γ rays agreed within 1σ. Also, the 2912 keV γ ray is almost twice as intense as the 1414 keV γ ray. Therefore, it is assumed that the 2912 keV γ ray directly feeds the 885 keV state.

5.4.3 γ-ray angular distributions

As discussed in Chapter 2, γ-ray angular distributions can determine the multipolarities of γ rays. The ^{32}Mg γ-ray energy spectra were fit for each SeGA detector angle pair as described in Section 5.3.4. Many of the γ-ray angular distribution spectra for the different γ rays had large error bars due to low statistics and angle-dependent corrections to the fitted intensities described in Section 5.3.4. The experimental γ-ray angular distributions were fit with calculated $W(\theta)$ curves with fixed initial and final spins I_i and I_f, respectively, optimizing for the alignment, the multipole mixing ratio δ and the overall amplitude a. The multipole mixing ratio was in general not known.
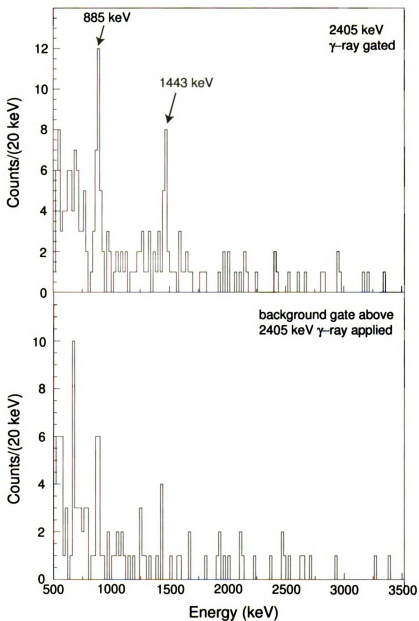
Figure 5.16: The ^{32}Mg γ-ray energy spectrum in coincidence with the 2405 keV γ ray is shown in the upper panel. The 885 keV and 1443 keV γ rays, in coincidence with the 2405 keV γ ray, are labeled. The background is shown in the lower panel.

Also, for each γ-ray transition the m substate distribution of the initial state, I_i, was not known. This alignment of a state can be oblate or prolate. (Section 2.3 defines oblate and prolate alignment.) As discussed in Section 5.4.1, J. Tostevin calculated the energies and partial cross sections of the sd states in ^{32}Mg from the ^{9}Be(^{34}Si,^{32}Mg γ)X reaction. The 2^+ and 4^+ excited states are predicted to have 15% and 24% prolate alignment, respectively. The alignments calculated for one-nucleon and two-nucleon knockout reactions are prolate and of similar magnitude. Section 2.5.3 briefly discusses one-nucleon knockout reactions and the calculated alignments. It is highly unlikely that different excited states could have oblate alignment. Therefore, in fitting the experimental γ-ray angular distributions the type of alignment was assumed to be prolate, but the amount of alignment was allowed to vary.

The error bars for the intensities at each angle for the different γ rays were too large to confine the amount of prolate alignment. For different I_i and I_f spin combinations, δ and σ values could be found such that the χ^2 was similar for all of the spin combinations tried. Table 5.3 gives a summary of the angular distribution fits performed and the results. The γ-ray angular distribution of the 2405 keV γ ray is shown in Fig. 5.17 and illustrates the above mentioned issues. Table 5.3 shows the γ-ray angular distributions are inconclusive. The different fits for each γ-ray transition have similar χ^2 values and are therefore indistinguishable from each other.

For each γ-ray transition fit with a $4 \to 2$ and/or a $6 \to 4$ spin transition, except the 885 keV γ ray, the γ-ray angular distribution data was also fit with $4 \to 2$ and $6 \to 4$ spin transitions where δ was fixed to zero and only a and σ were allowed to vary. The results of those fits gave the same a values which are in the table and gave σ values which were consistent with the results in the table for the respective γ-ray energy and I_i and I_f spins. The χ^2 values were similar to the χ^2 values of the other spin transition fits. (I.e. The χ^2 from the $3 \to 2$ spin transition fits.) Therefore, for all the $4 \to 2$ and $6 \to 4$ transitions, fixing $\delta = 0$ did not significantly change the results of the other fit parameters or significantly change the χ^2.

Table 5.3: Summary of results of fits of experimental γ-ray angular distributions. Listed are the γ-ray energies E_γ, initial I_i and final I_f spins, intensities a, measures of the degree of prolate alignment σ, the percentages of prolate alignment that σ corresponds to, the multipole mixing ratios δ and the χ^2 values of the fits. In each fit a, σ and δ were allowed to vary unless otherwise noted. I_i and I_f were fixed to the values listed. As can be seen by the large error bars for σ and δ, and the similar χ^2 values for each set of fits for a given E_γ, the present experiment is not able to distinguish different multipolarity transitions.

E_γ (keV)	I_i	I_f	a	σ	% alignment	δ	χ^2
885	2	0	0.540 ± 0.017	$4.70^{+\infty}_{-2.47}$	$2.2^{+7.4}_{-2.2}$	0^a	1.10
1800	3	2	0.017 ± 0.003	$0.02^{+\infty}_{-0.0199}$	100^{+0}_{-100}	$0.22^{+0.14}_{-0.13}$	3.05
1800	2	2	0.017 ± 0.003	$1.02^{+\infty}_{-1.0199}$	$36.3^{+63.7}_{-36.3}$	$3.67 \pm \infty$	3.03
1800	2	2	0.017 ± 0.003	$1.63^{+\infty}_{-1.07}$	$37.7^{+49.6}_{-37.7}$	$-0.34^{+0.64}_{-\infty}$	2.99
1964	3	2	0.081 ± 0.004	$0.45^{+2.53}_{-0.4499}$	$92.0^{+8.0}_{-82.8}$	0.23 ± 0.05	2.59
1964	2	2	0.081 ± 0.004	$0.67^{+2.43}_{-0.6699}$	$62.4^{+37.6}_{-57.3}$	$4.40^{+4.63}_{-1.55}$	2.59
1964	4	2	0.080 ± 0.004	$2.62^{+4.35}_{-0.76}$	$17.7^{+13.6}_{-15.0}$	$2.34^{+\infty}_{-0}$	2.40
2405	3	2	0.054 ± 0.004	$0.05^{+0.89}_{-0.0499}$	$100^{+0}_{-44.07}$	0.29 ± 0.06	1.55
2405	4	3	0.054 ± 0.004	$0.10^{+1.04}_{-0.099}$	$100^{+0}_{-43.78}$	0.27 ± 0.05	1.53
2405	2	2	0.054 ± 0.004	$0.92^{+\infty}_{-0.27}$	$42.2^{+22.1}_{-21.3}$	$1.70^{+1.61}_{-1.78}$	1.54
2405	4	2	0.054 ± 0.004	$1.20^{+0.62}_{-0.43}$	$53.6^{+21.2}_{-21.5}$	$-5.63^{+3.01}_{-127.77}$	1.35
2405	6	4	0.054 ± 0.004	$1.63^{+0.95}_{-0.76}$	$54.62^{+24.96}_{-22.69}$	$-30.69^{+24.92}_{-17.57}$	1.52
2599	3	2	0.054 ± 0.004	$3.61^{+\infty}_{-2.51}$	$6.4^{+40.4}_{-6.4}$	$0.34^{+\infty}_{-1.29}$	15.96
2599	2	2	0.055 ± 0.004	$1.04^{+\infty}_{-0.61}$	$35.3^{+54.6}_{-35.3}$	$6.25^{+\infty}_{-4.10}$	15.49
2599	4	2	0.055 ± 0.004	$1.78^{+3.78}_{-0.69}$	$33.2^{+25.6}_{-28.9}$	$-0.64^{+0.47}_{-4.11}$	14.64
2912	2	2	0.076 ± 0.004	$2.68^{+\infty}_{-1.54}$	$6.7^{+24.0}_{-6.7}$	$0.0 \pm \infty$	4.08
2912	3	2	0.076 ± 0.004	$4.61^{+\infty}_{-2.52}$	$4.0^{+13.6}_{-4.0}$	$2.99 \pm \infty$	4.07
2912	4	2	0.076 ± 0.004	$6.10^{+\infty}_{-3.22}$	$3.6^{+11.3}_{-3.6}$	$3.89 \pm \infty$	4.07
3258	3	2	0.040 ± 0.003	$0.01^{+0.52}_{-0.0099}$	$100.0^{+0.0}_{-14.2}$	$19.45^{+\infty}_{-0}$	11.92
3258	2	2	0.040 ± 0.003	$0.95^{+0.81}_{-0.33}$	$40.5^{+27.5}_{-25.6}$	$1.94^{+3.02}_{-\infty}$	14.16
3258	4	2	0.040 ± 0.003	$1.15^{+0.64}_{-0.57}$	$55.8^{+16.6}_{-23.1}$	$-4.11^{+2.17}_{-17.57}$	13.44

$^a\delta$ was set to zero and not allowed to vary because the 885 keV γ ray is known to be a $2^+ \rightarrow 0^+_{g.s.}$ (pure E2) transition.
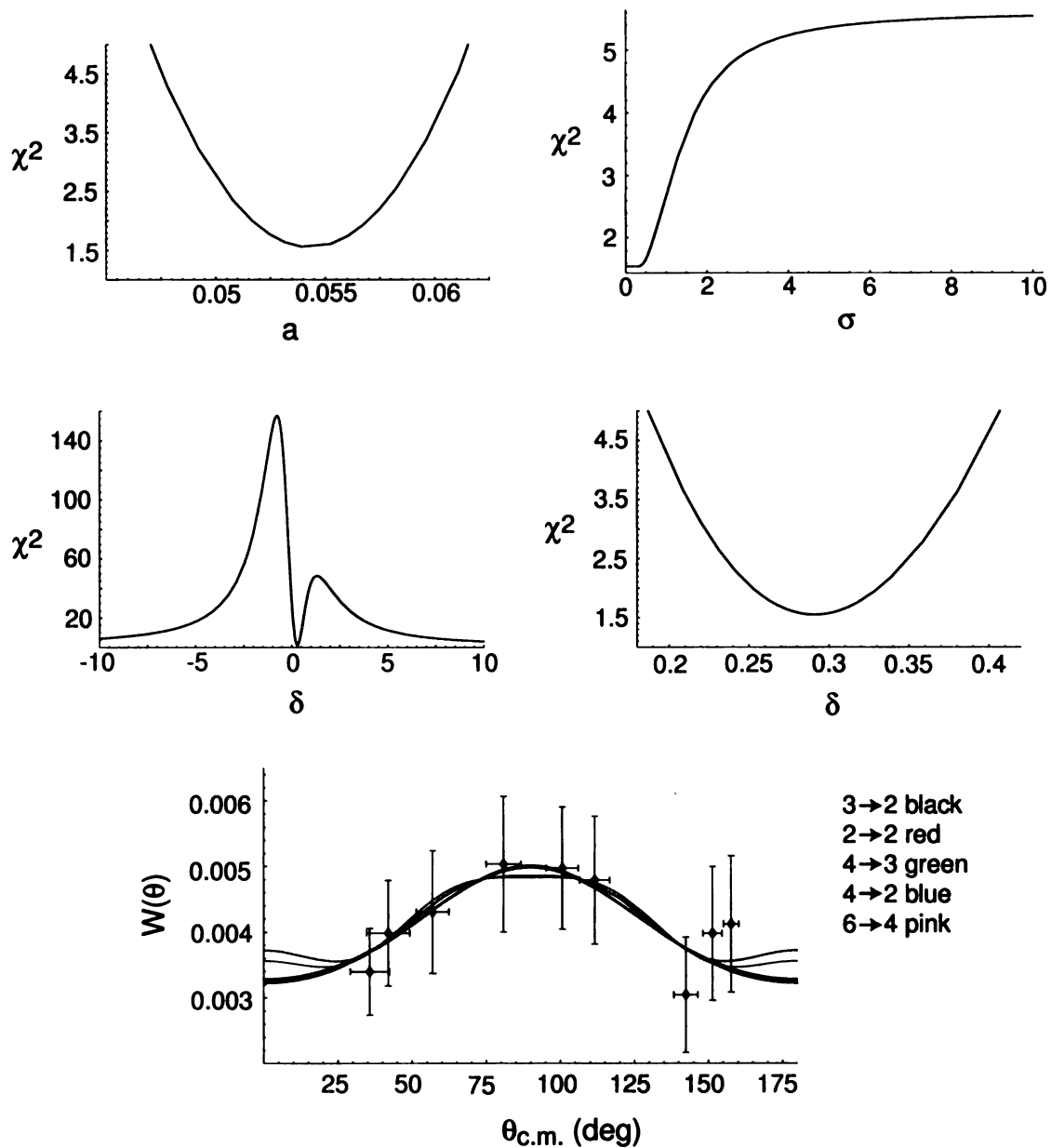
Figure 5.17: Plot of goodness-of-fit χ^2 values versus different parameters for the 2405 keV γ-ray angular distribution $3 \rightarrow 2$ spin transition fit shown together with a plot of the angular distribution versus angle shown in the bottom row. In the 2405 keV γ-ray angular distribution versus angle plot, the points are the data and the lines are the different spin transition fits as described in the text and Table 5.3.

Table 5.4: Ranges of the uncertainties $\Delta W(\theta)/W(\theta)$ on the experimental γ-ray angular distribution points, of the nine SeGA detector angle pairs. (The two γ rays comprising the doublet are not listed.) The detectors at forward angles have the smaller uncertainties because they have more statistics due to relativistic kinematics.

E_γ	$\Delta W(\theta)/W(\theta)$
885	9-10%
1800	34-66%
1964	14-20%
2405	19-29%
2599	14-50%
2912	14-21%
3258	18-30%

If the m substate distribution could be calculated explicitly for each observed excited state and if the error bars on the observed γ-ray angular distributions were smaller, then with only the multipole mixing ratio and an overall scale factor allowed to vary for each γ ray, the fits to the observed γ-ray angular distributions would be able to identify the multipolarities of the γ-ray transitions. For future fragmentation and nucleon-knockout experiments with fast beams, the number of unknowns in the fits to the experimental γ-ray angular distributions must be reduced and the error bars on the intensities must be smaller than the ones in the present experiment. The ranges, over all nine SeGA detector angle pairs, of the uncertainties on the experimental angular distribution points for the observed γ rays (excluding the two γ rays comprising the doublet) are shown in Table 5.4. For all but the 885 keV γ ray, I_i, I_f, a, σ and δ were unknown. Assuming a fit is always done by fixing I_i and I_f and letting a vary, something about σ or δ needs to be known (or assumed) to fit the γ-ray angular distribution and get information about the multipolarity of the γ-ray transition. Even if the error bars were infinitesimally small, σ and δ can not both be free to vary over all possible values for either oblate and prolate alignment. For example, a 3 $\rightarrow$ 2 prolate distribution and a 3 $\rightarrow$ 2 oblate distribution are essentially identical from approximately 20° to 160° with certain values of σ and δ. If the type of alignment is constrained, as was done for the fits to the ^{32}Mg γ-ray angular

distributions, something else still must be known or assumed about either the amount of alignment, σ, or δ (or I_i and I_f). For example, a $3 \rightarrow 2$ prolate distribution and a $4 \rightarrow 2$ prolate distribution are clearly distinguishable if $\delta = 0$, but a value of δ can be found such that the distributions are very similar. If the alignment of either is less than 100%, then the distributions can become nearly identical. This is illustrated in the fit results in Table 5.3 and can be seen in Fig. 5.17. In Chapter 2, only pure transitions of the lowest allowed multipolarity were discussed. In Section 2.5.2 an uncertainty of 4% was quoted as needed to measure γ-ray angular distributions of fragmentation or nucleon-knockout reactions if there is only 20% prolate or oblate alignment and $\beta = 0.4$. That would allow one to tell the difference between a quadrupole and dipole whose relative difference is 10-20%. However, this is not true if the transition is not a pure transition of the lowest possible multipolarity. The actual level of uncertainty needed to make a measurement is then dependent on what is known. Therefore, the type of alignment and some knowledge or plausible assumptions about σ, δ, I_i or I_f must exist to successfully use γ-ray angular distributions with fragmentation and nucleon-knockout reactions at intermediate energies to determine multipolarities of γ-ray transitions.

5.4.4 Partial cross sections

In Table 5.5 the observed ^{32}Mg γ-ray energies and intensities are presented. Table 5.6 lists the excited state energies and partial cross sections. The calculation of the energies of the γ-rays is outlined in Section 5.3.4. To calculate the γ-ray intensities and the partial cross sections the results of the fits of the SeGA angle pair spectra were used and the procedure is as follows. The fitting of the γ-ray spectra for each SeGA angle pair is described in Section 5.3.4. The γ-ray angular distributions were then fit as described in Section 5.4.3 and the results are shown in Table 5.3. For each γ ray,

Table 5.5: ^{32}Mg γ rays observed from the ^{9}Be(^{34}Si,^{32}Mg γ)X reaction. I_i and I_f are the initial and final excited state spins for the levels connected by the respective γ-ray transition with energy, E_γ. The I_γ values are the intensities of the γ-ray transitions relative to an observed ^{32}Mg particle. The column labeled coincidences contains the γ rays that were observed to be in coincidence with the respective E_γ. An energy in brackets denotes that in its γ-γ coincidence spectrum the γ ray with energy E_γ was not observed.

E_γ (keV)	I_i	I_f	I_γ (%)	coincidences[a]
885 ± 4	2$^+$	0$^+$	96.4 ± 3.2	[1414], 1443, 1800, 1964, 2405, 2599, 2912, 3258
1414 ± 7			7.4 ± 1.2	[885]
1443 ± 6			26.1 ± 2.6	885, 2405
1800 ± 10			3.0 ± 0.6	885
1964 ± 9			14.5 ± 1.0	885
2405 ± 11			9.6 ± 0.8	885, 1443
2599 ± 12			9.6 ± 0.8	885
2912 ± 13			13.6 ± 1.0	885, [1414]
3258 ± 16			7.1 ± 0.6	885

[a]For the 1414 and 1443 keV γ rays it was not possible to create separate γ-γ coincidence spectra. Therefore, the γ rays listed as coincidences for these γ rays are those deduced from calculations as described in the text.

the intensity I_γ^{ed}, is

$$I_\gamma^{ed} = \left(\frac{a}{4\pi} \times 10^7 \times \frac{1}{LT_{\text{coinc trig}}} \times \frac{1}{(1-d)} \right) \times \frac{1}{N(^{32}\text{Mg}) \times ds_{\text{S800 trig}} / LT_{\text{S800 trig}}}, \quad (5.4)$$

where 10^7 is the number of γ rays emitted in the GEANT simulation for each γ ray, $LT_{\text{coinc trig}}$ is the coincidence trigger livetime, d is the data loss, $N(^{32}\text{Mg})$ is the number of ^{32}Mg fragments, $LT_{\text{S800 trig}}$ is the S800 particle singles trigger livetime and $ds_{\text{S800 trig}}$ is the S800 particle singles trigger downscale value. (The coincidence trigger livetime and data loss are described in Section 5.3.4. The different livetimes for the different triggers are discussed in Sections 3.5 and 5.2.1.) In Eq. 5.4, for a given E_γ, a is the intensity from the fit of the γ-ray angular distribution where the GEANT scale factor and correction for paralyzed detectors (both described in Section 5.3.4) were taken into account. Those corrections had to be made to the intensities obtained by fitting the SeGA angle pair spectra prior to fitting the γ-

ray angular distributions because they are detector angle dependent. The efficiency of the CRDCs and efficiency of the object scintillator are not included in Eq. 5.4 because they affect the a and $N(^{32}\text{Mg})$ terms equally. There were 179 good runs (approximately 88 hours) in the $^9\text{Be}(^{34}\text{Si},^{32}\text{Mg }\gamma)\text{X}$ dataset. The entire dataset was used when fitting the γ-ray spectrum for each SeGA detector angle pair. However, different trigger downscale values were used for some runs. This was addressed as follows. A subset of 108 runs (approximately 54 hours) with one trigger setting (and set of downscale values) was used to accurately obtain the intensity for just the 885 keV γ ray. The intensity of the 885 keV γ ray from the subset of runs, I_{885}, was then taken as an absolute reference for the other intensities. The coincidence trigger livetime and data loss values listed in Table 5.1 are the values from this subset of runs and are used in the calculation of I_{885}. For the subset of runs the number of ^{32}Mg fragments, corrected for the S800 particle singles trigger livetime and downscale factor, was $N(^{32}\text{Mg}) \times ds_{\text{S800 trig}}/LT_{\text{S800 trig}} = 347108 \pm 2266$. The livetime of the S800 particle singles trigger, $LT_{\text{S800 trig}}$, was approximately 68%. Therefore, for each γ ray the absolute intensity I_γ given in Table 5.5 is

$$I_\gamma = I_\gamma^{ed} \times \frac{I_{885}}{I_{885}^{ed}} \tag{5.5}$$

Calculating partial cross sections from the γ-ray intensities was possible once a level scheme was constructed. The level scheme was constructed using the observed γ-ray intensities and γ-γ coincidence analysis as discussed in Section 5.4.2. For an excited state that was not fed by higher-lying γ rays, the partial cross section was calculated from the intensity of the γ ray which decays from that state by multiplying the intensity by the inclusive cross section. For an excited state fed by higher lying γ rays, the intensities of the feeding γ rays were subtracted from the intensity of the γ ray from the excited state whose partial cross section is being calculated. The value is then multiplied by the inclusive cross section to get the partial cross section. For the

Table 5.6: Level energies E and partial cross sections in ^{32}Mg corresponding to the level scheme shown.

E (keV)	Partial cross section (mb)
0.0	-0.019 ± 0.030^a
885 ± 4	0.080 ± 0.043^a
2299 ± 8	0.063 ± 0.012
2328 ± 8	0.142 ± 0.027
2685 ± 11	0.026 ± 0.005
2849 ± 10	0.124 ± 0.014
3484 ± 13	0.083 ± 0.011
3797 ± 14	0.117 ± 0.014
4143 ± 16	0.061 ± 0.008
4733 ± 13	0.083 ± 0.011
	Sum $= 0.760 \pm 0.066$

^{a}Includes feeding from γ-ray strength from 3400-4924 keV.

^{9}Be(^{34}Si,^{32}Mg γ)X reaction, the partial cross sections were calculated according to the level scheme shown in Fig. 5.13; the intensities of all the γ rays that are shown to feed the 885 keV level, for example, were subtracted from the 885 keV γ-ray intensity when calculating the partial cross section for the 885 keV level. The partial cross sections are presented in Table 5.6.

Some excess γ-ray strength above 3400 keV that could feed the 885 keV γ ray was quantified. γ rays above 4924 keV cannot feed the 885 keV level because $S_n = 5809$ keV. A 3400-4924 keV gated, γ-γ coincidence spectrum showed the 885 keV γ ray. In the ^{32}Mg γ-ray summed spectrum of all SeGA detectors it is not clear how many peaks are between 3400 and 4924 keV. Regardless of whether one or two peaks were assumed from 3400-4924 keV, using GEANT and the γ-γ coincidence spectrum a cross section for the γ ray(s) strength between 3400 and 4924 keV was estimated to be (0.05 ± 0.01) mb. Therefore, assuming feeding from above 3400 keV, the partial cross section of the 885 keV level is (0.080 ± 0.043) mb and the partial cross section of the ground state is (-0.019 ± 0.030) mb. If the 1414 keV γ ray is not in coincidence with the 885 keV γ ray, the partial cross section of the 885 keV level, including the feeding from above 3400 keV, would be (0.143 ± 0.044) mb.

Discussion

The 885 keV first 2^+ level is well established from previous experiments and its structure has been interpreted as being a $2\hbar\omega$ excitation. (See [46] and other references in Section 1.4.1.) In the reaction $^9\text{Be}(^{34}\text{Si},^{32}\text{Mg } \gamma)\text{X}$, two protons are removed from the $\pi d_{5/2}$ orbital in the ground state of ^{34}Si which is dominated by the $0\hbar\omega$ configuration [95]. Therefore, due to a very small overlap between these two configurations, little direct feeding is expected in this reaction to the 2^+ 885 keV level in ^{32}Mg. Within 2σ, the observed partial cross section of the 885 keV level of (0.080 ± 0.043) mb is consistent with no direct feeding to the 885 keV level. The partial cross section of the ground state of (-0.019 ± 0.030) mb is also consistent with no direct feeding to the ground state. This is expected because, like the 2^+ state, the ground state is dominated by a $2\hbar\omega$ configuration. If the 1414 keV γ ray was not in coincidence with the 885 keV γ ray, the partial cross section of (0.143 ± 0.044) mb for the 885 keV level would imply that the 885 keV level is not a $2\hbar\omega$ configuration, but has some small $0\hbar\omega$ admixture.

The 885 keV γ-ray angular distribution is shown in Fig. 5.18. The 885 keV γ ray is the lowest excited state and is fed by at least eight observed γ rays and appears to have little or no direct feeding. Therefore, one would expect its γ-ray angular distribution to be isotropic. The fit of the γ-ray angular distribution, as can be seen in Table 5.3, is consistent with an isotropic distribution.

The (1443 ± 6) keV γ ray agrees in energy with the (1437.0 ± 0.3) keV [34] γ ray observed in β decay. Within 2σ, the (1414 ± 7) keV γ ray agrees in energy with the (1438 ± 12) keV γ ray seen in intermediate-energy Coulomb excitation [4]. If the β decay and intermediate-energy Coulomb excitation experiments observed two different γ rays near 1430 keV as suggested here, then there is no contradiction in possible J^π values for their initial states. (The possible J^π values are discussed in Section 1.4.1 and below.)

Two recent experiments give contradictory information on whether the 1414 keV
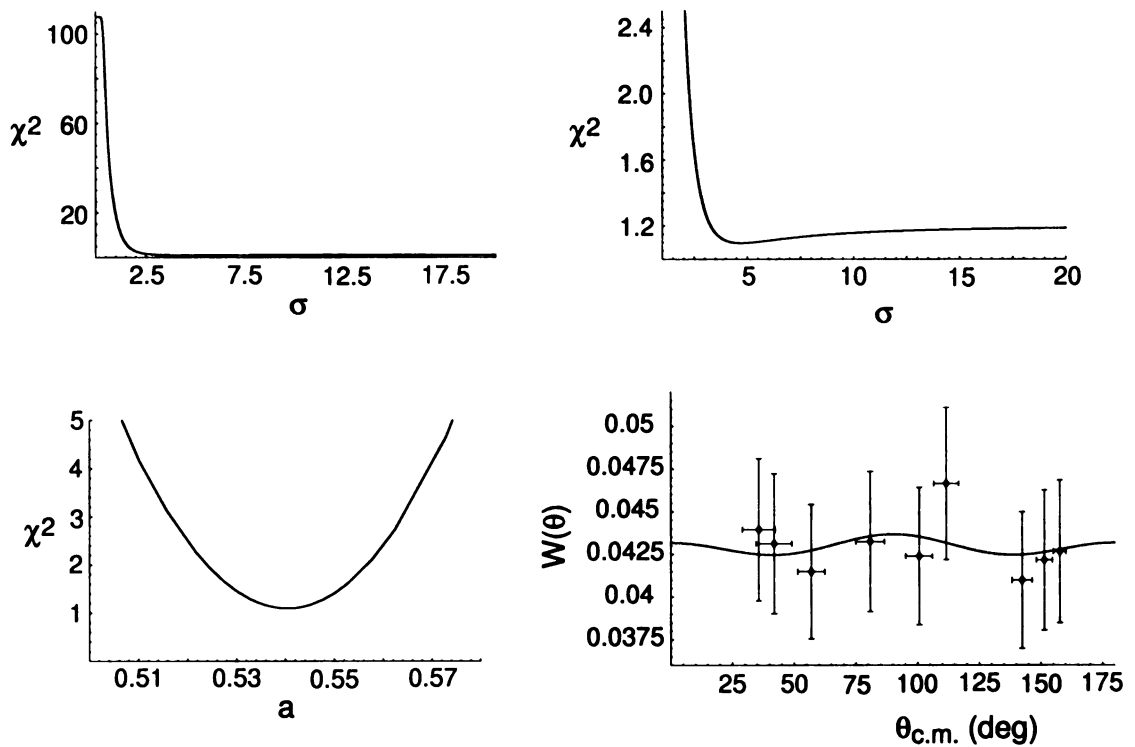
Figure 5.18: Plots of goodness-of-fit χ^2 values versus different parameters for the 885 keV γ-ray angular distribution $2 \rightarrow 0$ spin transition fit shown together with a plot of the angular distribution versus angle shown in the bottom row. The points are the data and the line is the $2 \rightarrow 0$ spin transition fit as described in the text and Table 5.3.

γ ray and 885 keV γ ray are in coincidence. The two published measured ^{32}Mg B(E2↑) values of 454(78) e^2fm^4 [10] and 333(70) e^2fm^4 [4] are different because the latter takes into account feeding into the 885 keV level from an observed γ ray around 1430 keV. Without the feeding correction, the B(E2↑) value in [4] is equal to 440(55) e^2fm^4 [4] which agrees well with [10] which has no feeding correction. A recent livetime measurement [100] measures a half-life with corresponds to a B(E2↑) value of 327(87) e^2fm^4. This value best agrees with the feeding corrected B(E2↑) value. However, another recent Coulomb excitation measurement at low energy [101] reports a preliminary B(E2↑) value of 434(52) e^2fm^4.

Assuming that the 1414 keV γ ray is the γ ray observed in the intermediate-energy Coulomb excitation experiment and that the 1414 keV and 885 keV γ rays are in coincidence, from [4] the possible J^π values of the 2299 keV state are 1^-, 1^+ or 2^+. If the 1414 keV γ ray decays directly to the ground state from a level at 1414 keV and it was observed in intermediate-energy Coulomb excitation, possible J^π values are 1^-, 1^+ or 2_2^+ because $\lambda = 1$ and $\lambda = 2$ excitations are the most probable in Coulomb excitation.

The (1964 ± 9) keV γ ray agrees in energy and level scheme placement with the (1972.9±0.5) keV γ ray observed in β decay [34]. Because the 1443 keV and 1964 keV γ rays agree in energy with the γ rays seen in β decay, it is concluded that the excited state levels, (2327.9 ± 7.5) keV and (2848.9 ± 9.7) keV are the same levels as the (2322.3 ± 0.3) keV and (2858.2 ± 0.5) keV levels, respectively, seen in the β-decay measurement [34]. The 2328 keV and 2849 keV levels have the largest partial cross sections, (0.142 ± 0.027) mb and (0.124 ± 0.014) mb respectively, and thus are the most strongly fed levels observed in the two-proton knockout reaction. The β-decay experiment of [47] reported a log ft value of 5.4 for the β-decay transition to the 2321 keV level and a log ft value of 5.1 for the β-decay transition to the 2858 keV level.

Generally, log ft values corresponding to allowed β-decay transitions range from

2.9-10 and log *ft* values corresponding to first forbidden transitions range from 5-19 [102]. In the mass region around ^{32}Mg, log *ft* values of 5.1 and 5.4 seem to correspond to allowed β-decay transitions. From a compilation of log *ft* values for nuclei with Z < 80, a lower limit of log *ft* = 5.9 for first forbidden transitions can be suggested [103]. In [103] eight exceptions are reported where the log *ft* values are in the range of 5.5 to 5.7; these are from decays of ^{96}Y, ^{142}Cs, ^{143}Cs, ^{150}Ho, ^{158}Er, ^{162}Yb and ^{163}Yb. The ground state of ^{32}Na is thought to be negative parity from shell-model calculations [12] and the β decay in [47] finds a negative-parity ground state for ^{32}Na more plausible than a positive-parity ground state. Shell-model calculations in [15] present configurations for the ground state of ^{32}Na to be positive parity or negative parity, but say that a negative parity ground state is consistent with β-decay results [46]. Assuming the ^{32}Na ground state is negative parity and the log *ft* values correspond to allowed transitions, then the 2849 keV level and the 2328 keV level must each have $J^{\pi} \leq 5^{-}$. This contradicts the simple picture of the two-proton knockout reaction ^{9}Be(^{34}Si,^{32}Mg γ)X which cannot explain the strong population of negative parity levels; direct removal of two $d_{5/2}$ protons does not yield negative parity excited states.

Some possibilities as to what might be occurring are presented. The first is that the two negative-parity levels are not directly fed in the two-proton knockout reaction, but are fed by higher-lying γ rays. In the ^{32}Mg γ-ray energy spectrum containing the sum of all the detectors, when fit with nine simulated response functions plus an exponential background, there is a small excess of counts around 2300 and 2700 keV corresponding to a partial cross section of (0.055 ± 0.008) mb. This excess of counts is too small to account for the two very strong γ rays at 1443 keV and 1964 keV. The second possibility is that the ground state of ^{32}Na is not negative parity as expected, but is positive parity. The *possibility* of a positive-parity ground state of ^{32}Na is supported by shell model calculations [15, 19], but is very dependent on the magnitude of the N=20 shell gap. If the ground state of ^{32}Na is positive parity then

the 2328 keV and 2849 keV levels would be positive parity and strongly populating positive parity states are what would be expected. The third possibility is if in the β-decay experiment some γ-ray strength was missed due to feeding from unobserved higher-lying γ rays in ^{32}Mg, the β branch intensities would change and small changes in the intensities have large impacts on the log ft values. If a small amount of γ-ray strength in ^{32}Mg feeding the 2328 keV and 2849 keV levels was not observed, the log ft values would increase and correspond to first forbidden transitions. If the ground state of ^{32}Na is assumed to be negative parity, then first forbidden transitions would make the 2328 keV and 2849 keV levels have positive parity. A fourth possibility is that the log ft values of 5.4 and 5.1 for the β-decay transitions to the 2321 keV and 2858 keV levels, respectively, correspond to first forbidden transitions. First forbidden transitions may be enhanced in the neutron-rich region around ^{32}Mg. Two examples of first forbidden transitions in this mass region, with relatively small log ft values are a β decay from the 4^- ground state of ^{34}Al to a 2^+ state in ^{34}Si with a log $ft > 5.5$ [104] and a β decay from the negative parity ground state of ^{38}P to a 2^+ state in ^{38}S with a log $ft = 5.9 \pm 0.2$ [105]. Lastly, a more remote possibility for the strong population of the 2328 keV and 2849 keV levels, assuming they are negative parity, is that many higher-energy, positive-parity states are weakly populated resulting in a shower of weak, unobserved γ rays feeding the 2328 keV and 2849 keV levels. These unobserved γ rays must be very weak and contribute only to the exponential background because they are not seen in the observed γ-ray spectrum.

Chapter 6

Summary

The feasibility of using γ-ray angular distributions and γ-γ angular correlations with intermediate-energy beams was explored theoretically. The angular distribution of 1460 keV $2^+ \rightarrow 0_{g.s.}^+$ γ rays emitted from intermediate-energy Coulomb excited ^{40}Ar was measured. The nucleus, ^{32}Mg was studied in a two-proton knockout reaction from ^{34}Si.

The formalism for γ-ray angular distributions and γ-γ angular correlations with intermediate-energy beams was presented. Measuring angular distributions and angular correlations of γ rays from different reaction mechanisms, including intermediate-energy Coulomb excitation, was discussed. Measuring γ-ray angular distributions and γ-γ angular correlations is feasible with intermediate-energy beams. This was shown for the intermediate-energy Coulomb excitation of ^{40}Ar. The measured angular distribution for the 1460 keV $2^+ \rightarrow 0_{g.s.}^+$ γ ray agrees with the calculated $0 \rightarrow 2 \rightarrow 0$ distribution.

^{32}Mg was studied in the two-proton knockout reaction, ^{9}Be(^{34}Si,^{32}Mg γ)X. Nine γ rays were observed; five were observed for the first time. For seven of the nine γ rays, γ-ray angular distributions were measured. No spin and parity assignments could be made from the distributions due to not knowing the magnitude of the prolate alignment and the relatively large error bars on the experimental points.

A level scheme for ^{32}Mg was constructed using the observed γ-γ coincidence data and γ-ray intensities. In the two-proton knockout reaction, ^{9}Be(^{34}Si,^{32}Mg γ)X, no direct feeding to the ground state of ^{32}Mg was observed and no direct feeding to the first excited 2^+ state at 885 keV was observed within 2σ. This supports that the ground state of ^{34}Si is predominantly $0\hbar\omega$ because the ground and first excited states of ^{32}Mg are known to be deformed, $2\hbar\omega$ configurations. The sd states are each thought to fragment over a few MeV to create the observed excited states. Six excited states were deduced from the observed γ rays which are thought to be from the fragmented sd states. The other two excited states at 2849 keV and 2328 keV appear to have negative parity and different possibilities to their population have been presented.

Two of the observed γ rays were at (1414.0±6.6) keV and (1443.0±6.4) keV. These two γ rays may resolve the possible spin and parity conflicts arisen from previous measurements of what was thought to be one γ ray around 1438 keV.

The observed inclusive cross section for the ^{9}Be(^{34}Si,^{32}Mg)X reaction is (0.86 ± 0.08) mb. Calculations of the two-proton knockout reaction, assuming two correlated protons knocked out of the $d_{5/2}$ shell, predict three pure sd states that are not observed in the present experiment. The predicted inclusive cross section for the ^{9}Be(^{34}Si,^{32}Mg)X reaction is 2.76 mb. Some of the calculated sd strength appears to be lost due to being above the neutron separation energy in agreement with the observation of ^{31}Mg. Thus the predicted cross section more closely reflects the observed inclusive cross section, though a better understanding of the structure of ^{32}Mg is needed to accurately predict the inclusive cross section and observed excited states.

Appendix A

Subroutine used by GEANT

Below is the Fortran subroutine described in Sect. 3.3.3. It takes the x,y,z center-of-mass of each segment of each SeGA detector from the *xml* file used by SpecTcl and generates the x,y,z positions and rotation angles for the geometry of SeGA as needed for GEANT. GEANT requires three theta and three phi angles for each detector as well as a position. The variables used below are thx, phix, thy, phiy, thz, phiz, xx, yy, and zz for each detector.

```fortran
      SUBROUTINE calcrotm(thx,phix,thy,phiy,thz,phiz,xx,yy,zz)


* User common blocks
INCLUDE 'uinc/uoutput.ins'


      INTEGER detnum(18)
      REAL x(18,576), y(18,576), z(18,576)
      REAL Offset/0.8/
      REAL aox/0./, aoy/0./, aoz/0./
      REAL box/0./, boy/1./, boz/0./
      REAL cox/1./, coy/0./, coz/0./
```

118

```
REAL ax(18), ay(18), az(18)

REAL bx(18), by(18), bz(18)

REAL cx(18), cy(18), cz(18)

REAL rot(18,3,3)

REAL thx(18), phix(18), thy(18), phiy(18), thz(18)

REAL phiz(18)

REAL PI/3.14159265359/

REAL det(18,3,3), orig(3,3), detinv(18,3,3)

REAL originv(3,3)

REAL dettrans(18,3,3), rottrans(18,3,3)

REAL origtrans(3,3), origtransinv(3,3)

REAL denom1, denom2, denom1o, denom2o

REAL determ(18), determo, norma(18), normb(18)

REAL normao, normbo, normco, normc(18)

REAL xx(18), yy(18), zz(18)

REAL v1(18,3), v2(18,3), v3(18,3)

REAL v1v2(18), v1v3(18), v2v3(18)

REAL sumx(18), sumy(18), sumz(18)

REAL avgx(18), avgy(18), avgz(18)

REAL sumx12(18), sumy12(18), sumz12(18)

REAL avgx12(18), avgy12(18), avgz12(18)

REAL sumx14(18), sumy14(18), sumz14(18)

REAL avgx14(18), avgy14(18), avgz14(18)

REAL last3x(18), last3y(18), last3z(18)

REAL avglast3x(18), avglast3y(18), avglast3z(18)

REAL distance(18)
```

```
      aoz=-Offset



      DO I=1,18


* Convert the DetPos data to the format used in this subroutine.

* DetPos are the detector positions as read in from the *.xml

* file by a GEANT subroutine that is called previous to this one.


        DO J=1,32
          x(I,J)=DetPos(I,J,1)
          y(I,J)=DetPos(I,J,2)
          z(I,J)=DetPos(I,J,3)
        END DO


* Begin calculations


        DO J=1,32
          sumx(I)=sumx(I)+x(I,J)
          sumy(I)=sumy(I)+y(I,J)
          sumz(I)=sumz(I)+z(I,J)
        END DO
        avgx(I)=sumx(I)/32
        avgy(I)=sumy(I)/32
        avgz(I)=sumz(I)/32


        distance(I)=(avgx(I)**2+avgy(I)**2+avgz(I)**2)**.5
```

```
      sumx12(I)=x(I,1)+x(I,2)+x(I,5)+x(I,6)+x(I,9)+x(I,10)+x(I,13)+
1        x(I,14)+x(I,17)+x(I,18)+x(I,21)+x(I,22)+x(I,25)+x(I,26)+
2        x(I,29)+x(I,30)
   avgx12(I)=sumx12(I)/16


      sumy12(I)=y(I,1)+y(I,2)+y(I,5)+y(I,6)+y(I,9)+y(I,10)+y(I,13)+
1        y(I,14)+y(I,17)+y(I,18)+y(I,21)+y(I,22)+y(I,25)+y(I,26)+
2        y(I,29)+y(I,30)
   avgy12(I)=sumy12(I)/16


      sumz12(I)=z(I,1)+z(I,2)+z(I,5)+z(I,6)+z(I,9)+z(I,10)+z(I,13)+
1        z(I,14)+z(I,17)+z(I,18)+z(I,21)+z(I,22)+z(I,25)+z(I,26)+
2        z(I,29)+z(I,30)
   avgz12(I)=sumz12(I)/16


      sumx14(I)=x(I,1)+x(I,4)+x(I,5)+x(I,8)+x(I,9)+x(I,12)+x(I,13)+
1        x(I,16)+x(I,17)+x(I,20)+x(I,21)+x(I,24)+x(I,25)+x(I,28)+
2        x(I,29)+x(I,32)
   avgx14(I)=sumx14(I)/16


      sumy14(I)=y(I,1)+y(I,4)+y(I,5)+y(I,8)+y(I,9)+y(I,12)+y(I,13)+
1        y(I,16)+y(I,17)+y(I,20)+y(I,21)+y(I,24)+y(I,25)+y(I,28)+
2        y(I,29)+y(I,32)
   avgy14(I)=sumy14(I)/16


      sumz14(I)=z(I,1)+z(I,4)+z(I,5)+z(I,8)+z(I,9)+z(I,12)+z(I,13)+
1        z(I,16)+z(I,17)+z(I,20)+z(I,21)+z(I,24)+z(I,25)+z(I,28)+
2        z(I,29)+z(I,32)
```

```
avgz14(I)=sumz14(I)/16


DO J=21,32
   last3x(I)=last3x(I)+x(I,J)

   last3y(I)=last3y(I)+y(I,J)

   last3z(I)=last3z(I)+z(I,J)
END DO
avglast3x(I)=last3x(I)/12

avglast3y(I)=last3y(I)/12

avglast3z(I)=last3z(I)/12


ax(I)=-(avglast3x(I)-avgx(I))

ay(I)=-(avglast3y(I)-avgy(I))

az(I)=-(avglast3z(I)-avgz(I))


bx(I)=avgx12(I)-avgx(I)

by(I)=avgy12(I)-avgy(I)

bz(I)=avgz12(I)-avgz(I)


cx(I)=avgx14(I)-avgx(I)

cy(I)=avgy14(I)-avgy(I)

cz(I)=avgz14(I)-avgz(I)


norma(I)=SQRT(ax(I)**2+ay(I)**2+az(I)**2)

normb(I)=SQRT(bx(I)**2+by(I)**2+bz(I)**2)

normc(I)=SQRT(cx(I)**2+cy(I)**2+cz(I)**2)

normao=SQRT(aox**2+aoy**2+aoz**2)

normbo=SQRT(box**2+boy**2+boz**2)
```

```
      normco=SQRT(cox**2+coy**2+coz**2)


      det(I,1,1)=ax(I)/norma(I)

      det(I,1,2)=ay(I)/norma(I)

      det(I,1,3)=az(I)/norma(I)

      det(I,2,1)=bx(I)/normb(I)

      det(I,2,2)=by(I)/normb(I)

      det(I,2,3)=bz(I)/normb(I)

      det(I,3,1)=cx(I)/normc(I)

      det(I,3,2)=cy(I)/normc(I)

      det(I,3,3)=cz(I)/normc(I)


*     Printing to screen the dot products of the det vectors
*     They should all be zero if orthonormal


      PRINT *, det(I,1,1)*det(I,2,1)+det(I,1,2)*det(I,2,2)+
1        det(I,1,3)*det(I,2,3), det(I,1,1)*det(I,3,1)+
2        det(I,1,2)*det(I,3,2)+det(I,1,3)*det(I,3,3),
3        det(I,3,1)*det(I,2,1)+det(I,3,2)*det(I,2,2)+
4        det(I,3,3)*det(I,2,3)


      orig(1,1)=aox/normao

      orig(1,2)=aoy/normao

      orig(1,3)=aoz/normao

      orig(2,1)=box/normbo

      orig(2,2)=boy/normbo

      orig(2,3)=boz/normbo

      orig(3,1)=cox/normco
```

```fortran
      orig(3,2)=coy/normco
      orig(3,3)=coz/normco


  END DO


  DO I=1,18
     DO J=1,3
        DO K=1,3
           dettrans(I,J,K)=det(I,K,J)
        END DO
     END DO
  END DO


  DO I=1,3
     DO J=1,3
           origtrans(I,J)=orig(J,I)
     END DO
  END DO


  DO I=1,18
     denom1=det(I,1,3)*det(I,2,2)*det(I,3,1)-
1         det(I,1,2)*det(I,2,3)*det(I,3,1)-
2         det(I,1,3)*det(I,2,1)*det(I,3,2)+
3         det(I,1,1)*det(I,2,3)*det(I,3,2)+
4         det(I,1,2)*det(I,2,1)*det(I,3,3)-
5         det(I,1,1)*det(I,2,2)*det(I,3,3)
     denom2=-det(I,1,3)*det(I,2,2)*det(I,3,1)+
1         det(I,1,2)*det(I,2,3)*det(I,3,1)+
```

```
2         det(I,1,3)*det(I,2,1)*det(I,3,2)-
3         det(I,1,1)*det(I,2,3)*det(I,3,2)-
4         det(I,1,2)*det(I,2,1)*det(I,3,3)+
5         det(I,1,1)*det(I,2,2)*det(I,3,3)
      detinv(I,1,1)=(det(I,2,3)*det(I,3,2)-det(I,2,2)*det(I,3,3))/
1         denom1
      detinv(I,1,2)=(det(I,1,3)*det(I,3,2)-det(I,1,2)*det(I,3,3))/
1         denom2
      detinv(I,1,3)=(det(I,1,3)*det(I,2,2)-det(I,1,2)*det(I,2,3))/
1         denom1
      detinv(I,2,1)=(det(I,2,3)*det(I,3,1)-det(I,2,1)*det(I,3,3))/
1         denom2
      detinv(I,2,2)=(det(I,1,3)*det(I,3,1)-det(I,1,1)*det(I,3,3))/
1         denom1
      detinv(I,2,3)=(det(I,1,3)*det(I,2,1)-det(I,1,1)*det(I,2,3))/
1         denom2
      detinv(I,3,1)=(det(I,2,2)*det(I,3,1)-det(I,2,1)*det(I,3,2))/
1         denom1
      detinv(I,3,2)=(det(I,1,2)*det(I,3,1)-det(I,1,1)*det(I,3,2))/
1         denom2
      detinv(I,3,3)=(det(I,1,2)*det(I,2,1)-det(I,1,1)*det(I,2,2))/
1         denom1


*    The determinant should be 1 if the normalized vector lengths
*    are conserved.


      determ(I)=denom2
```

125

```fortran
      END DO


      denom1o=orig(1,3)*orig(2,2)*orig(3,1)-
     1      orig(1,2)*orig(2,3)*orig(3,1)-
     2      orig(1,3)*orig(2,1)*orig(3,2)+
     3      orig(1,1)*orig(2,3)*orig(3,2)+
     4      orig(1,2)*orig(2,1)*orig(3,3)-
     5      orig(1,1)*orig(2,2)*orig(3,3)
      denom2o=-orig(1,3)*orig(2,2)*orig(3,1)+
     1      orig(1,2)*orig(2,3)*orig(3,1)+
     2      orig(1,3)*orig(2,1)*orig(3,2)-
     3      orig(1,1)*orig(2,3)*orig(3,2)-
     4      orig(1,2)*orig(2,1)*orig(3,3)+
     5      orig(1,1)*orig(2,2)*orig(3,3)
      originv(1,1)=(orig(2,3)*orig(3,2)-orig(2,2)*orig(3,3))/denom1o
      originv(1,2)=(orig(1,3)*orig(3,2)-orig(1,2)*orig(3,3))/denom2o
      originv(1,3)=(orig(1,3)*orig(2,2)-orig(1,2)*orig(2,3))/denom1o
      originv(2,1)=(orig(2,3)*orig(3,1)-orig(2,1)*orig(3,3))/denom2o
      originv(2,2)=(orig(1,3)*orig(3,1)-orig(1,1)*orig(3,3))/denom1o
      originv(2,3)=(orig(1,3)*orig(2,1)-orig(1,1)*orig(2,3))/denom2o
      originv(3,1)=(orig(2,2)*orig(3,1)-orig(2,1)*orig(3,2))/denom1o
      originv(3,2)=(orig(1,2)*orig(3,1)-orig(1,1)*orig(3,2))/denom2o
      originv(3,3)=(orig(1,2)*orig(2,1)-orig(1,1)*orig(2,2))/denom1o


      denom1o=origtrans(1,3)*origtrans(2,2)*origtrans(3,1)-
     1      origtrans(1,2)*origtrans(2,3)*origtrans(3,1)-
     2      origtrans(1,3)*origtrans(2,1)*origtrans(3,2)+
     3      origtrans(1,1)*origtrans(2,3)*origtrans(3,2)+
```

```
4       origtrans(1,2)*origtrans(2,1)*origtrans(3,3)-
5       origtrans(1,1)*origtrans(2,2)*origtrans(3,3)
 denom2o=-origtrans(1,3)*origtrans(2,2)*origtrans(3,1)+
1       origtrans(1,2)*origtrans(2,3)*origtrans(3,1)+
2       origtrans(1,3)*origtrans(2,1)*origtrans(3,2)-
3       origtrans(1,1)*origtrans(2,3)*origtrans(3,2)-
4       origtrans(1,2)*origtrans(2,1)*origtrans(3,3)+
5       origtrans(1,1)*origtrans(2,2)*origtrans(3,3)
 origtransinv(1,1)=(origtrans(2,3)*origtrans(3,2)-origtrans(2,2)*
1       origtrans(3,3))/denom1o
 origtransinv(1,2)=(origtrans(1,3)*origtrans(3,2)-origtrans(1,2)*
1       origtrans(3,3))/denom2o
 origtransinv(1,3)=(origtrans(1,3)*origtrans(2,2)-origtrans(1,2)*
1       origtrans(2,3))/denom1o
 origtransinv(2,1)=(origtrans(2,3)*origtrans(3,1)-origtrans(2,1)*
1       origtrans(3,3))/denom2o
 origtransinv(2,2)=(origtrans(1,3)*origtrans(3,1)-origtrans(1,1)*
1       origtrans(3,3))/denom1o
 origtransinv(2,3)=(origtrans(1,3)*origtrans(2,1)-origtrans(1,1)*
1       origtrans(2,3))/denom2o
 origtransinv(3,1)=(origtrans(2,2)*origtrans(3,1)-origtrans(2,1)*
1       origtrans(3,2))/denom1o
 origtransinv(3,2)=(origtrans(1,2)*origtrans(3,1)-origtrans(1,1)*
1       origtrans(3,2))/denom2o
 origtransinv(3,3)=(origtrans(1,2)*origtrans(2,1)-origtrans(1,1)*
1       origtrans(2,2))/denom1o


*       The determinant should be 1 if the normalized vector lengths
```

```fortran
*     are conserved.


      determo=denom2o


      DO I=1,18
         DO J=1,3
            DO K=1,3


               rot(I,J,K)=0.0
               DO L=1,3
                  rot(I,J,K)=rot(I,J,K)+dettrans(I,J,L)*
1                    origtransinv(L,K)
               END DO


            END DO
         END DO
      END DO


*     Fixing rounding problems


      DO I=1,18
         DO J=1,3
            DO K=1,3
               IF ((rot(I,J,K).GT.1.0).OR.(rot(I,J,K).LT.-1)) THEN
                  IF (rot(I,J,K).GT.1.0) THEN
                     rot(I,J,K)=1.0
                  END IF
                  IF (rot(I,J,K).LT.-1) THEN
```

```
                    rot(I,J,K)=-1.0

                END IF

            END IF

        END DO

    END DO

END DO


*    The GEANT angles, (thx, thy, thz, phix, phiy, phiz), are

*    calculated from rottrans(I,J,K)


DO I=1,18

    DO J=1,3

        DO K=1,3

            rottrans(I,J,K)=rot(I,K,J)

        END DO

    END DO

END DO


DO I=1,18


    thx(I)=ACOS(rottrans(I,1,3))*180.0/PI

    thy(I)=ACOS(rottrans(I,2,3))*180.0/PI

    thz(I)=ACOS(rottrans(I,3,3))*180.0/PI


    IF (rottrans(I,1,1).GT.0.0) THEN

        phix(I)=ATAN(rottrans(I,1,2)/rottrans(I,1,1))*180.0/PI

    ELSE

        IF (rottrans(I,1,1).LT.0.0) THEN
```

```
            phix(I)=ATAN(rottrans(I,1,2)/rottrans(I,1,1))*180.0/PI+
1            180.0
        ELSE
            IF (rottrans(I,1,1).EQ.0.0) THEN
                phix(I)=90.0
            END IF
        END IF
    END IF


    IF (rottrans(I,2,1).GT.0.0) THEN
        phiy(I)=ATAN(rottrans(I,2,2)/rottrans(I,2,1))*180.0/PI
    ELSE
        IF (rottrans(I,2,1).LT.0.0) THEN
            phiy(I)=ATAN(rottrans(I,2,2)/rottrans(I,2,1))*180.0/PI+
1            180.0
        ELSE
            IF (rottrans(I,2,1).EQ.0.0) THEN
                phiy(I)=90.0
            END IF
        END IF
    END IF


    IF (rottrans(I,3,1).GT.0.0) THEN
        phiz(I)=ATAN(rottrans(I,3,2)/rottrans(I,3,1))*180.0/PI
    ELSE
        IF (rottrans(I,3,1).LT.0.0) THEN
            phiz(I)=ATAN(rottrans(I,3,2)/rottrans(I,3,1))*180.0/PI+
1            180.0
```

```
        ELSE
          IF (rottrans(I,3,1).EQ.0.0) THEN
            phiz(I)=90.0
          END IF
        END IF
      END IF



*    The below IF statements are so the final angles are all positive
*    (GEANT requires positive angles)


      IF (thx(I).LT.0.) THEN
        thx(I)=thx(I)+360.0
      END IF
      IF (thy(I).LT.0.) THEN
        thy(I)=thy(I)+360.0
      END IF
      IF (thz(I).LT.0.) THEN
        thz(I)=thz(I)+360.0
      END IF
      IF (phix(I).LT.0.) THEN
        phix(I)=phix(I)+360.0
      END IF
      IF (phiy(I).LT.0.) THEN
        phiy(I)=phiy(I)+360.0
      END IF
      IF (phiz(I).LT.0.) THEN
        phiz(I)=phiz(I)+360.0
```

```
      END IF


      END DO


*     Calculate if the rotation matrix GEANT creates from

*     the above calculated angles is orthonormal - all

*     the dot products should be zero


      DO I=1,18
            v1(I,1)=SIN(thx(I)*PI/180)*COS(phix(I)*PI/180)

            v1(I,2)=SIN(thx(I)*PI/180)*SIN(phix(I)*PI/180)

            v1(I,3)=COS(thx(I)*PI/180)

            v2(I,1)=SIN(thy(I)*PI/180)*COS(phiy(I)*PI/180)

            v2(I,2)=SIN(thy(I)*PI/180)*SIN(phiy(I)*PI/180)

            v2(I,3)=COS(thy(I)*PI/180)

            v3(I,1)=SIN(thz(I)*PI/180)*COS(phiz(I)*PI/180)

            v3(I,2)=SIN(thz(I)*PI/180)*SIN(phiz(I)*PI/180)

            v3(I,3)=COS(thz(I)*PI/180)

            v1v2(I)=v1(I,1)*v2(I,1)+v1(I,2)*v2(I,2)+v1(I,3)*v2(I,3)

            v1v3(I)=v1(I,1)*v3(I,1)+v1(I,2)*v3(I,2)+v1(I,3)*v3(I,3)

            v2v3(I)=v2(I,1)*v3(I,1)+v2(I,2)*v3(I,2)+v2(I,3)*v3(I,3)

            PRINT *, 'v1v2, v1v3, v2v3', I, v1v2(I), v1v3(I),
1                 v2v3(I)
      END DO


*     Calculating the x,y,z of the center of the

*     detector (NOT the crystal) as required by

*     GEANT. The coordinates are (xx,yy,zz).
```

```fortran
      DO I=1,18

          xx(I)=avgx(I)+Offset*SIN(thz(I)*PI/180)*COS(phiz(I)*
1             PI/180)
          yy(I)=avgy(I)+Offset*SIN(thz(I)*PI/180)*SIN(phiz(I)*
1             PI/180)
          zz(I)=avgz(I)+Offset*COS(thz(I)*PI/180)


*     This assignment below gives the center of the crystal (it is
*     not used)
*         xx(I)=avgx(I)
*         yy(I)=avgy(I)
*         zz(I)=avgz(I)


      END DO


*     Output to file
      DO I=1,18
          WRITE(3,*) 'Detector number: ', detnum(I)
          WRITE(3,*) '**********'
          WRITE(3,*) 'thx, phix, thy, phiy, thz, phiz '
          WRITE(3,*) thx(I), phix(I), thy(I), phiy(I), thz(I), phiz(I)
          WRITE(3,*) '**********'
          WRITE(3,*) 'x, y, z '
          WRITE(3,*) xx(I), yy(I), zz(I)
          WRITE(3,*) '**********'
      END DO
```

```
      CLOSE(3)


***    Output to screen  ***


      DO I=1,18
         PRINT *, 'Distance(I) for I=1,18', distance(I)
      END DO


*     DO I=1,18
*        PRINT *, '*****************************************'
*        PRINT *, 'avgx, avgy, avgz', avgx(I), avgy(I), avgz(I)
*        PRINT *, 'xx, yy, zz', xx(I), yy(I), zz(I)
*     END DO


      PRINT *, 'End of subroutine. '


      RETURN


      END
```

Appendix B

GEANT input file

Below is a sample GEANT input file, described in Sect. 3.3.6. For each simulation performed this file is called. The values used for the parameters (the number(s) between the <value> and </value> tags) are taken from experimental observables.

```xml
<?xml version="1.0"?>
<?xml-stylesheet href="segasim.css" type="text/css"?>
<!DOCTYPE segasim SYSTEM "segasim.dtd">


<segasim>
<header>
    <filename>segasim0509061902.xml</filename>
    <creationdate>
        <year>2005</year>
        <month>09</month>
        <day>06</day>
        <hour>19</hour>
<minute>02</minute>
    </creationdate>
```

```
<creator>Heather Zwahlen</creator>

<creatorversion>1.0</creatorversion>

<comment></comment>
</header>


<variable>

<description>Random number seeds (2 values).</description>

<geantname>RNDM</geantname>

<extendeddescription>
Two random number seeds should be defined.

</extendeddescription>

<value>2342307421 4572456119</value>
</variable>


<variable>

<description>Version of GEANT code</description>

<geantname>VERSION</geantname>

<extendeddescription>
This is the version of the SeGA GEANT code that
will be used for this simulation.

</extendeddescription>

<value>2</value>
</variable>


<variable>

<description>Filename for SeGA segment position</description>

<geantname>SEGPOS</geantname>

<extendeddescription>
```

The valid angle files should have a .xml or .ang extenstion.

```
    </extendeddescription>

    <value>segang041105.xml</value>

</variable>


<variable>

    <description>Run mode for GEANT</description>

    <geantname>MODE</geantname>

    <extendeddescription>
i -- interactive mode
b -- batch mode
    </extendeddescription>

    <value>b</value>

</variable>


<variable>

    <description>Number of events to emit</description>

    <geantname>TRIG</geantname>

    <extendeddescription>
This key only works for batch mode.
    </extendeddescription>

    <value>10000000</value>

</variable>


<variable>

    <description>Show events tracks in display window.</description>

    <geantname>SHTRACKS</geantname>

    <extendeddescription>
```

If =1, show event tracks. This is useful only in

interactive mode.

        `</extendeddescription>`

        `<value>0</value>`

`</variable>`

`<variable>`

        `<description>Detector setup option (2 values).</description>`

        `<geantname>SETOPT</geantname>`

        `<extendeddescription>`

v1=0 v2= : Very simple cylinder of Ge (For testing only)

v1=1 v2=0: 1 SeGA det, source is at DISTANCE from front.

v1=1 v2=1: 1 SeGA det, source is at DISTANCE from side.

ROTATE spins detector around cylindrical

axis

v1=1 v2=2: 2 SeGA dets at DISTANCE from source in middle

v1=1 v2=3: 1 ring of 7 SeGA dets. (DISTANCE adjusts radius)

v1=1 v2=4: 2 rings of 7 SeGA dets. (DISTANCE adjusts radius)

v1=1 v2=5: 1 ring of 4 SeGA dets. (DISTANCE adjusts radius)

v1=1 v2=6: 1 ring of 6 SeGA dets at DISTANCE from source,

and steel plate at the end of detectors (ANL setup)

v1=1 v2=7: 18 detector SeGA array (fixed configuration)

v1=1 v2=8: 18 detector SeGA array in configuration

specified by the SEGPOS filename

        `</extendeddescription>`

        `<value>1 8</value>`

`</variable>`

```
<variable>

    <description>Detector availability

    array (18 values).</description>

    <geantname>USE</geantname>

    <extendeddescription>

These flags are only valid for SETOPT:(1,7) and (1,8).

For SETOPT (1,7),

values 1-8 are positions:  FB000, FB045, FB090, . . ., FB315

values 9-18 are positions: FA000, FA036, FA072, . . ., FA324

For SETOPT (1,8), (numbering 1-6, 9-14, 17-22):

1, 17 ~24deg; 9, 14 ~29deg; 2, 22 ~40deg; 6, 18 ~60deg;

10, 13 ~78deg; 3, 21 ~90deg; 11, 12 ~126deg;  19, 5 ~139deg;

20, 4 ~147deg;

The flag definitions are as follows:

0: Remove detector

1: Detector present but not operational

2: Detector present and operational

    </extendeddescription>

    <value>2 2 2 2 2  2 2 2 2 2  2 2 2 2 2 2 </value>

</variable>


<variable>

    <description>Beam pipe size (2 elements)</description>

    <geantname>PIPSIZ</geantname>

    <extendeddescription>

Element 1: Inner radius (in cm)

Element 2: Outer radius (in cm)
```

Some sample dimensions:

  deltaSeGA: inner 4.9149, outer 5.08, Al

  classicSeGA: inner 7.366, outer 7.62, Al

  LH2SeGA: inner 7.41, outer 7.62, Fe (steel really)

    </extendeddescription>

    <value>4.9149 5.08</value>

</variable>

<variable>

    <description>Beam pipe material</description>

    <geantname>PIPMAT</geantname>

    <extendeddescription>

        Material of the beam pipe. Options:

            0: No beam pipe

            3: Aluminum

            5: Iron

    </extendeddescription>

    <value>3</value>

</variable>

<variable>

    <description>Distance adjustment (in cm).</description>

    <geantname>DISTANCE</geantname>

    <extendeddescription>

The key is valid only for certain setups (see SETOPT for

details). The distance is always measured in centimeters

from the edge of the ge crystal (whether it is from the

front or side).

```
</extendeddescription>

    <value>0.0</value>

</variable>


<variable>

    <description>Rotation around detector symmetry

    axis (in degrees).</description>

    <geantname>ROTATE</geantname>

    <extendeddescription>
The key is valid only for certain setups (see SETOPT

for details)

    </extendeddescription>

    <value>0.0</value>

</variable>


<variable>

    <description>Position of target on beam

    axis (in cm).</description>

    <geantname>TARPOS</geantname>

    <extendeddescription>
TARPOS = 0.0 is the center of the array.  Gamma-rays will

be emitted based on this target position.

    </extendeddescription>

    <value>-0.554936</value>

</variable>


<variable>

    <description>Target material type.</description>
```

```
    <geantname>TTYPE</geantname>

    <extendeddescription>

The medium id number for the target.  Sample id's are:

 0 -- no target

 1 -- liquid hydrogen

16 -- gold

17 -- lithium

18 -- berylium

19 -- carbon

20 -- bismuth

21 -- polypropelene

22 -- nickel

Notes:

  (a) The no target option also removes any beam lines

  (b) The Liquid Hydrogen option adds the appropriate

      beam line mechanics for the target.

    </extendeddescription>

    <value>18</value>

</variable>


<variable>

    <description>Target thickness (in mg/cm^2).</description>

    <geantname>TTHICK</geantname>

    <extendeddescription>

Thickness of the experimental target.

    </extendeddescription>

    <value>376.</value>

</variable>
```

```
<variable>

    <description>Intrinsic germanium energy-resolution

    parameters (4 values)</description>

    <geantname>GERES</geantname>

    <extendeddescription>

The intrinsic resolution is definded as:

 (1-R/100)*exp(-0.5*((x-x0)/siga)**2) +

 (R/100)*exp((x-x0)/sigma)*erfc((x-x0)/(sqrt(2)*sigma) +

 1/sqrt(2))

where

 sigma = GERES(1)*x0 + GERES(2)

 R = GERES(3)*x0 + GERES(4)

    </extendeddescription>

    <value>0.000205  1.31  0.0162  5.19</value>

</variable>


<variable>

    <description>Intrinsic germanium-segment energy-resolution

    parameters (2 values)</description>

    <geantname>SEGRES</geantname>

    <extendeddescription>

The intrinsic resolution is definded as:

FWHM = v1*energy + v2,

where energy is the detected energy in keV.

    </extendeddescription>

    <value>0.0007123  2.5</value>

</variable>
```

```
<variable>

    <description>Intrinsic silicon energy-resolution parameters

    (2 values)</description>

    <geantname>SIRES</geantname>

    <extendeddescription>

The intrinsic resolution is definded as:

FWHM = v1*energy + v2,

where energy is the detected energy in keV.

    </extendeddescription>

    <value>0.0013534  0.3973</value>

</variable>


<variable>

    <description>Intrinsic plastic energy-resolution parameters

    (2 values)</description>

    <geantname>PLARES</geantname>

    <extendeddescription>

The intrinsic resolution is definded as:

FWHM = v1*energy + v2,

where energy is the detected energy in keV.

    </extendeddescription>

    <value>0.3111111 11.1111</value>

</variable>


<variable>

    <description>Intrinsic NaI energy-resolution parameters

    (2 values)</description>
```

```
    <geantname>NAIRES</geantname>

    <extendeddescription>
The intrinsic resolution is definded as:
FWHM = v1*energy + v2,
where energy is the detected energy in keV.
    </extendeddescription>

    <value>0.3111111 11.1111</value>
</variable>


<variable>
    <description>Segment smear standard deviation</description>
    <geantname>SEGUNC</geantname>
    <extendeddescription>
A value of 1 means 68% of the events take the
selected segment.
        A value of 0.5 means 95% of the events take the
selected segment.
    </extendeddescription>
    <value>0.0</value>
</variable>


<variable>
    <description>Options for event creation.</description>
    <geantname>KINOPT</geantname>
    <extendeddescription>
0 -- Emit PARTICLE with ENERGY in four pi.
    (Kinematics disabled).
1 -- Emit PARTICLE with ENERGY from 0 to THETA
```

(isotropic in phi). (Kinematics disabled).

2 -- Emit PARTICLE with ENERGY at THETA and PHI
   (Kinematics disabled).

3 -- Emit gamma ray in 4pi with randomw energy
   between 0 and 10000 (record only photpeak events)
   (Kinematics disabled).

4 -- Emit gamma ray from predefined list of energies in 4pi.
   (record only photpeak events) (Kinematics disabled).

5 -- Emit gamma rays with ENERGY in four pi.
   (Kinematics ENABLED).

6 -- Emit gamma rays in 4pi with random energy
   between 0 and 10000 (Kinematics ENABLED).

7 -- Emit gamma rays with ENERGY in a distribution defined
   by a probability distribution in the file WGFUNC
        (Kinematics ENABLED)
   </extendeddescription>
   <value>5</value>
</variable>

<variable>
   <description>Angle of emission of particle
   (in degrees)</description>
   <geantname>THETA</geantname>
   <extendeddescription>
This key is only valid for certain event creation
options (see KINEOPT).
   </extendeddescription>
   <value>90</value>

```
</variable>


<variable>

    <description>Angle of emission of particle

    (in degrees)</description>

    <geantname>PHI</geantname>

    <extendeddescription>
This key is only valid for certain event creation

options (see KINEOPT).

    </extendeddescription>

    <value>90</value>

</variable>


<variable>

    <description>Options for beta particle emission</description>

    <geantname>BETOPT</geantname>

    <extendeddescription>
This key is only valid for particle types 2 or 3.

0 -- Emit realistic beat spectrum with Qbeta = ENERGY

1 -- Emit monoenergetic beta of ENERGY.

    </extendeddescription>

    <value>0</value>

</variable>


<variable>

    <description>Number of particles emitted in

    coicidence.</description>

    <geantname>NUMPART</geantname>
```

```
    <extendeddescription>

The maximum number of particles is 10.

    </extendeddescription>

    <value>1</value>

</variable>


<variable>

    <description>Particle type array (10 values)</description>

    <geantname>PARTICLE</geantname>

    <extendeddescription>

The array of particle types to be emitted in coincidence.

This array is ignored in some event creation

options (see KINEOPT).

Some particle types:

1 -- gamma ray.

2 -- positron.

3 -- electron.

    </extendeddescription>

    <value>1 0 0 0 0 0 0 0 0 0</value>

</variable>


<variable>

    <description>Emitted energy

    array (10 values) (in keV).</description>

    <geantname>ENERGY</geantname>

    <extendeddescription>

Array of energies of emitted particles.

This array is ignored in some event creation
```

options (see KINEOPT).

    </extendeddescription>

    <value>1965. 0.0 0.0 0.0 0.0 0.0 0.0 0.0 0.0 0.0 </value>

</variable>

<variable>

    <description>File that contains the W(theta)

    function </description>

    <geantname>WGFUNC</geantname>

    <extendeddescription>

The file name with a W(theta) function for

emitting gamma rays

Format of the file should be:

Wfunc1   Theta1(deg)

Wfunc2   Theta2(deg)

.

.

(repeat for a maxmium of 1800 lines)

    </extendeddescription>

    <value>obalign1002to0.dat</value>

</variable>

<variable>

    <description>Initial velocity of the

    beam (in v/c).</description>

    <geantname>VBEAM</geantname>

    <extendeddescription>

This key is only valid when kinematics are enabled

```
in KINEOPT.
    </extendeddescription>
    <value>.39204</value>
</variable>


<variable>
    <description>Velocity of the beam after the
    target (in v/c).</description>
    <geantname>VEND</geantname>
    <extendeddescription>
This key is only valid when kinematics are enabled
in KINEOPT.
    </extendeddescription>
    <value>.36374</value>
</variable>


<variable>
    <description>Velocity spread of the beam incomming
    beam (in v/c).</description>
    <geantname>VUNC</geantname>
    <extendeddescription>
Standard deviation of the incomming beam
velocity (gaussian distribution).
    </extendeddescription>
    <value>.00302</value>
</variable>


<variable>
```

```
    <description>Velocity to use in the Doppler

    reconstruction (in v/c).</description>

    <geantname>VUSE</geantname>

    <extendeddescription>

This key is only valid when kinematics are enabled

in KINEOPT.

    </extendeddescription>

    <value>0.3787</value>

</variable>


<variable>

    <description>Focus option of the beam.</description>

    <geantname>FOCUSOPT</geantname>

    <extendeddescription>

This key is only valid when kinematics are enabled

in KINEOPT.

1 -- Focussed mode

BSPOT(1):  Spot size sigma (circular distribution).

BSPOT(2):  Not used in this mode.

BSPOT(3):  Vertical position of the center of

the beam spot

BSPOT(4):  Horizontal position of the center

of the beam spot

2 -- Dispersion-matched mode

BSPOT(1):  Vertical distribution (isotropic

with sharp cutoff).

BSPOT(2):  Horizontal distribution (sigma of

gaussian).
```

```
BSPOT(3):  Vertical position of the center

of the beam spot

BSPOT(4):  Horizontal position of the center

of the beam spot

    </extendeddescription>

    <value>1</value>

</variable>


<variable>

    <description>Beam spot size on the

    target (4 values) (in cm).</description>

    <geantname>BSPOT</geantname>

    <extendeddescription>

This key is only valid when kinematics are enabled

in KINEOPT. Meaning of values depends on the beam

optics (see FOCUSOPT).

    </extendeddescription>

    <value>0.388 0.0 0.465202 0.381167</value>

</variable>


<variable>

    <description>Maximum scattering angle of the

    beam (in degrees).</description>

    <geantname>SCATMAX</geantname>

    <extendeddescription>

This key is only valid when kinematics are enabled

in KINEOPT.

This key can be positive or negative.
```

If it is positive then the particle scattering is
assumed to be gaussian with its peak at PSCAT and
a width WSCAT.
If it is negative then the particle scattering is
assumed to be lorentzian with the following type of
distribution:

    angle**(PSCAT)*exp((WSCAT - angle)/WSCAT)

    </extendeddescription>

    <value>-5.16</value>

</variable>

<variable>

    <description>The peak of the beam scattering

    angle (in degrees).</description>

    <geantname>PSCAT</geantname>

    <extendeddescription>

This key is only valid when kinematics are enabled
in KINEOPT.
If SCATMAX is positive the following description
applies:
While the beam scattering angle is naturally peaked
at zero, the scattering angle at which gamma-ray
emission is peaked is typically not at zero. This
situation is approximated by a gaussian peaked
at PSCAT with a width of WSCAT.
If SCATMAX is negative the following description
applies:
PSCAT is the exponent in the Lorentz distribution

described in SCATMAX and WSCAT is the exponential
decay of the Lorentzian.

    </extendeddescription>

    <value>1.88975</value>

</variable>

<variable>

    <description>Width of the beam scattering

    distribution (in degrees).</description>

    <geantname>WSCAT</geantname>

    <extendeddescription>

This key is only valid when kinematics are enabled

in KINEOPT.

See PSCAT for more details.

    </extendeddescription>

    <value>0.523103</value>

</variable>

<variable>

    <description>Half life of the emitting energy

    level (in picoseconds).</description>

    <geantname>HALFLIFE</geantname>

    <extendeddescription>

This key is only valid when kinematics are enabled

in KINEOPT. The actual location of gamma-ray emission

depends on the beam velocity and the level half life.

    </extendeddescription>

    <value>0.0</value>

```
</variable>


<variable>

    <description>Save event increment.</description>

    <geantname>OUTPUT</geantname>

    <extendeddescription>

The hbook file will be saved after every OUTPUT events.

In this way, if GEANT crashes for some reason after near

the end of a simulation, you would still have most of

your data.

    </extendeddescription>

    <value>100000</value>

</variable>


<variable>

    <description>Central contact energy

    threshold (in keV) </description>

    <geantname>CCTHRESH</geantname>

    <extendeddescription>

Central contact energy threshold (in keV) below which

the event is not recorded.  This threshold applies

the same to all SeGA detectors.

    </extendeddescription>

    <value>0</value>

</variable>


<variable>

    <description>Gamma-ray angle determination
```

```
    option.</description>

    <geantname>GAMANGOPT</geantname>

    <extendeddescription>

This key is only valid when kinematics are enabled

in KINEOPT.

0 -- Select segment with greatest energy deposited.

1 -- Use the WFM selection procedure.

    </extendeddescription>

    <value>0</value>

</variable>


<variable>

    <description>Uncertainty in the germanium

    positions (in cm).</description>

    <geantname>GEUNC</geantname>

    <extendeddescription>                        .

GangUnc is assumed to be the radial standard deviation

of the germanium positions. This deviation is applied

to each detector at the beginning of the simulation.

    </extendeddescription>

    <value>0.3</value>

</variable>


<variable>

    <description>Beam tracking option.</description>

    <geantname>TRKOPT</geantname>

    <extendeddescription>

This key is only valid when kinematics are enabled
```

in KINEOPT.

0 -- Take the center of the target for angle
reconstruction.

1 -- Take the actual target position with an
uncertainty of TRACKUNC.

    </extendeddescription>

    <value>0</value>

</variable>

<variable>

    <description>Uncertainty in the beam

    position (in cm).</description>

    <geantname>TRKUNC</geantname>

    <extendeddescription>

This key is only valid when kinematics are enabled
in KINEOPT.

This is the one sigma uncertainty.

    </extendeddescription>

    <value>0.0</value>

</variable>

<variable>

    <description>The target position and beam centroid assumed

    in the reconstruction (3 values) (in cm).</description>

    <geantname>UTARPOS</geantname>

    <extendeddescription>

This key is only valid when kinematics are enabled
in KINEOPT.

UTARPOS(1): Position along the beam line (z)

UTARPOS(2): Vertical position (x)

UTARPOS(3): Horizontal position (y)

    </extendeddescription>

    <value>-0.554936 0.465202 0.381167</value>

</variable>

<variable>

    <description>Maximum energy in the gamma-ray

histograms (in keV).</description>

    <geantname>ENMAX</geantname>

    <extendeddescription>

    </extendeddescription>

    <value>8000.0</value>

</variable>

<variable>

    <description>Number of channels for the energy

histograms.</description>

    <geantname>ENCHAN</geantname>

    <extendeddescription>

Note: For KINEOPT 4 the number of channels is forced

to int(ENMAX).

    </extendeddescription>

    <value>8000</value>

</variable>

<variable>

```
    <description>GEANT defined parameter (do not

    change).</description>

    <geantname>RUNG</geantname>

    <extendeddescription>
You should only change this value if you fully

understand GEANT.

    </extendeddescription>

    <value>1       1</value>

</variable>


<variable>

    <description>GEANT defined parameter (do not

    change).</description>

    <geantname>CUTS</geantname>

    <extendeddescription>
You should only change this value if you fully

understand GEANT.

    </extendeddescription>

    <value>0.000010 0.000010 0.000010 0.000010 0.000010 0.000010

        0.000010 1.e4 1.e4 0.000010 1.e10 0. 0. 0. 0. 0.

</value>

</variable>


<variable>

    <description>GEANT defined parameter (do not

    change).</description>

    <geantname>MUNU</geantname>

    <extendeddescription>
```

You should only change this value if you fully

understand GEANT.

    </extendeddescription>

    <value>0</value>

</variable>

<variable>

    <description>GEANT defined parameter (do not

    change).</description>

    <geantname>HADR</geantname>

    <extendeddescription>

You should only change this value if you fully

understand GEANT.

    </extendeddescription>

    <value>0</value>

</variable>

<variable>

    <description>GEANT defined parameter (do not

    change).</description>

    <geantname>DRAY</geantname>

    <extendeddescription>

You should only change this value if you fully

understand GEANT.

    </extendeddescription>

    <value>0</value>

</variable>

```
<variable>

    <description>GEANT defined parameter (do not

    change).</description>

    <geantname>DEBU</geantname>

    <extendeddescription>

You should only change this value if you fully

understand GEANT.

    </extendeddescription>

    <value>0       0      0</value>

</variable>


<variable>

    <description>GEANT defined parameter (do not

    change).</description> <geantname>TIME</geantname>

    <extendeddescription>

You should only change this value if you fully

understand GEANT.

    </extendeddescription>

    <value>1e10  1  1e10</value>

</variable>


<variable>

    <description>GEANT defined parameter (do not

    change).</description> <geantname>ERAN</geantname>

    <extendeddescription>

You should only change this value if you fully

understand GEANT.

    </extendeddescription>
```

```
        <value>1.e-6     0.01     90</value>

    </variable>

</segasim>
```

Bibliography

[1] M. G. Mayer. *Phys. Rev.*, **75**:1969, 1949.

[2] O. Haxel et al. *Phys. Rev.*, **75**:1766, 1949.

[3] S. G. Nilsson and I. Ragnarsson, editors. *Shapes and Shells in Nuclear Structure.* Cambridge University Press, Cambridge, 1995.

[4] B.V. Pritychenko et al. *Phys. Lett. B*, **461**:322, 1999.

[5] W. D. Hamilton, editor. *The Electromagnetic Interaction in Nuclear Spectroscopy.* North-Holland Publishing Company, Amsterdam, 1975.

[6] G. W. Butler et al. *Phys. Rev. Lett.*, **38**:1380, 1977.

[7] C. Detraz et al. *Phys. Rev. C*, **19**:164, 1979.

[8] C. Detraz et al. *Nucl. Phys. A*, **394**:378, 1983.

[9] D. J. Vieira et al. *Phys. Rev. Lett.*, **57**:3253, 1986.

[10] T. Motobayashi et al. *Phys. Lett. B*, **346**:9, 1995.

[11] B. H. Wildenthal and W. Chung. *Phys. Rev. C*, **22**:2260, 1980.

[12] A. Watt et al. *J. Phys. G*, **7**:L145, 1981.

[13] M. H. Storm et al. *J. Phys. G*, **9**:L165, 1983.

[14] A. Poves and J. Retamosa. *Phys. Lett. B*, **184**:311, 1987.

[15] E.K. Warburton, J.A. Becker, and B.A. Brown. *Phys. Rev. C*, **41**:1147, 1990.

[16] K. Heyde and J. L. Wood. *J. Phys. G*, **17**:135, 1991.

[17] N. Fukunishi et al. *Phys. Lett. B*, **296**:279, 1992.

[18] A. Poves and J. Retamosa. *Nucl. Phys. A*, **571**:221, 1994.

[19] E. Caurier et al. *Phys. Rev. C*, **58**:2033, 1998.

[20] Y. Utsuno et al. *Phys. Rev. C*, **60**:0504315, 1999.

[21] D. J. Dean et al. *Phys. Rev. C*, **59**:2474, 1999.

[22] T. Otsuka et al. *Phys. Rev. Lett.*, **87**:082502, 2001.

[23] X. Campi et al. *Nucl. Phys. A*, **251**:193, 1975.

[24] S. K. Patra and C. R. Praharaj. *Phys. Lett. B*, **273**:13, 1991.

[25] Z. Ren et al. *Phys. Lett. B*, **380**:241, 1996.

[26] F. Grümmer et al. *Phys. Lett. B*, **387**:673, 1996.

[27] J. Terasaki et al. *Nucl. Phys. A*, **621**:706, 1997.

[28] G. A. Lalazissis et al. *Nucl. Phys. A*, **628**:221, 1998.

[29] P.-G. Reinhard et al. *Phys. Rev. C*, **60**:014316, 1999.

[30] P. D. Stevenson et al. *Phys. Lett. B*, **545**:291, 2002.

[31] M. Yamagami and N. V. Giai. *Phys. Rev. C*, **69**:034301, 2004.

[32] C. Thibault et al. *Phys. Rev. C*, **12**:644, 1975.

[33] B. A. Brown. *Prog. Part. Nucl. Phys.*, **47**:517, 2001.

[34] S. Nummela et al. *Phys. Rev. C*, **64**:0504313, 2001.

[35] O. Niedermaier et al. *Phys. Rev. Lett.*, **94**:172501, 2005.

[36] M. Baranger. *Phys. Rev.*, **122**:992, 1961.

[37] K. Yoneda et al. *Phys. Lett. B*, **499**:233, 2001.

[38] M. Belleguic et al. *Physica Scripta*, **T88**:122, 2000.

[39] D. Guillemaud-Mueller. *Eur. Phys. J. A*, **13**:63, 2002.

[40] M. Belleguic et al. *Nucl. Phys. A*, **682**:136c, 2001.

[41] F. Azaiez et al. *Eur. Phys. J. A*, **15**:93, 2002.

[42] F. Azaiez. *Physica Scripta*, **T88**:118, 2000.

[43] F. Azaiez. *Nucl. Phys. A*, **704**:37c, 2002.

[44] D. Bazin et al. *Phys. Rev. Lett.*, **91**:012501, 2003.

[45] W. Mittig et al. *Prog. Theor. Phys. Supp.*, **146**:16, 2002.

[46] D. Guillemaud-Mueller et al. *Nucl. Phys. A*, **426**:37, 1984.

[47] G. Klotz et al. *Phys. Rev. C*, **47**:2502, 1993.

[48] M. Ishihara. *Nucl. Phys. A*, **583**:747, 1995.

[49] H. Olliver, T. Glasmacher, and A. E. Stuchbery. *Phys. Rev. C*, **68**:044312, 2003.

[50] H. Olliver, T. Glasmacher, and A. E. Stuchbery. *Phys. Rev. C*, **69**:024301, 2004.

[51] K. S. Krane. Nuclear orientation formalism. In N. J. Stone and H. Postma, editors, *Low-Temperature Nuclear Orientation*, chapter 2. Elsevier Science Publishers, B.V., 1986.

[52] K. Alder and A. Winther. *Electromagnetic Excitation Theory of Coulomb Excitation with Heavy Ions*. North-Holland Publishing Company, Amsterdam, 1975.

[53] A. E. Stuchbery and M. P. Robinson. *Nucl. Instr. and Meth. A*, **485**:753, 2002.

[54] A. E. Stuchbery. *Nucl. Phys. A*, **723**:69, 2003.

[55] T. J. M. Symons, Y. P. Viyogi, G. D. Westfall, P. Doll, D. E. Greiner, H. Faraggi, P. J. Lindstrom, D. K. Scott, H. J. Crawford, and C. McParland. *Phys. Rev. Lett.*, **42**:40, 1979.

[56] R. Anne et al. *Z. Phys. A*, **352**:397, 1995.

[57] A. Navin et al. *Phys. Rev. Lett.*, **81**:5089, 1998.

[58] T. Yamazaki. *Nucl. Data A*, **3**:1, 1967.

[59] R. M. Diamond, E. Matthias, J. O. Newton, and F. S. Stephens. *Phys. Rev. Lett.*, **16**:1205, 1966.

[60] E. Der Mateosian and A. W. Sunyar. *At. Data and Nucl. Data Tables*, **13**:391, 1974.

[61] D. Sohler et al. *Phys. Rev. C*, **66**:054302, 2002.

[62] G. Neyens et al. *Phys. Lett. B*, **393**:36, 1997.

[63] W.-D. Schmidt-Ott et al. *Z. Phys. A*, **350**:215, 1994.

[64] K. Asahi et al. *Phys. Rev. C*, **43**:456, 1991.

[65] G. A. Souliotis, D. J. Morrissey, N. A. Orr, B. M. Sherrill, and J. A. Winger. *Phys. Rev. C*, **46**:1383, 1992.

[66] Url: http://www.orau.org/ria/ March 31, 2003.

[67] P. G. Hansen. *Phys. Rev. Lett.*, **77**:1016, 1996.

[68] P.G. Hansen and J.A. Tostevin. *Annu. Rev. Nucl. Part. Sci.*, **53**:219, 2003.

[69] P. G. Hansen. priv. comm.

[70] H. Simon et al. *Phys. Rev. Lett.*, **83**:496, 1999.

[71] A. Winther and K. Alder. *Nucl. Phys. A*, **319**:518, 1979.

[72] D. J. Morrissey, B. M. Sherrill, M. Steiner, A. Stolz, and I. Wiedenhoever. *Nucl. Instr. and Meth. B*, **204**:90, 2003.

[73] W. F. Mueller, J. A. Church, T. Glasmacher, D. Gutknecht, G. Hackman, P. G. Hansen, Z. Hu, K. L. Miller, and P. Quirin. *Nucl. Instr. and Meth. A*, **466**:492, 2001.

[74] GEANT. CERN library long writeup. Technical Report W5013, CERN, 1994.

[75] Url: http://www.bentley.com/en-US/Products/MicroStation/ August 5, 2005.

[76] Stephen Wolfram. *The Mathematica Book*. Wolfram Media/Cambridge University Press, third edition, 1996.

[77] K. L. Miller et al. *Nucl. Instr. and Meth. A*, **490**:140, 2002.

[78] A. Gade. priv. comm.

[79] PAW, 2002. http://paw.web.cern.ch/paw.

[80] J. A. Caggiano. *Spectroscopy of Exotic Nuclei with the S800 Spectrograph*. PhD thesis, Michigan State University, 1998.

[81] J. Yurkon et al. *Nucl. Instr. and Meth. A*, **422**:291, 1999.

[82] D. Bazin et al. *Nucl. Instr. and Meth. B*, **204**:629, 2003.

[83] Url: http://groups.nscl.msu.edu/s800/ July 05, 2005.

[84] G. F. Knoll. *Radiation Detection and Measurement*. John Wiley and Sons, Inc., third edition, 2000.

[85] T. Glasmacher. *Annu. Rev. Nucl. Part. Sci.*, **48**:1, 1998.

[86] J. A. Tostevin. *Phys. Rev. C*, **70**:064602, 2004.

[87] B. Singh. *Eval. Nucl. Structure Data File*, 2004.

[88] D. Bazin. priv. comm.

[89] B. A. Brown. priv. comm.

[90] B. A. Brown. *Phys. Rev. C*, **58**:220, 1998.

[91] J. A. Tostevin. priv. comm.

[92] J. A. Tostevin et al. *Nucl. Phys. A*, **746**:166c, 2004.

[93] J.M. Kidd et al. *Phys. Rev. C*, **37**:2613, 1988.

[94] J. Fridmann et al. *Nat.*, **435**:922, 2005.

[95] R. W. Ibbotson et al. *Phys. Rev. Lett.*, **80**:2081, 1998.

[96] J. A. Tostevin. Two-nucleon knockout reactions and spectroscopy. In *Direct Reactions with Exotic Beams,DREB 2005*. National Superconducting Cyclotron Laboratory, Michigan State University, 2005.

[97] B.A. Brown et al. *Phys. Rev. C*, **65**:061601(R), 2002.

[98] V.R. Pandharipande, I. Sick, and P.K.A. deWitt Huberts. *Rev. Mod. Phys.*, **69**:981, 1997.

[99] W. H. Dickhoff and C. Barbieri. *Prog. Part. Nucl. Phys.*, **52**:377, 2004.

[100] H. Mach et al. *Eur. Phys. J. A*, **25**:105, 2005.

[101] H. Scheit. priv. comm. Sept. 13, 2005.

[102] S. S. M. Wong. *Introductory Nuclear Physics*. John Wiley and Sons, Inc., 1998.

[103] B. Singh et al. *Nucl. Data Sheets*, **84**:487, 1998.

[104] S. Nummela et al. *Phys. Rev. C*, **63**:044316, 2001.

[105] J. P. Dufour et al. *Z. Phys. A*, **324**:487, 1986.